

# THE GASEOUS ENVIRONMENT OF HIGH-Z GALAXIES: PRECISION MEASUREMENTS OF NEUTRAL HYDROGEN IN THE CIRCUMGALACTIC MEDIUM OF $Z \sim 2-3$ GALAXIES IN THE KECK BARYONIC STRUCTURE SURVEY<sup>1</sup>

GWEN C. RUDIE,<sup>2</sup> CHARLES C. STEIDEL,<sup>2</sup> RYAN F. TRAINOR,<sup>2</sup> OLIVERA RAKIC,<sup>3,4</sup> MILAN BOGOSAVLJEVIĆ,<sup>5</sup> MAX PETTINI,<sup>6,7</sup>  
NAVEEN REDDY,<sup>8,9,10</sup> ALICE E. SHAPLEY<sup>11</sup>, DAWN K. ERB,<sup>12</sup> AND DAVID R. LAW<sup>13</sup>

*Draft version September 18, 2018*

## ABSTRACT

We present results from the Keck Baryonic Structure Survey (KBSS), a unique spectroscopic survey of the distant universe designed to explore the details of the connection between galaxies and intergalactic baryons within the same survey volumes, focusing particularly on scales from  $\sim 50$  kpc to a few Mpc. The KBSS is optimized for the redshift range  $z \sim 2-3$ , combining  $S/N \sim 100$  Keck/HIRES spectra of 15 of the brightest QSOs in the sky at  $z \simeq 2.5-2.9$  with very densely sampled galaxy redshift surveys within a few arcmin of each QSO sightline. In this paper, we present quantitative results on the distribution, column density, kinematics, and absorber line widths of neutral hydrogen (H I) surrounding a subset of 886 KBSS star-forming galaxies with  $2.0 \lesssim z \lesssim 2.8$  and with projected distances  $\leq 3$  physical Mpc from a QSO sightline. Using Voigt profile decompositions of the full Ly $\alpha$  forest region of all 15 QSO spectra, we compiled a catalog of  $\sim 6000$  individual absorbers in the redshift range of interest, with  $12 \leq \log(N_{\text{HI}}) \leq 21$ . These are used to measure H I absorption statistics near the redshifts of foreground galaxies as a function of projected galactocentric distance from the QSO sightline and for randomly chosen locations in the intergalactic medium (IGM) within the survey volume. We find that  $N_{\text{HI}}$  and the multiplicity of velocity-associated H I components increase rapidly with decreasing galactocentric impact parameter and as the systemic redshift of the galaxy is approached. The strongest H I absorbers within  $\simeq 100$  physical kpc of galaxies have  $N_{\text{HI}} \sim 3$  orders of magnitude higher than those near random locations in the IGM. The circumgalactic zone of most significantly enhanced H I absorption is found within transverse distances of  $\lesssim 300$  kpc and within  $\pm 300$  km s<sup>-1</sup> of galaxy systemic redshifts. Taking this region as the defining bounds of the circumgalactic medium (CGM), nearly half of absorbers with  $\log(N_{\text{HI}}) > 15.5$  are found within the CGM of galaxies meeting our photometric selection criteria, while their CGM occupy only 1.5% of the cosmic volume. The spatial covering fraction, multiplicity of absorption components, and characteristic  $N_{\text{HI}}$  remain significantly elevated to transverse distances of  $\sim 2$  physical Mpc from galaxies in our sample. Absorbers with  $N_{\text{HI}} > 10^{14.5}$  cm<sup>-2</sup> are tightly correlated with the positions of galaxies, while absorbers with lower  $N_{\text{HI}}$  are correlated with galaxy positions only on  $\gtrsim$  Mpc scales. Redshift anisotropies on these larger scales indicate coherent infall toward galaxy locations, while on scales of  $\sim 100$  physical kpc peculiar velocities of  $\Delta v \simeq \pm 260$  km s<sup>-1</sup> with respect to the galaxies are indicated. The median Doppler widths of individual absorbers within 1-3  $r_{\text{vir}}$  of galaxies are larger by  $\simeq 50\%$  than randomly chosen absorbers of the same  $N_{\text{HI}}$ , suggesting higher gas temperatures and/or increased turbulence likely caused by some combination of accretion shocks and galactic winds around galaxies with  $M_{\text{halo}} \simeq 10^{12} M_{\odot}$  at  $z \sim 2-3$ .

*Subject headings:* cosmology: observations — galaxies: high-redshift — galaxies: evolution — galaxies: formation — intergalactic medium — quasars: absorption lines

## 1. INTRODUCTION

Hydrogen, comprising three quarters of the baryonic mass of the universe, is the principal component of all luminous objects in the universe. It is the fuel source for stars and therefore for star formation. Thus, in order to understand the formation and evolution of galaxies, one must understand and be able to trace the inflow and outflow of this fuel.

There exist very poor observational constraints on the movement of baryons in and out of galaxies. At high redshift in star-forming systems, it has been argued that the outflow rate must be similar to the star-formation rate (Pettini et al. 2000) and that the inflow rate must be similar to the combined star-formation rate and outflow rate (Erb 2008; Finlator & Davé 2008).

Recently there has been a flurry in the theoretical lit-

Electronic address: gwen@astro.caltech.edu

<sup>1</sup> Based on data obtained at the W.M. Keck Observatory, which is operated as a scientific partnership among the California Institute of Technology, the University of California, and the National Aeronautics and Space Administration, and was made possible by the generous financial support of the W.M. Keck Foundation.

<sup>2</sup> Cahill Center for Astronomy and Astrophysics, California Institute of Technology, MS 249-17, Pasadena, CA 91125, USA

<sup>3</sup> Leiden Observatory, Leiden University, P.O. Box 9513, 2300 RA Leiden, The Netherlands

<sup>4</sup> Max-Planck-Institut für Astronomie, Königstuhl 17, 69117 Heidelberg, Germany

<sup>5</sup> Astronomical Observatory, Volgina 7, 11060 Belgrade, Serbia

<sup>6</sup> Institute of Astronomy, Madingley Road, Cambridge CB3 0HA, UK

<sup>7</sup> International Centre for Radio Astronomy Research, University of Western Australia, 7 Fairway, Crawley WA 6009, Australia

<sup>8</sup> National Optical Astronomy Observatory, 950 N Cherry Ave, Tucson, AZ 85719

<sup>9</sup> Department of Physics and Astronomy, UC Riverside, 900 University Avenue, Riverside, CA 92521

<sup>10</sup> Hubble Fellow

<sup>11</sup> Department of Astronomy, University of California, Los Angeles, 430 Portola Plaza, Los Angeles, CA 90024, USA

<sup>12</sup> Department of Physics, University of Wisconsin Milwaukee, Milwaukee, WI, 53211

<sup>13</sup> Dunlap Institute for Astronomy & Astrophysics, University of Toronto, 50 St. George Street, Toronto M5S 3H4, Ontario, Canada

erature predicting the prevalence of accretion of cold gas ( $\log(T) \lesssim 4.5 - 5.5$  K) onto high- $z$  galaxies via filamentary “cold flows” (Birnboim & Dekel 2003; Kereš et al. 2005; Ocvirk et al. 2008; Brooks et al. 2009; Faucher-Giguère et al. 2011; van de Voort et al. 2011a,b). In this model, the baryons stream into galaxies along the filamentary structure of the cosmic web, accreting onto galaxies without experiencing virial shocks. A wide range of predictions has been made concerning the efficiency of the transport of this material into galaxy halos, as well as its role in fueling ongoing star formation (van de Voort et al. 2011b; Faucher-Giguère et al. 2011). Further, there may be substantial suppression of the cold accretion rate caused by galaxy-scale mass outflows, evidence for which is commonly observed in the spectra of high- $z$  star-forming systems (Pettini et al. 2001; Shapley et al. 2003; Adelberger et al. 2005a; Steidel et al. 2010). Mapping the gas distribution surrounding galaxies is critical to constraining these models (Faucher-Giguère & Kereš 2011; Fumagalli et al. 2011), and would be a significant step toward understanding and quantifying the exchange of baryons between the sites of galaxy formation and the nearby intergalactic medium (IGM).

There has been a large amount of recent theoretical examination of the nature of IGM absorbers and their relation to galaxies using simulations.  $\text{Ly}\alpha$  is believed to broadly trace the filamentary large-scale structure (Cen et al. 1994; Zhang et al. 1995; Miralda-Escudé et al. 1996; Hernquist et al. 1996; Rauch et al. 1997; Theuns et al. 1998; Davé et al. 1999; Schaye 2001) although there are indications (Barnes et al. 2011) that winds could blow spatially extended halos of gas which may have recently been observed both in absorption (Steidel et al. 2010) and in  $\text{Ly}\alpha$  emission (Steidel et al. 2011). There seems to be general agreement that galactic winds are responsible for metal absorbers in the IGM. Booth et al. (2010) suggest that mostly low mass ( $M_{\text{DM}} \lesssim 10^{10} M_{\odot}$ ) galaxies must be responsible for the pollution, while Wiersma et al. (2010) suggest only half of the metals would originate from galaxies with  $M_{\text{DM}} \lesssim 10^{11} M_{\odot}$ . Wiersma et al. (2010) also studied the history of the ejection of these metals and found that half of the metals observed at redshift 2 were ejected during the time between  $2 < z < 3$ . Using cosmological “zoom-in” simulations Shen et al. (2011) found a “Lyman Break”-type galaxy could distribute metals to 3 virial radii by  $z = 3$ . Simcoe (2011) recently considered this problem observationally, finding that indeed 50% of the metals observed in the IGM at  $z \sim 2.4$  were placed there since  $z \sim 4.3$ , i.e. in 1.3 Gyr. Oppenheimer & Davé (2008) and Oppenheimer et al. (2010) studied the fate of winds using cosmological simulations and found that while galactic winds are likely responsible for the metallic species seen in the IGM, much of the outflowing gas may be bound to galaxies and may fall back in. In their simulations the recycling timescale scaled inversely with mass because winds emanating from more massive galaxies experienced greater hydrodynamic drag due to the increased abundance of dense IGM surrounding them. Further, in these simulations the largest source of gaseous fuel for star formation after  $z \sim 1$  was recycled wind material.

To date, systematic attempts to jointly study high- $z$  galaxies and their intergalactic environs have been made by Adelberger et al. (2003, 2005a) (see also Crighton et al. 2011). These studies focused primarily on H I and C IV absorption in the spectra of background QSOs whose sightlines

probed regions covered by  $2 < z < 4$  Lyman break galaxy (LBG) surveys. This work allowed for a first glimpse of the distribution of diffuse gas surrounding forming galaxies at high redshift, and, perhaps more tantalizing, evidence for interactions between the IGM and galaxies during the epoch when galaxies are expected to be most active. Generally, Adelberger et al. (2003) and Adelberger et al. (2005a) found excess H I absorption out to  $\approx 5 - 6h^{-1}$  comoving Mpc (cMpc) of galaxies [ $\sim 2$  physical Mpc (pMpc) at  $\langle z \rangle = 3.3$  using the cosmology adopted in this paper]. C IV systems were found to correlate strongly with the positions of galaxies suggesting a causal connection. Unfortunately, these papers could not consider physical properties of the gas such as its column density or temperature because the data were not of sufficiently high quality to perform Voigt profile analysis. As such these papers focused on the transmitted flux which could be applied to a wider range of data qualities.

In this work, we provide high-accuracy analysis of the spectral regions surrounding 886 high- $z$  star-forming galaxies as seen in absorption against the spectra of background hyperluminous QSOs using data drawn from the Keck Baryonic Structure Survey (KBSS; Steidel et al, in prep). The KBSS was specifically designed to allow for the observation of gas absorption features surrounding high-redshift star-forming galaxies, providing unique insight into the IGM/galaxy interface at high redshift. The size and quality of the KBSS sample allow us to map the distribution and properties of gas near to individual star-forming galaxies with direct physical parameters such as the column density as opposed to proxies such as the equivalent width. This paper is the first in a series designed to study the physical properties of star-forming galaxies at high redshift using Voigt profile analysis of this data sample. The complementary analysis presented by Rakic et al. (2011b) describes the pixel statistics of the QSO spectra from the KBSS and the correlation of H I optical depth with the positions and redshifts of galaxies.

In §2 we discuss the galaxy and QSO data and present the Voigt profile analysis of the QSO spectra in §3. The distributions of H I absorbers as a function of velocity, impact parameter, and 3D distance are presented in §4. In §5 we consider the geometric distribution of the gas using the covering fraction and incidence of absorbers. §6 focuses on 2D “maps” of the absorber distribution around galaxies. In §7 we analyze the velocity widths of individual absorbers and their correlation with the proximity of galaxies. We discuss the results and their possible interpretation in §8 with a brief summary of the paper and our conclusions in §9.

Throughout this paper we assume a  $\Lambda$ -CDM cosmology with  $H_0 = 70 \text{ km s}^{-1} \text{ Mpc}^{-1}$ ,  $\Omega_m = 0.3$ , and  $\Omega_{\Lambda} = 0.7$ . All distances are expressed in physical (proper) units unless stated otherwise. We use the abbreviation pkpc and pMpc to indicate physical units, and ckpc or cMpc for co-moving units. At the mean redshift of the galaxy sample ( $\langle z \rangle = 2.3$ ), 300 pkpc is  $210h^{-1}\text{pkpc}$  (physical) or  $\simeq 700h^{-1}\text{ckpc}$ ; the age of the universe is 2.9 Gyr, the look-back time is 10.9 Gyr, and 8.2 pkpc subtends one arcsecond on the sky.

## 2. OBSERVATIONS

The data presented in this paper are drawn from the Keck Baryonic Structure Survey (KBSS) and include a large sample of rest-UV (2188) and rest-optical (112) spectra of UV-color selected star-forming galaxies at  $\langle z \rangle \sim 2.3$ . These galaxies were photometrically selected to lie in the foreground of one of 15 hyper-luminous QSOs in the redshift range  $2.5 \leq z_{\text{QSO}} \leq$

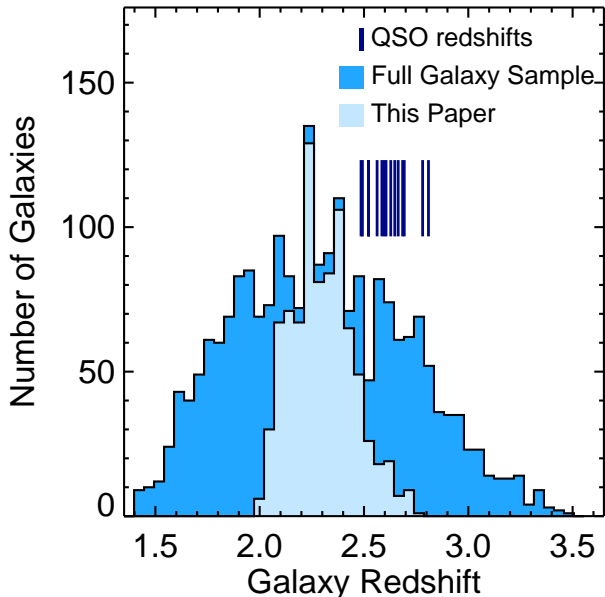


**Figure 1.** The redshift distribution of the 2188 galaxies in the full KBSS sample (dark shaded histogram) and of the subset of 886 galaxies used for the analysis in this paper (light shaded histogram), which are those with redshifts high enough that the corresponding wavelength of the Ly $\beta$  transition is observed in the relevant QSO spectrum, and with  $z < z_{\text{QSO}} - 3000 \text{ km s}^{-1}$ . The dark vertical line segments mark the redshifts of the 15 KBSS QSOs.

2.85 for which we have obtained high-resolution, high signal-to-noise ratio (S/N) echelle spectra.

The redshift range of this survey has important significance in the history of the universe – it coincides with the peak of both universal star formation (see Reddy et al. 2008) and super-massive black hole growth (see Richards et al. 2006). Spectroscopic observations of star-forming galaxies during this epoch commonly exhibit signatures of strong outflowing winds (Pettini et al. 2001; Shapley et al. 2003; Adelberger et al. 2005a; Steidel et al. 2010). At the same time, the baryonic accretion rate onto galaxies is predicted to be near its peak at  $z \sim 2.5$  (e.g., van de Voort et al. 2011b; Faucher-Giguère et al. 2011; van de Voort et al. 2011a). Thus, the signatures of galaxy formation within the IGM should be at their peak as well.

The redshift range  $2.0 \lesssim z \lesssim 2.8$  offers a number of practical advantages as well: first, the rapidly-evolving Ly $\alpha$  forest has thinned enough to allow measurements of individual H I systems and to enable the detection of important metallic transitions falling in the same range (notably, O VI  $\lambda\lambda 1031, 1036$ ); second, the astrophysics-rich rest-frame far-UV becomes accessible to large ground-based telescopes equipped with state-of-the-art optical spectrographs; third, the rest-frame optical spectrum is shifted into the atmospheric transmission windows in the near infrared, allowing for observations of a suite of diagnostic emission lines (H $\alpha$ , H $\beta$ , [O II]  $\lambda\lambda 3726, 3729$ , [O III]  $\lambda\lambda 4363, 4959, 5007$ , and [S II]  $\lambda\lambda 6717, 6732$ ) neatly packed into the J, H, and K bands.

### 2.1. The Galaxy Sample

The KBSS galaxy sample, a subset of which is used in this paper (Figure 1), is described in detail by Steidel et al (2012); here we present a brief summary. Galaxies were selected for spectroscopy using their rest-frame UV colors (i.e., LBGs) according to the criteria outlined by Steidel et al. (2004) and Adelberger et al. (2004) for  $z \sim 2$  and by Steidel et al. (2003)

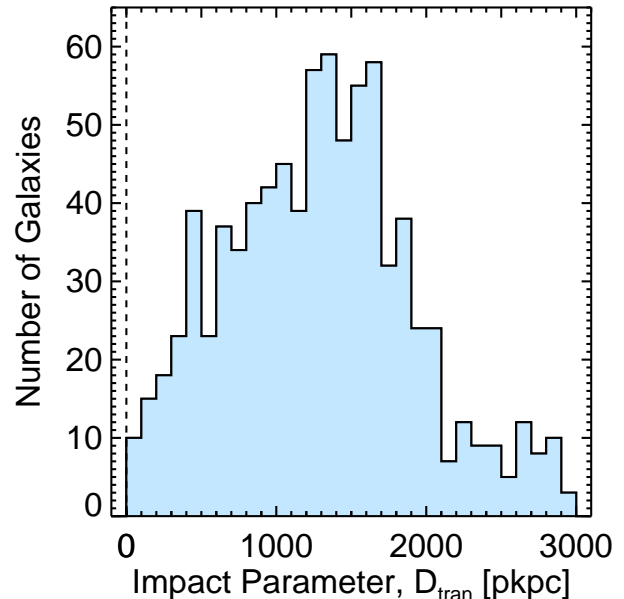


**Figure 2.** The number of galaxies as a function of physical impact parameter  $D_{\text{tran}}$  for the sample which has appropriate redshifts to be used in this work (light shaded histogram in Figure 1; see Table 1). The decline in the number of galaxies at  $D_{\text{tran}} \approx 2 \text{ pMpc}$  is due to the typical survey geometry of the KBSS fields as described in §4.2.1.

for  $z \sim 3$ . In combination, these criteria have been devised to efficiently select star-forming galaxies over the redshift range  $1.5 \lesssim z \lesssim 3.5$ . In total, the KBSS galaxy sample includes  $R \simeq 1000$  ( $\sim 5\text{-}10\text{\AA}$ ) rest-UV spectra of 2188 star-forming galaxies obtained at the W.M. Keck Observatory using the Keck 1 10m telescope and the blue arm of the Low Resolution Imaging Spectrometer (LRIS-B; Oke et al. 1995; Steidel et al. 2004.)

Most of the observations were conducted using a 400 lines  $\text{mm}^{-1}$  grism (blazed at 3400  $\text{\AA}$  in first order) in combination with a dichroic beamsplitter sending all light shortward of  $\sim 6800 \text{\AA}$  into the blue channel, where the wavelength coverage for a typical slit location was  $\simeq 3100\text{--}6000 \text{\AA}$  with a resolving power  $R \simeq 800$  using  $1''/2$  wide slits (Steidel et al. 2010). Some of the spectra were obtained using the d560 beamsplitter (beam divided near 5600  $\text{\AA}$ ) together with a 600 lines  $\text{mm}^{-1}$  grism (4000  $\text{\AA}$  blaze), typically covering  $\simeq 3400\text{--}5600 \text{\AA}$  with a resolving power  $R \simeq 1300$ . Observations obtained after July 2007 made use of the Cassegrain Atmospheric Dispersion Corrector, thus minimizing the effects of differential atmospheric refraction over the spectral range of interest. Wavelength calibration was accomplished using Hg, Cd, Zn, and Ne lamps, with zero point corrections based on night sky emission lines on each individual exposure.<sup>14</sup>

The exposure times allocated to individual galaxies ranged from 1.5-7.5 hours depending on the number of separate masks containing the same target; typically galaxies were observed on either 1 or 2 masks, each mask receiving a total integration of 1.5 hours. Further details on the selection, observing strategy, and data reduction for KBSS galaxies are presented elsewhere (Steidel et al. 2010, Steidel et al. 2012).

The rest-UV spectra of LBGs are dominated by the continuum emission of O and B stars, over which are super-

<sup>14</sup> An extensive discussion of the LRIS/KBSS wavelength calibration errors (including slit illumination and atmospheric dispersion) is given in Steidel et al. (2010).

**Table 1**  
KBSS Central QSOs and Foreground Galaxy Samples

Name	RA	Dec	$z_{\text{QSO}}^{\text{a}}$	$\lambda_{\text{min}}^{\text{b}}$	$z_{\text{gal}} \text{ range}$	$N_{\text{gal}}^{\text{c}}$	S/N Ly $\alpha^{\text{d}}$	S/N Ly $\beta^{\text{d}}$
Q0100+130 (PHL957)	01:03:11.27	+13:16:18.2	2.721	3133	2.0617–2.6838	47	77	50
HS0105+1619	01:08:06.4	+16:35:50.0	2.652	3230	2.1561–2.6153	53	127	89
Q0142–09 (UM673a)	01:45:16.6	–09:45:17.0	2.743	3097	2.0260–2.7060	65	71	45
Q0207–003 (UM402)	02:09:50.71	–00:05:06.5	2.872	3227	2.1532–2.8339	46	82	55
Q0449–1645	04:52:14.3	–16:40:16.2	2.684	3151	2.0792–2.6470	50	73	41
Q0821+3107	08:21:07.62	+31:07:51.17	2.616	3239	2.1650–2.5794	37	50	33
Q1009+29 (CSO 38)	10:11:55.60	+29:41:41.7	2.652 <sup>e</sup>	3186	2.1132–2.6031	36	99	58
SBS1217+499	12:19:30.85	+49:40:51.2	2.704	3098	2.0273–2.6669	43	68	38
HS1442+2931	14:44:53.67	+29:19:05.6	2.660	3152	2.0798–2.6237	46	99	47
HS1549+1919	15:51:52.5	+19:11:04.3	2.843	3165	2.0926–2.8048	54	173	74
HS1603+3820	16:04:55.38	+38:12:01.8	2.551 <sup>f</sup>	3181	2.1087–2.5066	37	108	58
Q1623+268 (KP77)	16:25:48.83	+26:46:58.8	2.5353	3126	2.0544–2.4999	133 <sup>g</sup>	48	28
HS1700+64	17:01:00.6	+64:12:09.4	2.751	3138	2.0668–2.7138	110 <sup>g</sup>	98	42
Q2206–199	22:08:52.1	–19:43:59.7	2.573	3084	2.0133–2.5373	45	88	46
Q2343+125	23:46:28.30	+12:48:57.8	2.5730	3160	2.0884–2.5373	84 <sup>g</sup>	71	45

<sup>a</sup> The redshift of the QSO

<sup>b</sup> The minimum wavelength covered in the HIRES QSO spectrum

<sup>c</sup> The number of galaxies in our LRIS survey with  $D_{\text{tran}} < 3$  pMpc and spectroscopic redshifts in the correct range given in the previous column.

<sup>d</sup> The average signal to noise ratio per pixel of the QSO spectrum in the wavelength range pertaining to CGM Ly $\alpha$  and Ly $\beta$  absorption.

<sup>e</sup> The redshift of this QSO was revised after the fitting of the HIRES spectrum was completed. The redshift assumed for the  $\Delta v = -3000$  km s<sup>-1</sup> is 2.6395

<sup>f</sup> The redshift of this QSO was revised after the fitting of the HIRES spectrum was completed. The redshift assumed for the  $\Delta v = -3000$  km s<sup>-1</sup> is 2.5420

<sup>g</sup> The photometry and spectroscopy in fields Q1623, HS1700, and Q2343 cover larger areas than a single LRIS footprint. As such, they represent the fields in which we sample the galaxy-IGM connection at  $D_{\text{tran}} > 2$  pMpc.

posed numerous resonance absorption lines of metallic ions and H I. The H I Ly $\alpha$  line at 1215.67 Å may be seen in emission or absorption (and often in both). The absorption features arise in cool interstellar gas in the foreground of the OB stars; they are most commonly observed to be blue-shifted by 100 – 800 km s<sup>-1</sup> with respect to the systemic velocity of the stars, as measured from either rest-frame optical nebular emission lines or stellar photospheric lines in stacked spectra (see Pettini et al. 2001; Shapley et al. 2003; Adelberger et al. 2005a; Steidel et al. 2010) or from the redshift-space symmetry of Ly $\alpha$  absorption in the nearby IGM (Rakic et al. 2011a). Common lines observed include: O VI  $\lambda\lambda$ 1031,1036, Si II  $\lambda$ 1260,  $\lambda$ 1526, Si II+O I  $\lambda$ 1303 (blend), Si III  $\lambda$ 1206, Si IV  $\lambda\lambda$ 1393,1402, N V  $\lambda\lambda$ 1238,1242, C II  $\lambda$ 1334, C III  $\lambda$ 977, and C IV  $\lambda\lambda$ 1548,1550. The profile of the Ly $\alpha$  emission or absorption line is modulated by the optical depth of the material closest to the systemic velocity of the stars, which has been shown to correlate most significantly with the baryonic mass (Steidel et al. 2010) and the physical size (Law et al., in prep) of the galaxy.

The sample used in this study includes 886 galaxies within the redshift range where at minimum Ly $\alpha$  and Ly $\beta$  are observed in the HIRES spectrum and with redshifts placing them at least 3000 km s<sup>-1</sup> blue-ward of the redshift of the QSO. The latter criterion was selected to avoid proximate systems that originate within material ejected from the QSO itself and/or the region affected by its ionizing radiation field.

A typical galaxy in the spectroscopic survey has a bolometric luminosity of  $\sim 2.5 \times 10^{11} L_{\odot}$  (Reddy et al. 2008, 2011), a star-formation rate (SFR) of  $\sim 30 M_{\odot} \text{ yr}^{-1}$  (Erb et al. 2006b), a stellar age of  $\sim 0.7$  Gyr (Erb et al. 2006c), and a gas-phase metallicity of  $\simeq 0.5 Z_{\odot}$  (Erb et al. 2006a). The galaxies inhabit dark matter halos of average mass  $\sim 10^{12} M_{\odot}$  (Adelberger et al. 2005b; Conroy et al. 2008, Trainor & Steidel, in prep; Rakic et al, in prep) and average dynamical

masses of  $\sim 7 \times 10^{10} M_{\odot}$  (Erb et al. 2006c) and generally exhibit dispersion-dominated kinematics (Law et al. 2009). The luminous parts of the galaxies are dominated by baryons, typically half stars and half cold gas (Shapley et al. 2005; Erb et al. 2006c), with half-light radii of  $\sim 2$  pkpc (Law et al. 2011). The spectroscopic sample includes objects with apparent magnitudes  $\mathcal{R} \leq 25.5$ , where  $\mathcal{R}$  is equivalent to  $m_{\text{AB}}(6830 \text{ \AA})$ . At the mean redshift of the sample ( $\langle z \rangle = 2.30$ ) the faint limit corresponds to a galaxy of  $0.25 L_{\text{UV}}^*$  (Reddy & Steidel 2009).

The redshift distribution of the galaxy and QSO sample is presented in Figure 1, and the distribution of physical impact parameters,  $D_{\text{tran}}$ , between the galaxies and the QSO lines of sight is shown in Figure 2.

At present, 112 galaxies in the full KBSS sample have been observed spectroscopically in the near-IR using using NIR-SPEC (McLean et al. 1998) on the Keck II telescope. 87 of these galaxies lie in our chosen redshift interval. The NIR-SPEC target selection, data, and reductions are discussed in Erb et al. (2006b,c). The NIR redshifts, generally based on the H $\alpha$  emission line, are estimated to be accurate to  $\sim 60$  km s<sup>-1</sup> or  $\sigma_z \simeq 0.0007$  at  $z \sim 2.3$ .

## 2.2. Measured and Calibrated Redshifts

Because the most prominent features in the UV spectra of star forming galaxies are not at rest with respect to a galaxy's systemic redshift,  $z_{\text{gal}}$ , corrections must be applied to avoid substantial systematic redshift errors. The velocity peak and centroid of the Ly $\alpha$  emission line, when present, tend to be redshifted with respect to  $z_{\text{gal}}$  by several hundred km s<sup>-1</sup>, while the strong UV absorption features ( $z_{\text{IS}}$ ) tend to be similarly blue-shifted with respect to  $z_{\text{gal}}$  (Shapley et al. 2003; Adelberger et al. 2003; Steidel et al. 2010). These observations are generally interpreted as strong evidence for the presence of galaxy-scale outflows.

Here we adopt estimates of galaxy systemic redshifts ( $z_{\text{gal}}$ ) computed in the manner proposed by Adelberger et al. (2005a) and later updated by Steidel et al. (2010) and Rakic et al. (2011a). Adelberger et al. (2005a) and Steidel et al. (2010) analyzed the subset of the UV sample for which both rest-UV and rest-optical spectra had been obtained. They measured the average offset between redshifts defined by  $\text{H}\alpha$  emission versus  $z_{\text{Ly}\alpha}$  and  $z_{\text{IS}}$  to estimate average corrections. The  $\text{H}\alpha$  line traces the ionized gas in star-forming regions and is therefore a reasonable proxy for the systemic velocity of the stars, which are more difficult to measure due to the weakness of the UV photospheric absorption lines. Rakic et al. (2011a) used the QSO and galaxy data set presented here and calibrated velocity offsets appropriate for various classes of LBGs by insisting that the average IGM  $\text{Ly}\alpha$  absorption profiles should be symmetric with respect to galaxy redshifts. In both cases, the offsets represent those of the ensemble while in reality there is some scatter between individual objects even if their spectral morphology is similar. However, as we will demonstrate, the adopted  $z_{\text{gal}}$  must be generally quite accurate in order to produce the trends described below.

The formulae used for estimating  $z_{\text{gal}}$  from  $z_{\text{Ly}\alpha}$  and  $z_{\text{IS}}$  measurements are reproduced below. For galaxies with  $\text{H}\alpha$ -based redshifts (87/886), we set  $z_{\text{gal}} = z_{\text{H}\alpha}$ . For galaxies which have measured  $z_{\text{IS}}$  with or without the presence of  $\text{Ly}\alpha$  emission (691/886),

$$z_{\text{gal,IS}} \equiv z_{\text{IS}} + \frac{\Delta v_{\text{IS}}}{c}(1 + z_{\text{IS}}), \quad (1)$$

where

$$\Delta v_{\text{IS}} = 160 \text{ km s}^{-1} \quad (2)$$

is the velocity shift needed to transform the observed redshift into its systemic value,  $z_{\text{IS}}$  is the measured redshift from the centroids of interstellar absorption lines, and  $z_{\text{gal,IS}}$  corresponds to the estimated systemic redshift of the galaxy.

For galaxies which have redshifts measured *only* from  $\text{Ly}\alpha$  in emission (90/886), we compute the redshift as

$$z_{\text{gal,Ly}\alpha} \equiv z_{\text{Ly}\alpha} + \frac{\Delta v_{\text{Ly}\alpha}}{c}(1 + z_{\text{Ly}\alpha}), \quad (3)$$

where

$$\Delta v_{\text{Ly}\alpha} = -300 \text{ km s}^{-1} \quad (4)$$

is the velocity shift needed to transform the observed redshift into its systemic value,  $z_{\text{Ly}\alpha}$  is the measured redshift from  $\text{Ly}\alpha$ , and  $z_{\text{gal,Ly}\alpha}$  is adopted systemic redshift.

For galaxies with measurements of both  $z_{\text{IS}}$  and  $z_{\text{Ly}\alpha}$ , we verify that  $z_{\text{IS}} < z_{\text{gal,IS}} < z_{\text{Ly}\alpha}$ . If the corrected absorption redshift is not bracketed by the two measured redshifts (18/886 galaxies)<sup>15</sup>, then we use the average of  $z_{\text{IS}}$  and  $z_{\text{Ly}\alpha}$ :

$$z_{\text{gal}} \equiv \frac{z_{\text{Ly}\alpha} + z_{\text{IS}}}{2}. \quad (5)$$

The residual redshift errors have a significant impact on our ability to interpret the kinematic information in the data; thus, their amplitude will be important to consider in the examination of the line-of-sight distribution of H I. Steidel et al.

<sup>15</sup> In these cases,  $z_{\text{IS}}$  and  $z_{\text{Ly}\alpha}$  have very similar values and therefore taking their average generally provides a systemic redshift with less potential error than in those galaxies for which an average shift (as in equations 1 and 3) is required.

(2010) found this method generally corrects the redshifts to within  $\sim 125 \text{ km s}^{-1}$  of the systemic velocity.

### 2.3. QSO Observations

The 15 hyper-luminous ( $m_V \simeq 15.5 - 17$ ) QSOs in the center of the KBSS fields (Table 1) were observed with the High Resolution Echelle Spectrometer (HIRES; Vogt et al. 1994) on the Keck I telescope. All available archival data for these 15 QSOs have been incorporated, including data taken with UVES (Dekker et al. 2000) on the VLT for Q2206-199 and Q2343+125. We obtained additional HIRES observations in order to reach a uniformly high S/N ratio over the spectral range of primary interest, 3100–6000 Å. The final HIRES spectra have  $R \simeq 45,000$  ( $\text{FWHM} \simeq 7 \text{ km s}^{-1}$ ),  $\text{S/N} \sim 50 - 200$  per pixel, covering at least the wavelength range 3100 – 6000 Å with no spectral gaps. The significant improvement in the UV/blue sensitivity of HIRES resulting from a detector upgrade in 2004 enabled us to observe  $\text{Ly}\beta \lambda 1025.7$  down to at least  $z = 2.2$  in all 15 KBSS sightlines, and to significantly lower redshifts in many (see Table 1.) The additional constraints provided by  $\text{Ly}\beta$  (and in many cases, additional Lyman series transitions) allow for much more accurate measurements of H I for  $N_{\text{HI}} = 10^{14} - 10^{17} \text{ cm}^{-2}$  (see §3); this is particularly important since these column densities are typical of H I gas in the CGM at these redshifts (see §5).

The QSO spectra were reduced using T. Barlow’s MAKEE package which is specifically tailored to the reduction of HIRES data. The output from MAKEE is a wavelength-calibrated<sup>16</sup> extracted spectrum of each echelle order, corrected for the echelle blaze function and transformed to vacuum, heliocentric wavelengths. The spectra were continuum-normalized in each spectral order using low-order spline interpolation, after which the normalized 2-D spectrograms were optimally combined into a single one-dimensional, continuum-normalized spectrum resampled at  $2.8 \text{ km s}^{-1}$  per pixel.

Three of the KBSS QSO spectra contain a damped Lyman  $\alpha$  (DLA) system ( $N_{\text{HI}} > 10^{20.3} \text{ cm}^{-2}$ ), and three contain a sub-DLA ( $10^{19} \lesssim N_{\text{HI}} < 10^{20.3} \text{ cm}^{-2}$ ). Special care must be taken in the continuum fit to the regions surrounding these systems, as the damping wings of the absorption lines extend for thousands of  $\text{km s}^{-1}$  from line center. In these regions, we carefully fit a Voigt profile to the core of the absorber and adjusted the original continuum fit so that the Voigt profile produced a good fit to the damping wings, as shown in the top panel of Figure 3. The final Voigt profile fit is divided into the true spectrum, resulting in a new spectrum where the wings of the DLA have been removed, as illustrated in the bottom panel of Figure 3. The re-normalized spectrum can then be used to fit additional absorption systems superposed on the damping wings.

The redshifts of the QSOs are measured from rest-frame optical emission lines using lower-dispersion NIR spectra. The details of this procedure and the expected errors in the QSO redshifts are reported upon in Trainor & Steidel (2011, submitted). The precise QSO redshifts do not affect our analysis.

## 3. ANALYSIS OF QSO ABSORPTION SPECTRA

<sup>16</sup> The wavelength calibration of the HIRES spectra introduce negligible error into our analysis. The HIRES spectra have calibration errors less than  $0.5 \text{ km s}^{-1}$ .

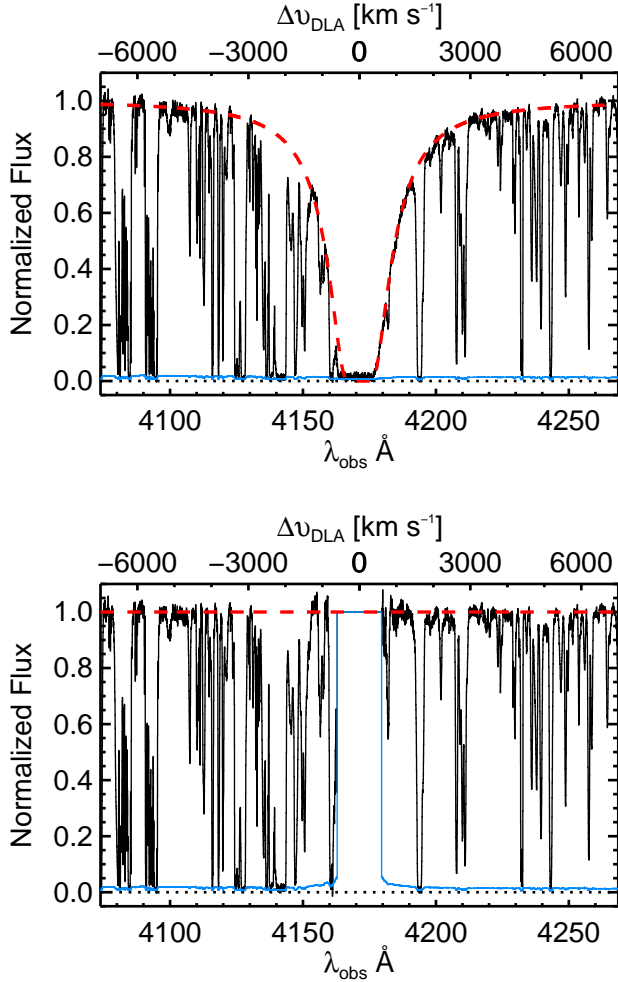


**Figure 3.** A demonstration of our treatment of the continuum surrounding damped- $\text{Ly}\alpha$  systems. *Top:* In black, the continuum-normalized H IRES spectrum of Q2343+125 showing  $\pm 7000 \text{ km s}^{-1}$  surrounding the DLA. The (red) dashed line corresponds to the Voigt profile of the DLA centered at  $z = 2.4312$  with  $\log(N_{\text{HI}}) = 20.4$ . Shown in the light (blue) curve is the error spectrum. *Bottom:* The H IRES spectrum of the same QSO with the DLA profile divided out. The new error spectrum accounting for the DLA profile division is shown by the light (blue) curve. The new continuum (with the DLA divided out) is shown in the dashed (red) curve.

The process of accurately measuring H I in the  $\text{Ly}\alpha$  forest of QSO spectra is complicated by the saturation of moderately strong absorbers and the blending of H I features with other H I or with lines of metallic species that happen to fall in the forest region.

Our analysis includes a full Voigt-profile decomposition of the  $\text{Ly}\alpha$  forest from the lowest redshift for which  $\text{Ly}\beta$  is available in each spectrum up to  $3000 \text{ km s}^{-1}$  blue-ward of the QSO redshift; Table 1 shows the relevant redshift range used for each QSO in the sample. The cut-off at the high redshift end is to avoid H I systems which could be ejected from and/or ionized by the QSO itself; the low-redshift cut is necessary due to the high frequency of systems with  $N_{\text{HI}} \gtrsim 10^{14.5} \text{ cm}^{-2}$  that will be saturated in  $\text{Ly}\alpha$ <sup>17</sup>. For saturated systems, the fit to  $\text{Ly}\alpha$  is degenerate between an increase in column den-

<sup>17</sup> Note that the exact saturation point for the  $\text{Ly}\alpha$  line and for any other line depends on the line width (i.e. the Doppler parameter) and thus the internal properties of the absorbing cloud.

sity or an increase in the width of the line,  $b_d$ . The best way to resolve this degeneracy is to measure higher-order Lyman lines where decreasing oscillator strengths allow accurate  $N_{\text{HI}}$  determination.

Simultaneous fits were made to as many Lyman lines as were both (1) available in the observed spectral range and (2) needed to measure an unsaturated and uncontaminated profile in the highest-order line. The exact number of higher-order Lyman lines used therefore depended upon both the redshift of the absorber and the degree of contamination in the spectral region containing the higher-order Lyman series absorption features. Higher-order lines, whether saturated or unsaturated, were used whenever doing so provided additional constraints on the overall fit.

Example Voigt profile fits to the H I absorption in regions surrounding the systemic redshift of five galaxies from our sample are shown in Figure 4. Note that for galaxies with redshifts significantly larger than  $z \sim 2.2$ , many higher-order Lyman transitions can be measured.

To facilitate the fitting of the Lyman  $\alpha$  forest, we developed a semi-automatic line-fitting code. Briefly described, the code works with  $\sim 1500 \text{ km s}^{-1}$  sections of spectrum at a time<sup>18</sup>, fitting to  $\text{Ly}\alpha$  and as many higher-order lines as are accessible within the H IRES spectrum at the redshift of the H I systems being fit. The algorithm first searches for systems by cross correlating a template hydrogen absorption spectrum (i.e., a single non-saturated H I absorption component) with the H IRES spectrum. Peaks in the cross correlation are taken as initial estimates of the centroids of absorption lines. We fit Gaussians to these lines to estimate column densities and Doppler parameters. Residual absorption features (i.e., those inconsistent with  $\text{Ly}\alpha$ ) in the  $\text{Ly}\alpha$  portion of the spectrum are assumed to be metal lines. Residual absorption in the higher-order Lyman series sections of the spectra are assumed to be lower-redshift H I systems. The fits begin with  $\text{Ly}\alpha$  at the high-redshift end of the range so that their higher-order Lyman absorption can be flagged as a known contaminant for fitting lower-redshift H I absorbers.

Once estimates of the locations, column densities, and Doppler parameters of all the absorption lines are complete, they are input into the  $\chi^2$  minimization code VPFIT<sup>19</sup> written by R.F. Carswell and J.K. Webb. VPFIT simultaneously fits all transitions of H I as well as the specified contaminating lines. The results are checked by eye, alterations made where the fit is inappropriate, and the process is repeated iteratively until a good fit (reduced  $\chi^2 \approx 1$ ) is achieved. At this point, the multiple sections of spectrum are spliced together until a full fit to the forest is achieved.

It should be noted that the Voigt profile fit to a spectrum does not represent a unique solution. In this work, we fit each set of absorbers with the minimum number of components, adding additional components only when they significantly improve the  $\chi^2$ . Median errors in  $N_{\text{HI}}$  reported by VPFIT are 0.07 dex for absorbers with  $13 < \log(N_{\text{HI}}) < 14$  and 0.03 dex for absorbers with  $14 < \log(N_{\text{HI}}) < 16$ ; however in many cases the systematic errors will exceed these values. The largest source of error in our fits to low column-density systems is

<sup>18</sup> Note, the choice of  $1500 \text{ km s}^{-1}$  was made largely out of convenience. This velocity window is the largest window which can be easily displayed to check the goodness of fit and for which the number of components allows for a reasonable VPFIT run time.

<sup>19</sup> <http://www.ast.cam.ac.uk/rfc/vpfit.html>; © 2007 R.F. Carswell, J.K. Webb

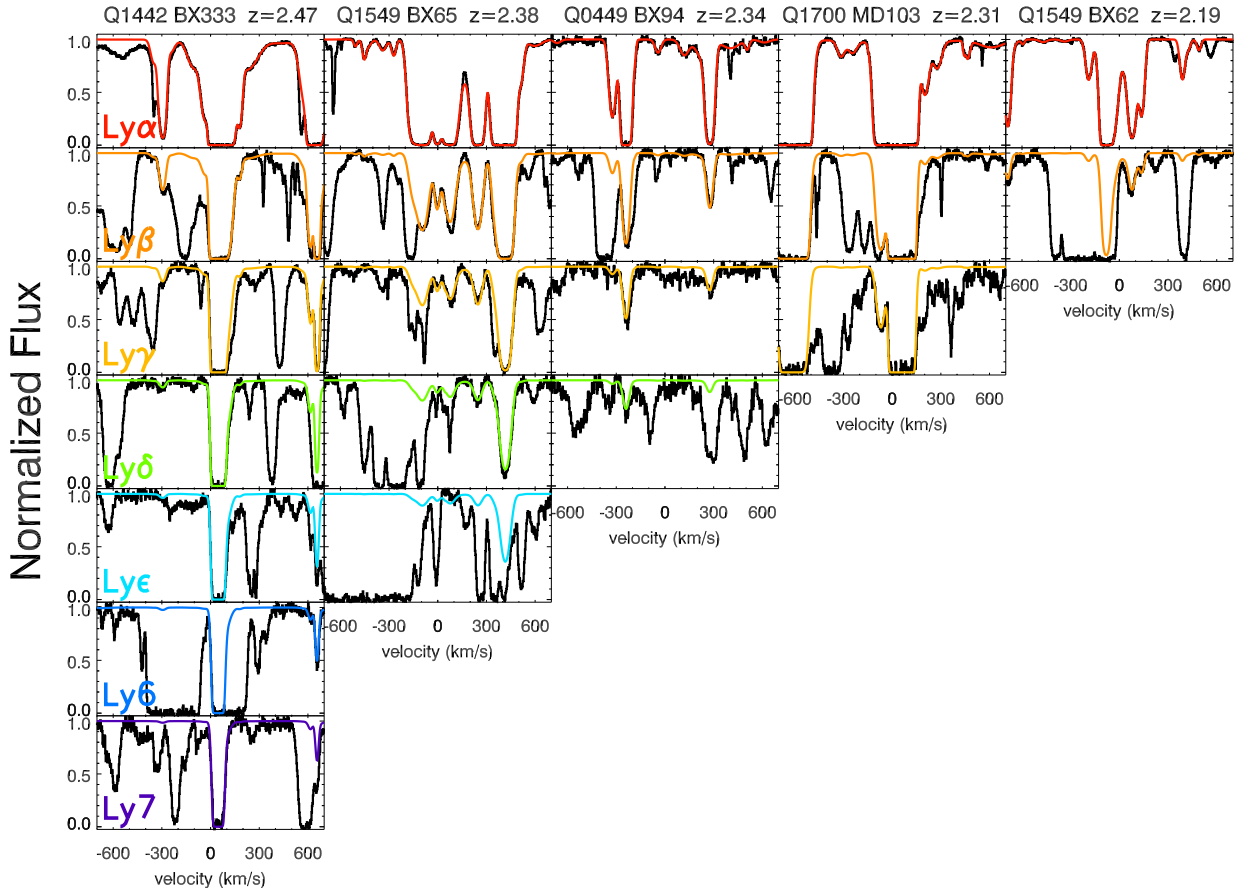


**Figure 4.** Example fits to the QSO data surrounding the redshifts of galaxies in our sample. Displayed in black are the continuum-normalized HRES spectra showing the Lyman series transitions within  $\pm 700 \text{ km s}^{-1}$  of the systemic redshift of 5 galaxies with redshifts as indicated. Over-plotted in color are Voigt profile decompositions for H I absorption systems within  $\pm 700 \text{ km s}^{-1}$  of the galaxy redshift. Successive rows illustrate the fit to Ly $\alpha$ , Ly $\beta$ , etc. Absorption in the HRES spectra that does not appear in the colored fit corresponds to absorption from metallic species or from H I at a redshift far from that of the galaxy. Note that for all galaxies in our sample, the QSO spectra cover the Ly $\alpha$  and Ly $\beta$  transitions near the galaxy redshifts, and for the higher-redshift galaxies, many more transitions in the Lyman series can be measured.

uncertainty in the continuum level; for high column-density absorbers, it is the possibility of unrecognized sub-component structure.

The complete decomposition of the Ly $\alpha$  forest in these 15 lines of sight includes Voigt profile fits to  $> 5900$  distinct H I absorption systems with  $N_{\text{HI}} > 10^{12.0} \text{ cm}^{-2}$ , making it the largest absorber catalog ever compiled at these redshifts. It increases by an order of magnitude the number of intermediate  $N_{\text{HI}}$  absorbers measured with the additional constraint of higher-order Lyman lines.

#### 4. CIRCUMGALACTIC H I

In the following sections, we discuss the statistics of individual H I absorption systems with respect to the redshifts and transverse positions of galaxies. We do not uniquely “assign” each absorber to a specific galaxy or vice versa. Instead we rely on comparisons between the absorption measured close to galaxies with that typical of “random” locations<sup>20</sup> in the IGM. This allows us to quantify the significance of any apparent correlation with galaxies.

In principle, it would be preferable to compare absorbers found close to galaxies with those found in IGM locations

<sup>20</sup> A “random” location, as described later in this section, is in effect a random redshift from our galaxy redshift catalog and an independent random position on the sky from our galaxy position catalog.

known to be far from galaxies; however, because the galaxy sample is spectroscopically incomplete compared to our photometrically selected targets,<sup>21</sup> we do not measure the redshifts of all galaxies in our survey volume. As a consequence, we do not know which locations in 3D space *do not* have a nearby galaxy. Thus, we can only compare locations near to galaxies with random locations in the IGM (irrespective of the positions of galaxies).

In order to reproduce the absorber distributions for a typical place in the IGM, we compiled a catalog of 15,000 random locations (in both redshift space and on the plane of the sky). The redshifts are drawn from the actual galaxy redshift list and therefore reproduce the typical IGM absorption associated with the redshift ranges covered by our galaxy sample. With each redshift, we also associate a randomly drawn QSO and an impact parameter to the QSO sightline from the real galaxy impact parameter list. We can then study the distribution of absorption systems around these 15,000 random locations and thereby understand how the presence of a galaxy alters the distributions.

Below we consider the distribution of H I surrounding galaxies: first along the line of sight, then on the plane of the

<sup>21</sup> Our photometric sample is also incomplete at the faintest apparent magnitudes (see Reddy et al. 2008), and no attempt is made to include galaxies with  $\mathcal{R} > 25.5$ .

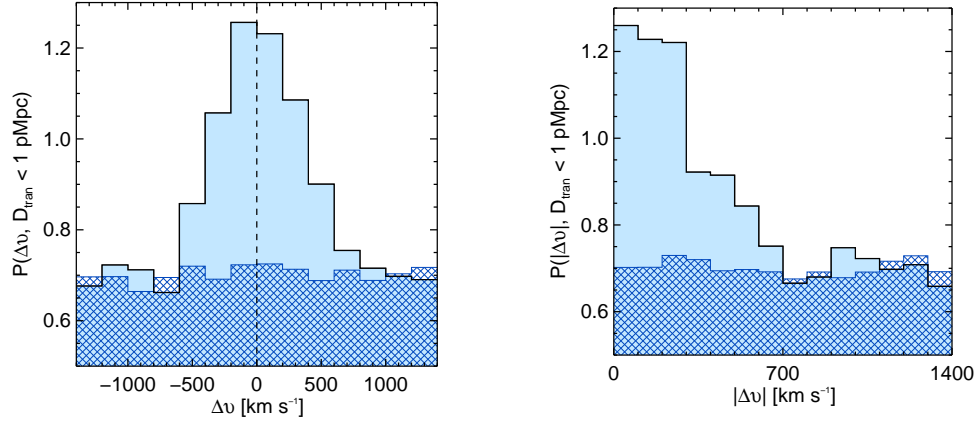


**Figure 5.** The velocity-space distribution of H I absorption systems with respect to the systemic redshift of galaxies, normalized by the number of galaxies in the sample. Absorbers with  $\log(N_{\text{HI}}) > 13$  and within 1 pMpc of the sightline to a QSO are included. The solid histogram represents the distribution of H I around galaxies, whereas the hatched histogram represents the average absorber density near randomly-chosen redshifts drawn from our galaxy redshift distribution.

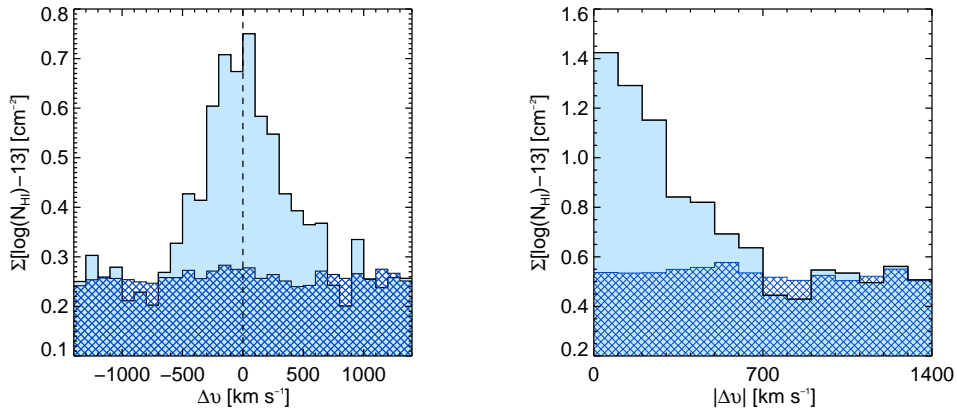


**Figure 6.** As in Figure 5, where the histogram is  $N_{\text{HI}}$ -weighted as described in the text.

sky, and finally as a function of 3D distance. These measurements are used to determine the relevant velocity and transverse scales of circumgalactic H I.

#### 4.1. Velocity-Space Distribution of H I Near Galaxies

The properties of H I gas near galaxies in our sample can be quantified in several ways. First, we consider the line of sight velocity distribution of absorbers relative to the redshifts of galaxies. Shown in Figure 5 is the velocity distribution of all absorbers with  $N_{\text{HI}} > 10^{13} \text{ cm}^{-2}$  within  $1400 \text{ km s}^{-1}$  in redshift and 1 pMpc in projected distance from a galaxy. We define the velocity offset,  $\Delta v$ , of an absorber,

$$\Delta v \equiv \frac{(z_{\text{abs}} - z_{\text{gal}})c}{1 + z_{\text{gal}}} \quad (6)$$

where  $z_{\text{abs}}$  is the absorption system redshift and  $z_{\text{gal}}$  is the adopted systemic redshift of the galaxy from §2.2. With this definition, absorbers blue-shifted with respect to galaxies have negative  $\Delta v$ .

We define  $P(\Delta v, D_{\text{tran}})$  as the number of absorbers per galaxy at a given  $\Delta v$  and within the specified range of impact parameters  $D_{\text{tran}}$ . The solid histogram in Figure 5 represents

the distribution of H I around galaxies, whereas the hatched histogram shows the average number of absorbers expected relative to randomly chosen redshifts, as described above. The number of absorbers is clearly higher near galaxies, with an excess peaking near  $\Delta v = 0$  (the galaxy systemic redshift) and confined to  $\Delta v \simeq \pm 700 \text{ km s}^{-1}$ .

Figure 6 shows a similar pattern; in this case, each absorption system is weighted in proportion to  $\log(N_{\text{HI}})$  such that high-column density systems contribute more significantly to the histogram. Each absorber with  $\log(N_{\text{HI}}) > 13$  contributes  $[\log(N_{\text{HI}}) - 13]$  to the histogram, which is normalized by the number of galaxies considered. Taken together, Figures 5 and 6 indicate that there is an increase near galaxies of both the number and the column density of H I absorbers. The narrow peak of the  $\Delta v$  distribution has an apparent half-width of  $\sim 300 \text{ km s}^{-1}$ , while the full excess extends to  $\simeq \pm 700 \text{ km s}^{-1}$  (most clearly shown in the right-hand panel of Figure 6).

As has been argued by Shapley et al. (2003); Adelberger et al. (2003); Steidel et al. (2010); Rakic et al. (2011a), these velocity distributions are also useful for checking our redshift calibration; their symmetry about  $\Delta v = 0 \text{ km s}^{-1}$  is a sensitive probe of systematic errors in our galaxy systemic redshift calibration, while the width of the



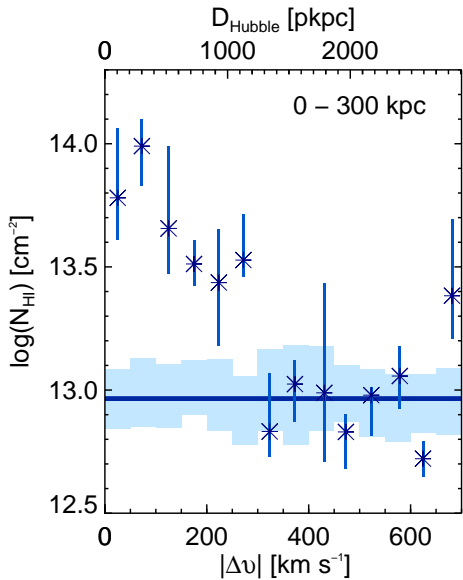


**Figure 7.** The median value of  $N_{\text{HI}}$  as a function of the velocity offset of absorbers with respect to those galaxies with impact parameters  $D_{\text{tran}} < 300$  pkpc. Asterisks represent the median value of  $N_{\text{HI}}$ , dark vertical bars are the  $1-\sigma$  dispersion in the median determined via the bootstrap method. The dark horizontal line is the median value of  $N_{\text{HI}}$  in the random distribution. The light shaded boxes are the bootstrapped symmetric  $1-\sigma$  dispersion in the median values of the samples drawn from the random distribution. The top x-axis shows the conversion between velocity offset and Hubble distance. See Equation 7 and §4.3 for further discussion.

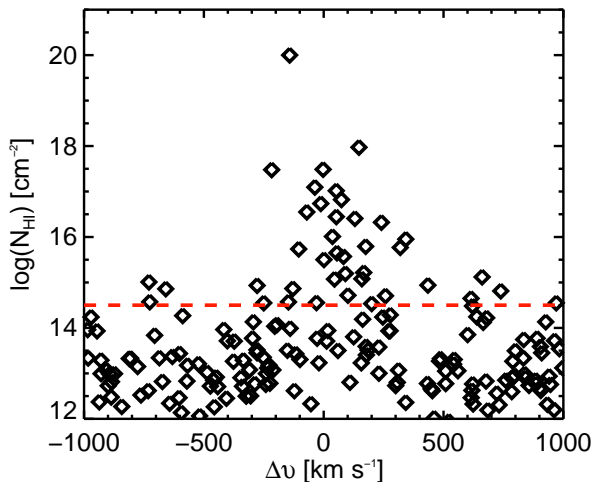


**Figure 8.**  $N_{\text{HI}}$  as a function of  $\Delta v$  for absorbers with  $D_{\text{tran}} < 100$  pkpc. The dashed (red) line marks the position of  $\log(N_{\text{HI}}) = 14.5$ . The significance of this column density threshold is discussed in §5.

distribution provides an upper limit on the random errors.<sup>22</sup> A Gaussian fit to Figure 5 yields a mean  $\Delta v = 18 \pm 26$  with a standard deviation of  $308 \pm 30$  km s<sup>-1</sup>.

An alternative method of quantifying the column density dependence in Figure 6 is to examine the distribution of  $N_{\text{HI}}$  as a function of  $\Delta v$ . Figure 7 shows the median  $N_{\text{HI}}$  as a function of  $\Delta v$  for all absorbers within  $D_{\text{tran}} \leq 300$  pkpc of a galaxy<sup>23</sup>.

<sup>22</sup> The width is an upper limit because it includes both redshift errors and any peculiar velocity of absorbers relative to galaxies.

<sup>23</sup> We choose 300 pkpc as our distance cut because the majority of the

The asterisks indicate the median value of  $N_{\text{HI}}$  for each bin in velocity space. The dark vertical lines represent the dispersion in the median computed through the bootstrap method<sup>24</sup>. The value of the median column density across all velocity bins for the random distribution is shown as the dark horizontal bar; the light shaded contours are the  $1-\sigma$  bootstrapped dispersions in the median of the random sample, where we consider samples of the same size as those from the real distribution. Note that there is an enhancement by a factor of  $\approx 3-10$  in the median  $N_{\text{HI}}$  out to  $|\Delta v| \approx 300$  km s<sup>-1</sup> relative to galaxy redshifts. However, for  $|\Delta v| > 300$  km s<sup>-1</sup>, the measurements are consistent with random places in the IGM.

Shown in Figure 8 are the individual measurement of  $N_{\text{HI}}$  as a function of  $\Delta v$  for all absorbers within 1000 km s<sup>-1</sup> of a galaxy within  $D_{\text{tran}} \leq 100$  pkpc of a QSO sightline. Notably, the higher- $N_{\text{HI}}$  absorbers cluster strongly near the galaxy systemic redshift with a full width of  $\sim \pm 300-400$  km s<sup>-1</sup>.

In summary, Figures 5–8 clearly illustrate an enhancement in both the column density and number of absorption systems near the systemic velocities of galaxies. The most significant enhancement of column density is seen within  $\pm 300$  km s<sup>-1</sup> (Figure 7), but there is a higher number of absorbers out to at least  $\pm 700$  km s<sup>-1</sup> (Figures 5 and 6).

#### 4.2. Transverse Distribution of Absorbers

In addition to the strong velocity alignment of absorption systems with the systemic redshift of nearby galaxies, there is also a significant increase in the column densities,  $N_{\text{HI}}$ , of individual absorbers with decreasing projected (or transverse) distance between the galaxy and the line of sight,  $D_{\text{tran}}$ . Here, we suppose that, as an ensemble, these galaxies show similar circumgalactic absorption signatures. Therefore, because galaxies fall at various discrete impact parameters from the QSO line of sight, we can combine the information from each galaxy to make a sparsely sampled map of the absorption as a function of  $D_{\text{tran}}$  relative to the ensemble galaxy.

We introduce two related statistics designed to trace the change in column density as a function of  $D_{\text{tran}}$ . Recalling that  $\pm 700$  km s<sup>-1</sup> encompassed the bulk of the “excess” absorption (§4.1), for each galaxy we define  $\max(N_{\text{HI}}, 700 \text{ km s}^{-1})$  to be the value of  $\log(N_{\text{HI}})$  for the strongest absorber with  $|\Delta v| < 700$  km s<sup>-1</sup> of the galaxy systemic redshift. The left panel of Figure 9 shows the median value of  $\max(N_{\text{HI}}, 700 \text{ km s}^{-1})$  as a function of impact parameter. A second statistic is the logarithm of the total  $N_{\text{HI}}$ ,  $\text{sum}(N_{\text{HI}})$ , of all absorbers with  $|\Delta v| < 700$  km s<sup>-1</sup>. The statistics of the median value of  $\text{sum}(N_{\text{HI}}, 700 \text{ km s}^{-1})$  versus  $D_{\text{tran}}$  is shown in the right-hand panel of Figure 9. Generally, the values of these two statistics are quite similar because the  $N_{\text{HI}}$  in most velocity windows is dominated by the single highest- $N_{\text{HI}}$  absorber. We consider the sum because it is most easily compared to results of numerical simulations, as it does not require the fitting of Voigt profiles to simulated data and can instead be compared to a simulation “collapsed” along the line of sight.

Figure 9 clearly demonstrates that both  $\max(N_{\text{HI}})$  and  $\text{sum}(N_{\text{HI}})$  increase rapidly as one approaches a galaxy. In the bin corresponding to the smallest impact parameters,  $D_{\text{tran}} <$

excess absorption is found within that zone, as described in §4.2.

<sup>24</sup> To bootstrap the dispersion in the median, we draw (with replacement) sets of data with the same size as the real distribution. For each set the median is computed; 100 such data sets are evaluated, and then we take the  $1-\sigma$  symmetric bounds on the distribution of the medians, i.e. the 16th and 84th percentiles.

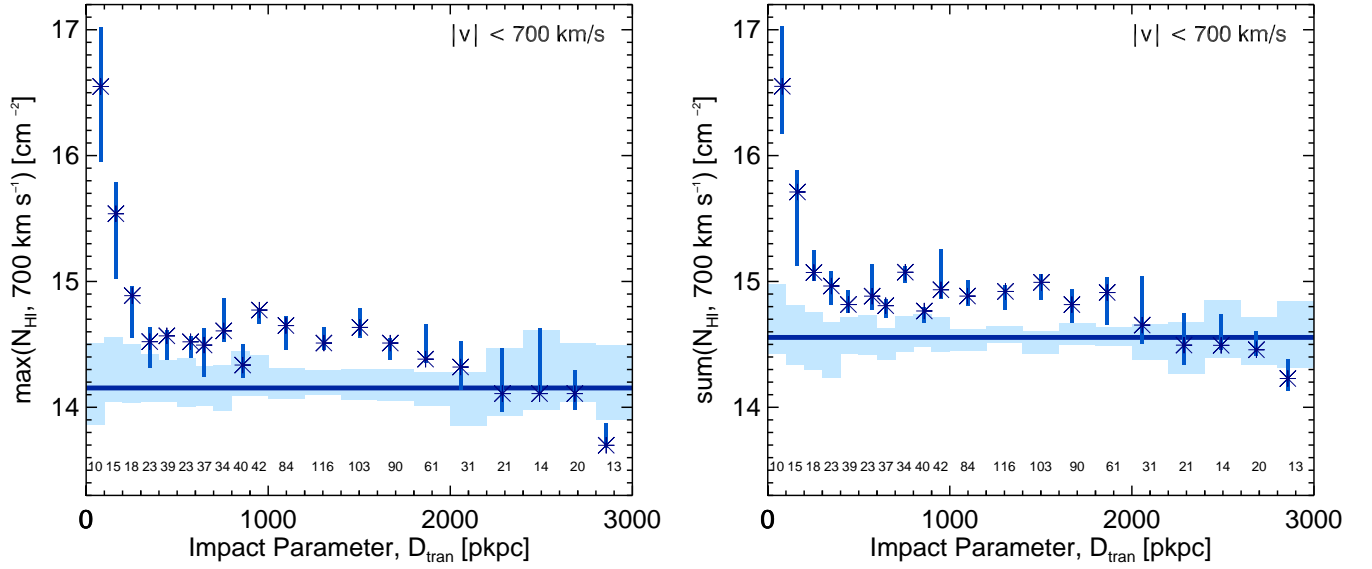


**Figure 9.** The log column densities of the strongest  $N_{\text{HI}}$  absorbers as a function of transverse distance. *On the left* we consider the  $\max(N_{\text{HI}})$  statistic, the log of the maximum column density of the single strongest absorber per galaxy with  $|\Delta v| < 700 \text{ km s}^{-1}$ . *On the right* is the  $\text{sum}(N_{\text{HI}})$  statistic, the log of the sum of the  $N_{\text{HI}}$  of all the absorbers within  $|\Delta v| < 700 \text{ km s}^{-1}$ . Asterisks represent the median value of the considered statistic in a given bin of  $D_{\text{tran}}$ . Dark vertical bars are their dispersions. The horizontal position of the asterisks represent the median  $D_{\text{tran}}$  of the galaxies in that bin. The number of galaxies in each bin is indicated at the bottom of the plot. The dark horizontal line is the median value drawn from the random distribution. The light shaded boxes are the bootstrapped symmetric  $1\text{-}\sigma$  dispersion in the median values of the samples drawn from the random distribution. The bin size is 100 pkpc for absorbers with  $D_{\text{tran}} < 1 \text{ pMpc}$  and 200 pkpc for those with  $D_{\text{tran}} > 1 \text{ pMpc}$ . We increase in binning to reduce the shot noise in the bins at  $D_{\text{tran}} > 2 \text{ pMpc}$  which have fewer galaxies due to the limited field-of-view of LRIS.

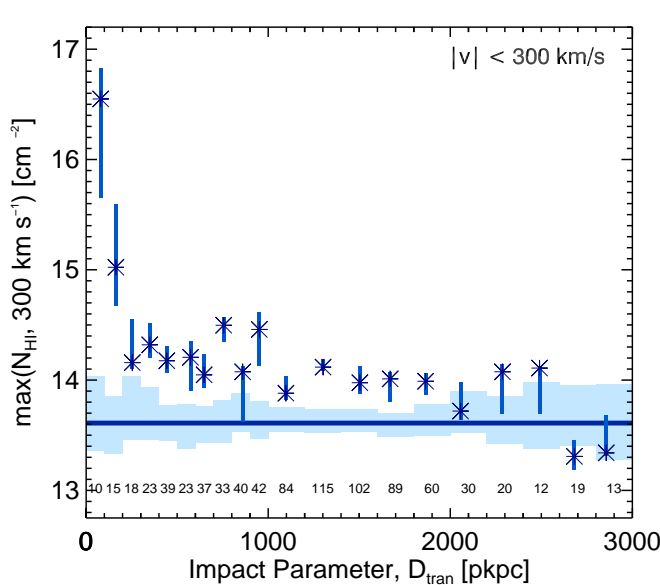


**Figure 10.** Same as Figure 9 but for the maximum column density absorber within  $\pm 300 \text{ km s}^{-1}$ . Changing the velocity interval considered with the  $\max(N_{\text{HI}})$  statistic has little effect on the observed trends.

100 pkpc, the median value of  $\max(N_{\text{HI}})$  is more than two orders of magnitude higher than that of a random location. Moving outwards, the median value decreases with increasing  $D_{\text{tran}}$  to 300 pkpc, at which point the statistic “plateaus” and remains significantly higher than the random sample out to 2 pMpc. The plateau value in the galaxy-centric sample is  $\max(N_{\text{HI}}) \simeq 10^{14.5} \text{ cm}^{-2}$ , while that of the random distribution is  $\max(N_{\text{HI}}) \simeq 10^{14.1} \text{ cm}^{-2}$ . As we will discuss in §4.2.1,  $\max(N_{\text{HI}})$  begins to decline for  $D_{\text{tran}} > 2 \text{ pMpc}$ .

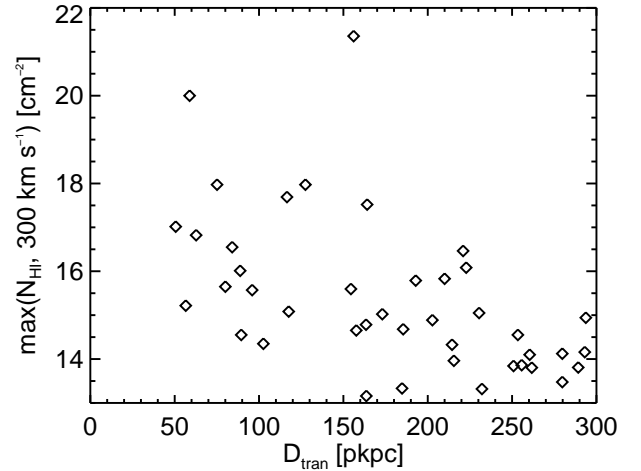


**Figure 11.** The individual measured values of  $\max(N_{\text{HI}}, 300 \text{ km s}^{-1})$  for galaxies with  $D_{\text{tran}} < 300 \text{ pkpc}$ .

A relevant question concerns the dependence of these statistics on the size of the velocity window considered. In Figure 9 we considered the maximum column density absorber within  $\pm 700 \text{ km s}^{-1}$  of the systemic velocity of each galaxy. This corresponds to the full width of the velocity distribution shown in Figure 6. However, it is clear from Figures 6 and 7 that the majority of the excess *strength* of absorption falls within  $\pm 300 \text{ km s}^{-1}$ , especially for those systems with small impact parameters. Figure 10 shows  $\max(N_{\text{HI}}, 300 \text{ km s}^{-1})$ ; the trends are similar, though in the more restricted velocity window the peak on small scales is higher relative to random IGM locations—the median value in the first bin is 3 dex higher than the random redshift sample, and the extended floor of absorption is increased to at least .5 dex above the median of

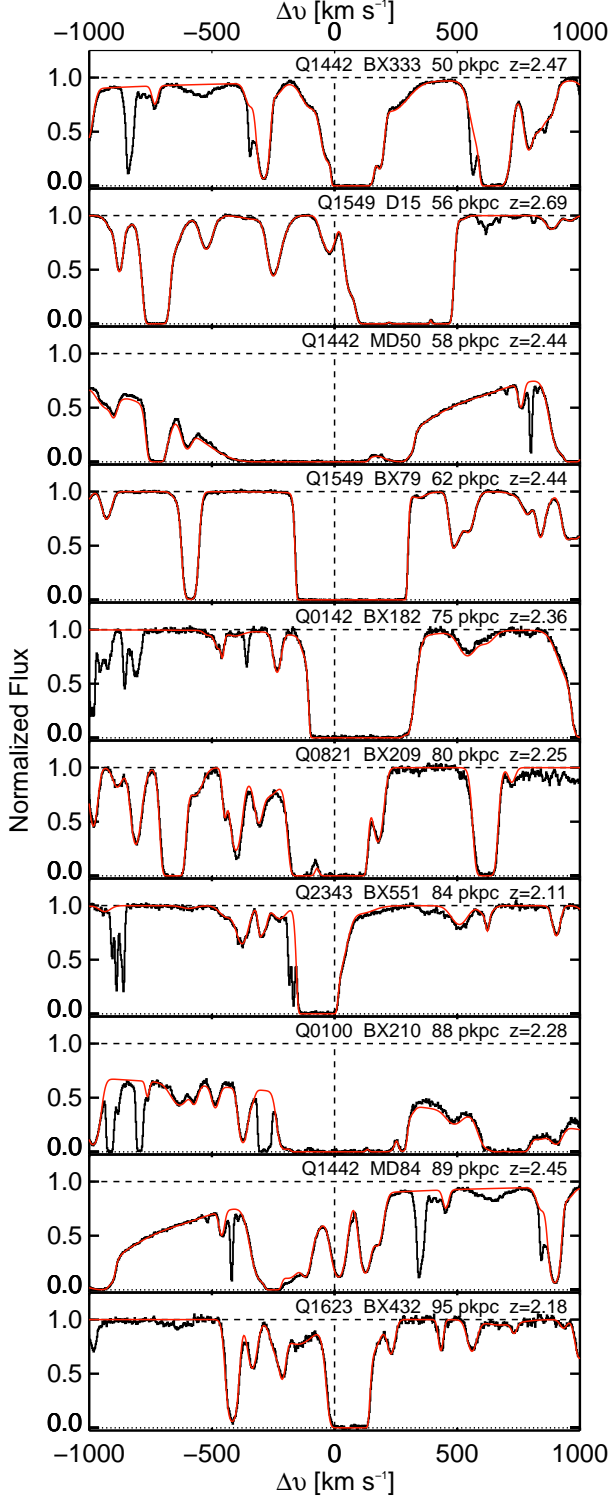


**Figure 12.** Ly $\alpha$  absorption within  $\pm 1000$  km s $^{-1}$  of the systemic redshift of the 10 galaxies within  $D_{\text{tran}} < 100$  pkpc of the line of sight to the QSO. The HIRES data are in black, while the red shows our Voigt profile decomposition of the H I absorption near the redshift of the galaxy. The continuum and zero level of the spectrum are shown in dashed and dotted lines respectively. The systemic redshift of each galaxy is marked by the vertical dashed line at 0 km s $^{-1}$ . Note that the continuum is depressed in some of the spectral regions surrounding Q1442-BX333, Q1442-MD50, Q0100-BX210, and Q1442-MD84 by a DLA or sub-DLA near the galaxy redshift as described in §2.3.

the random-redshift distribution. The more significant excess over random of the 300 km s $^{-1}$  version is primarily due to the exclusion of unrelated absorbers at large velocity separation; however, we note that at  $D_{\text{tran}} > 1200$  pkpc, the differential Hubble velocity associated with this distance along the line of sight is  $> 300$  km s $^{-1}$ , meaning that for large  $D_{\text{tran}}$  it may be more appropriate to adopt  $\max(N_{\text{HI}}, 700 \text{ km s}^{-1})$  as the relevant statistic. Regarding the sum statistic for the smaller velocity window (not shown), the value of the plateau and that of the random sample is  $\sim 0.3$  dex higher for  $\text{sum}(N_{\text{HI}}, 300 \text{ km s}^{-1})$  than for  $\max(N_{\text{HI}}, 300 \text{ km s}^{-1})$ , similar to the variation in the statistics shown in Figure 9.

As we will argue in §5 and §8.1, the velocity and spatial scales of 300 km s $^{-1}$  and 300 kpc capture the most significant excess in both the column density and the number of absorbers near galaxies. In Figure 11 we provide the individual measurements  $\max(N_{\text{HI}}, 300 \text{ km s}^{-1})$  for all galaxies in the sample with  $D_{\text{tran}} < 300$  pkpc. Note the large intrinsic scatter in  $\max(N_{\text{HI}})$ , even at fixed impact parameter. For the 10 galaxies with the smallest impact parameters ( $D_{\text{tran}} < 100$  pkpc), the relevant portions of the QSO spectra within  $\pm 1000$  km s $^{-1}$  of Ly $\alpha$  at  $z_{\text{gal}}$  are reproduced in Figure 12.

#### 4.2.1. The large-scale distribution of H I

We now consider the larger-scale distribution H I around galaxies. Unfortunately, the sampling of galaxies with  $D_{\text{tran}} > 2$  pMpc is comparatively poor in our sample due to the survey geometry of most of the KBSS fields (typically  $5.5 \times 7.5$  arcmin on the sky). This scale is imposed by the footprint of LRIS; with each field roughly centered on the bright QSO, the maximum observed impact parameter would be  $\simeq 2.15$  pMpc at  $\langle z \rangle = 2.3$ . However, three out of 15 survey fields (see Table 1) were imaged with other instruments covering larger angular sizes and thus provide information on larger transverse scales. In Figures 9 and 10 we use wider bin sizes for absorbers with  $D_{\text{tran}} > 1$  pMpc in order to consider the large-scale distribution. This reduces the shot noise in the bins with  $D_{\text{tran}} > 2$  pMpc. Figures 9 and 10 demonstrate that  $\max(N_{\text{HI}})$  remains higher than the global median value in the IGM (dark horizontal line) out to  $\sim 2$  pMpc, and then begins to decline. For larger  $D_{\text{tran}}$ , the data suggest column densities at or below that of random places in the IGM.

Again, considering the degree of scatter in  $\max(N_{\text{HI}})$  at fixed impact parameter, Figure 13 shows  $\max(N_{\text{HI}}, 700 \text{ km s}^{-1})$  for various bins in  $D_{\text{tran}}$ , as indicated. The top row of panels correspond to  $D_{\text{tran}} < 300$  pkpc, while the bottom two rows of panels consider larger impact parameters. Each panel shows the Kolmogorov-Smirnov probability that the two histograms are drawn from the same parent distribution. Notably, only the  $2 < D_{\text{tran}} < 3$  pMpc bins have a distribution of  $\max(N_{\text{HI}})$  consistent with the random sample.

Thus, we have shown that the column density of H I peaks sharply at the position of galaxies in the transverse direction, that the width of the peak is  $\simeq 300$  pkpc, and that there remains a significant excess of H I gas to  $D_{\text{tran}} \simeq 2$  pMpc. In §8 we discuss the implications of these results.

#### 4.3. 3D Distribution of $N_{\text{HI}}$

The 3D distance,  $D_{3\text{D}}$ , is computed using the quadrature sum of the physical impact parameter ( $D_{\text{tran}}$ ) and the line-of-sight distance calculated assuming the velocity differences  $\Delta v$  are due entirely to the Hubble flow,

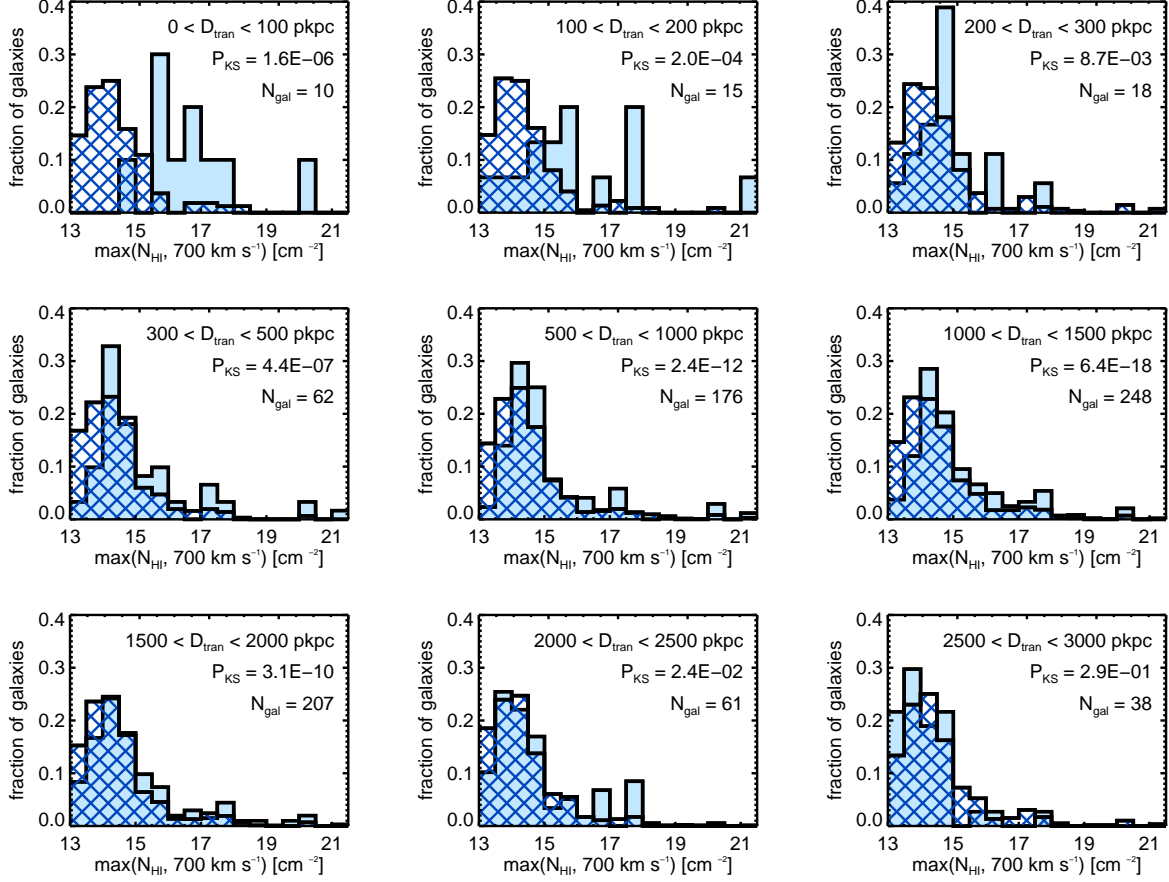


**Figure 13.** The  $\max(N_{\text{HI}}, 700 \text{ km s}^{-1})$  statistic as a function of impact parameter (different panels). The hatched histograms are the values for the random sample, the solid histograms are the values for the real sample. These histograms quantify the variation from galaxy to galaxy of the  $\max(N_{\text{HI}})$  statistic at fixed impact parameter.  $P_{\text{KS}}$  is the probability that the two  $\max(N_{\text{HI}})$  sets were drawn from the *same* distribution. Notably, the last panel with the highest value of  $D_{\text{tran}}$  has the least significant departure from the random distribution.

$$D_{\text{Hubble}}(\Delta v, z) \equiv \frac{\Delta v}{H(z)}. \quad (7)$$

The 3D distance is therefore

$$D_{3\text{D}}(\Delta v, z, D_{\text{tran}}) \equiv \sqrt{D_{\text{tran}}^2 + \left(\frac{\Delta v}{H(z)}\right)^2}, \quad (8)$$

where  $H(z)$  is given by

$$H(z) = H_0 \sqrt{\Omega_m(1+z)^3 + \Omega_\Lambda} \quad (9)$$

such that  $H(z = 2.3)$  in our cosmology is

$$H(z = 2.3) = 240 \text{ km s}^{-1} \text{ Mpc}^{-1}. \quad (10)$$

In this formalism, each absorber has a unique  $D_{3\text{D}}$  with respect to a galaxy in the same field.

The 3D distance, due to its strong dependence on  $|\Delta v|$ , requires that absorbers have *both* small  $D_{\text{tran}}$  *and* very small values of  $|\Delta v|$  in order to populate bins at small values of  $D_{3\text{D}}$ . As a result,  $D_{3\text{D}}$  has the effect of isolating those absorbers *most likely* to be associated with the galaxy without imposing a velocity cut.

Figure 14 shows that the median  $N_{\text{HI}}$  stays above that of an average place in the universe out to  $D_{3\text{D}} \simeq 3 \text{ pMpc}$ .<sup>25</sup> The

decline of  $N_{\text{HI}}$  as a function of  $D_{3\text{D}}$  is quite smooth, but again strongly peaked at the position of galaxies. The pixel analysis of the KBSS sample recently completed by Rakic et al. (2011b) studies in detail the 3D distribution of H I optical depths. There is excellent agreement between the optical depths measured in Rakic et al. (2011b) and the  $N_{\text{HI}}$  trends shown in Figure 14. The smoothness of the decline is caused by the shifting of absorbers with small  $D_{\text{tran}}$  and modest  $|\Delta v|$  into bins at larger  $D_{3\text{D}}$ . Thus, the signal appearing in the inner 300 pkpc in Figure 9 is distributed across a larger number of bins in  $D_{3\text{D}}$  as a result of the velocity distribution of the absorbers.

The nature of the velocity width of the excess absorption will be discussed at length in §6; however, it should be noted that all measurements of  $|\Delta v|$  rely on the accuracy of the galaxy redshifts and in addition are affected by whatever peculiar velocities are present, whether due to random motion, inflows, or outflows.

#### 4.4. Connection to Galaxy-Galaxy Pair Results

Steidel et al. (2010) presented a sample of 512 close angular pairs of galaxies with different redshifts (drawn primarily from the same KBSS catalogs used in the present paper), using the spectrum of the background galaxy to probe gas associated with that in the foreground. They were able to mea-

<sup>25</sup> Note, this is consistent with the quadratic sum of the extent of the ve-

locity and transverse distance excesses seen in previous sections.

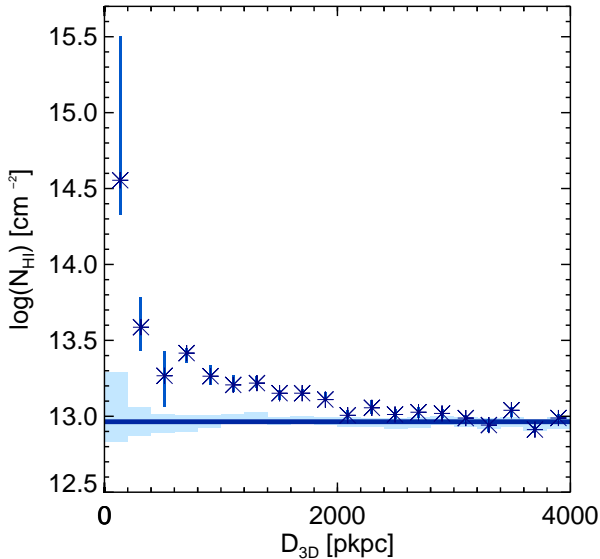


**Figure 14.** The median column density of all absorption systems within  $\pm 1400 \text{ km s}^{-1}$  of a galaxy as a function of the 3D distance between the absorber and the galaxy. The symbols have the same meaning as those in Figure 9. Note the steeply rising column densities at small  $D_{3D}$  and that the median value remains above that of a random location (horizontal bar) out to  $\sim 3 \text{ pMpc}$ .

sure the strength of absorption from H I and several metallic species over a range in impact parameter  $D_{\text{tran}} = 8 - 125 \text{ pkpc}$ . The principal advantage of this method is that it allows for probes at very small angular separation ( $\theta < 5''$ )—obtaining statistical results for galaxies at such small separations from QSOs is difficult due both to the “glare” of the QSO and the relative rarity of QSO-galaxy pairs with very small separations (the smallest QSO sightline–galaxy separation is  $D_{\text{tran}} = 50 \text{ pkpc}$  or  $\theta \approx 6''$ ). As such, the galaxy pair results are highly complementary to the QSO sightline study described in this paper.

Using background *galaxies* instead of QSOs results in two important differences between these studies: first, background galaxies have a projected “beam size” of  $\sim 1 \text{ kpc}$  at the location of the foreground galaxy, whereas background QSOs have a projected beam of order  $\sim 1 \text{ pc}$ . As a result, the absorption seen against background galaxies measures a combination of the covering fraction of gas on kpc scales and the column density of absorbers. Further, background galaxies are faint and therefore only low-dispersion, low-S/N spectra can be obtained. Steidel et al. (2010) thus used stacks of background galaxy spectra shifted into the rest frame of the foreground galaxies to quantify the average absorption profile surrounding these galaxies. The lower-resolution spectra do not separate into individual components as would be found in individual QSO spectra. As such, the galaxy pair method allows for the measurement of equivalent widths ( $W_0$ ) only. As discussed by Steidel et al. (2010) interpretation of  $W_0$  is complicated by its sensitivity to the covering fraction and velocity extent of the absorbing material, and its relative *insensitivity* to ionic column density.

Steidel et al. (2010) measured  $W_0$  of H I, C IV, C II, Si IV, and Si II in bins of impact parameter ( $D_{\text{tran}}$ ). The large  $W_0$ , particularly at  $D_{\text{tran}} \lesssim 40 \text{ pkpc}$ , seemed to require high line-of-sight velocity spread in the gas—likely higher than could be easily explained by gravitationally-induced motions, but

easily accounted for by the high velocities observed “down the barrel” in the spectra of LBGs, which typically reach  $\Delta v \sim 800 \text{ km s}^{-1}$  for galaxies with properties similar to those in our sample.

Steidel et al. (2010) found that a simple geometric and kinematic model of outflows from LBGs could account simultaneously for the behavior of  $W_0$  as a function of  $D_{\text{tran}}$  as well as the shape of the blue-shifted line profiles of strong interstellar absorption features observed along direct sightlines to the same galaxies. The presence of detected C II absorption to  $D_{\text{tran}} \sim 90 \text{ pkpc}$  was cited as evidence for a non-negligible covering fraction of H I gas having  $N_{\text{HI}} > 10^{17} \text{ cm}^{-2}$  at such large galactocentric distances. Steidel et al. (2010) remarked that  $90 \text{ kpc}$  is very close to the expected virial radius  $r_{\text{vir}}$  for LBGs similar to those in the current sample. Our  $\max(N_{\text{HI}})$  statistic agrees well with this inference (Figure 9); in fact, we find a covering fraction  $\simeq 30\%$  for absorbers with  $N_{\text{HI}} > 10^{17.2} \text{ cm}^{-2}$  for  $r \lesssim r_{\text{vir}}$ —see § 5.2.

In addition, Steidel et al. (2010) used the same HIRES spectra as this work to show that the  $W_0(\text{Ly}\alpha)$  measured from the relevant portions of the high resolution spectra, averaged in the same way as the background galaxy spectra, are consistent with an extrapolation to  $D_{\text{tran}} \simeq 250 \text{ pkpc}$  of the trend seen in the galaxy-galaxy pairs results; a similar conclusion was reached by Rakic et al. (2011b), also using equivalent width analysis of the QSO spectra, where a smooth trend was noted out to  $D_{\text{tran}} > 1 \text{ pMpc}$ .

#### 4.5. Comparison to previous studies at $z > 2$

Adelberger et al. (2003, 2005a) conducted the first systematic studies of high- $z$  galaxies and their surrounding IGM using sightline surveys of the  $2 < z < 4$  IGM paired with large LBG surveys designed to probe galaxies in the same volume. Adelberger et al. (2003) analyzed the transmitted flux in the  $\text{Ly}\alpha$  forest of background QSOs, evaluated near the redshifts of survey galaxies. At the time, this was most easily accomplished using  $z \sim 3$  LBGs and  $z \simeq 3.5$  background QSOs. These authors did not attempt Voigt profile decompositions (as in the present work) but focused on transmitted flux because it made for easier comparisons to theory and because the spectra covered the  $\text{Ly}\alpha$  transition only, making measurements of column density or optical depth difficult due to limited dynamic range for any  $N_{\text{HI}} \gtrsim 10^{14.5} \text{ cm}^{-2}$ . Based on 8 QSO sightlines covering  $3 \lesssim z \lesssim 3.6$ , Adelberger et al. (2003) found that excess H I absorption (i.e., lower transmitted flux than the average IGM at the same redshift) was present within  $\lesssim 5h^{-1} \text{ comoving Mpc}$  (cMpc) of galaxies [ $1.7 \text{ physical Mpc}$  (pMpc) at  $\langle z \rangle = 3.3$  using the cosmology adopted in the present work], and an intriguing but not highly significant lack of H I very close to these galaxies ( $< 0.5h^{-1} \text{ cMpc}$  or  $< 170 \text{ pkpc}$ ). C IV absorption was observed to be correlated with galaxy positions to out to  $2.4h^{-1} \text{ cMpc}$  (or  $800 \text{ physical kpc}$ ). The cross-correlation of C IV systems with LBGs was found to be similar to the LBG auto-correlation, suggesting that metal enriched IGM and galaxies shared the same volumes of space. The strongest C IV absorbers were so strongly correlated with LBG positions that the authors concluded that they must be causally connected to one another.

Adelberger et al. (2005a) extended similar studies to  $1.8 \leq z \leq 3.3$ , using a larger number of QSO sightlines and a wider range of QSO spectra for the analysis. Based once again on the transmitted flux statistics, the large-scale excess  $N_{\text{HI}}$  near galaxies was consistent with the results of Adelberger et al.

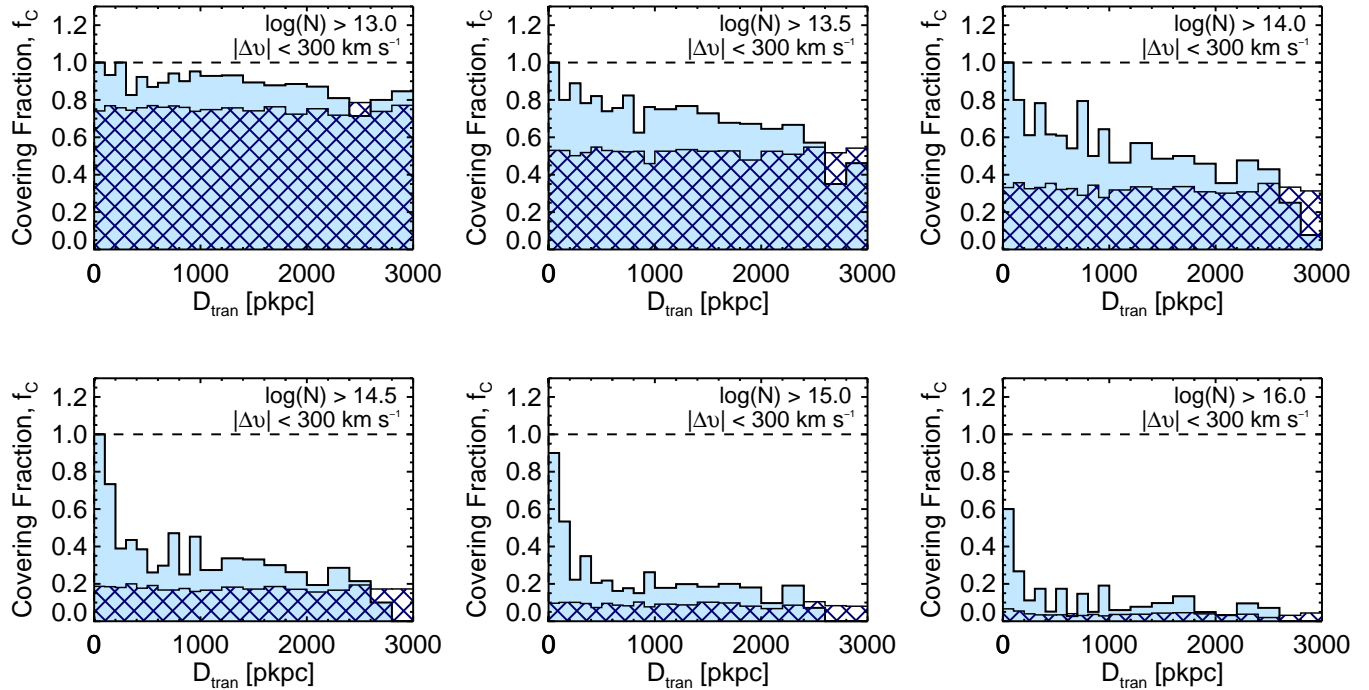


**Figure 15.** The covering fraction,  $f_c$ , of absorbers for various  $N_{\text{HI}}$  thresholds (different panels) as a function of  $D_{\text{tran}}$ . The solid histogram represents the fraction of galaxies with an absorber of a given  $N_{\text{HI}}$  or greater, within  $\pm 300 \text{ km s}^{-1}$ . The hatched histogram represents  $f_c$  at random locations in the IGM; the horizontal dashed line marks  $f_c = 1$  (100% covering). The bin size is 100 pkpc for absorbers with  $D_{\text{tran}} < 1 \text{ pMpc}$  and 200 pkpc for those with  $D_{\text{tran}} > 1 \text{ pMpc}$ .

(2003), but the “turnover” of H I absorption on the smallest scales was not confirmed using the larger sample at somewhat lower redshift. Generally, the transmitted flux was decreasing with galactocentric distance, though it was still the case that  $\sim 30\%$  of the galaxies with the smallest impact parameters showed a lack of strong absorption, interpreted as evidence that the gas is clumpy. The results for C IV were extended, and it was shown that the correlation with galaxies grows increasingly strong as  $N_{\text{CIV}}$  increases; the correlation length of  $N_{\text{CIV}} \gtrsim 10^{12.5} \text{ cm}^{-2}$  absorption systems was similar to that of the autocorrelation length of the galaxies. The authors attempted to correlate the observed IGM properties with galaxy properties, but no significant correlations were found given the relatively small sample of galaxies at small impact parameters.

There is no overlap in the data sample used in this paper with that of Adelberger et al. (2003) which focused on higher-redshift galaxies and QSOs. Three of the fields (Q1623, HS1700, and Q2343) included in our analysis were also included in Adelberger et al. (2005a) which considered similar redshifts to this work; however, we have increased the S/N of the QSO spectra and also added many galaxy redshifts to our catalogs for these fields since the earlier analysis. The most surprising result of the Adelberger et al. (2003) sample, especially in light of the work presented here, was the reported *deficit* of absorption found within  $0.5 h^{-1} \text{ cMpc}$  or  $170 \text{ pkpc}$  of galaxies. Adelberger et al. (2005a), with a larger data set, found that 1/3 of galaxies had relatively-little H I absorption (consistent with the pixel statistics of our sample presented in Rakic et al. 2011b), but that the majority of galaxies were associated with significant absorption. In our sample, only 1/21 galaxies with  $D_{\text{tran}} < 170 \text{ pkpc}$  has a  $\text{sum}(N_{\text{HI}}, 300 \text{ km s}^{-1})$  value less than the median of the random sample. As such we

concur with the argument of Adelberger et al. (2005a) suggesting that the reported deficit was due to the small sample size presented. Further, we note that a measure of  $N_{\text{HI}}$  shows that the majority of galaxies do have excess H I absorption in their surroundings.

On larger physical scales, Adelberger et al. (2003) and Crighton et al. (2011) considered the large-scale distribution of H I absorbers at  $z \approx 3$  while Adelberger et al. (2005a) studied that at  $z \approx 2.5$ . All found evidence for increased absorption to  $D_{3\text{D}} \approx 5\text{-}6 h^{-1} \text{ cMpc}$  or  $\sim 2 \text{ pMpc}$ . This scale is roughly consistent with our measurements of the 3D distribution of absorption presented in Figure 14, as well as with the trends in optical depth vs.  $D_{3\text{D}}$  presented in Rakic et al. (2011b).

## 5. THE COVERING FRACTION AND INCIDENCE OF H I

As discussed in §4.1, the scale of the strongest correlation between  $N_{\text{HI}}$  and the positions of galaxies is found within  $300 \text{ km s}^{-1}$  of  $z_{\text{gal}}$ . Adopting this value as the characteristic velocity scale for circumgalactic gas, we can examine other useful measures of the gas distribution around galaxies. The covering fraction ( $f_c$ ) and the incidence of absorbers ( $\eta_{\text{abs}}$ ) are two ways of quantifying the geometry of the distribution as a function of both impact parameter and  $N_{\text{HI}}$ .

First, we define the covering fraction,  $f_c(D_{\text{tran}}, N_0)$ , as the fraction of galaxies in a bin of impact parameter,  $D_{\text{tran}}$ , that have an absorber within  $|\Delta v| < 300 \text{ km s}^{-1}$  with  $N_{\text{HI}} > N_0$ . This is equivalent to the geometric fraction of the area of an annulus centered on the galaxy that is covered by gas with  $N_{\text{HI}} > N_0$  and  $|\Delta v| < 300 \text{ km s}^{-1}$ . This quantity measures the *variation* within the sample of the decline of  $N_{\text{HI}}$  as a function of  $D_{\text{tran}}$ .

A related quantity is the incidence of absorbers,  $\eta_{\text{abs}}$ , defined to be the number of absorbers *per galaxy* within a given

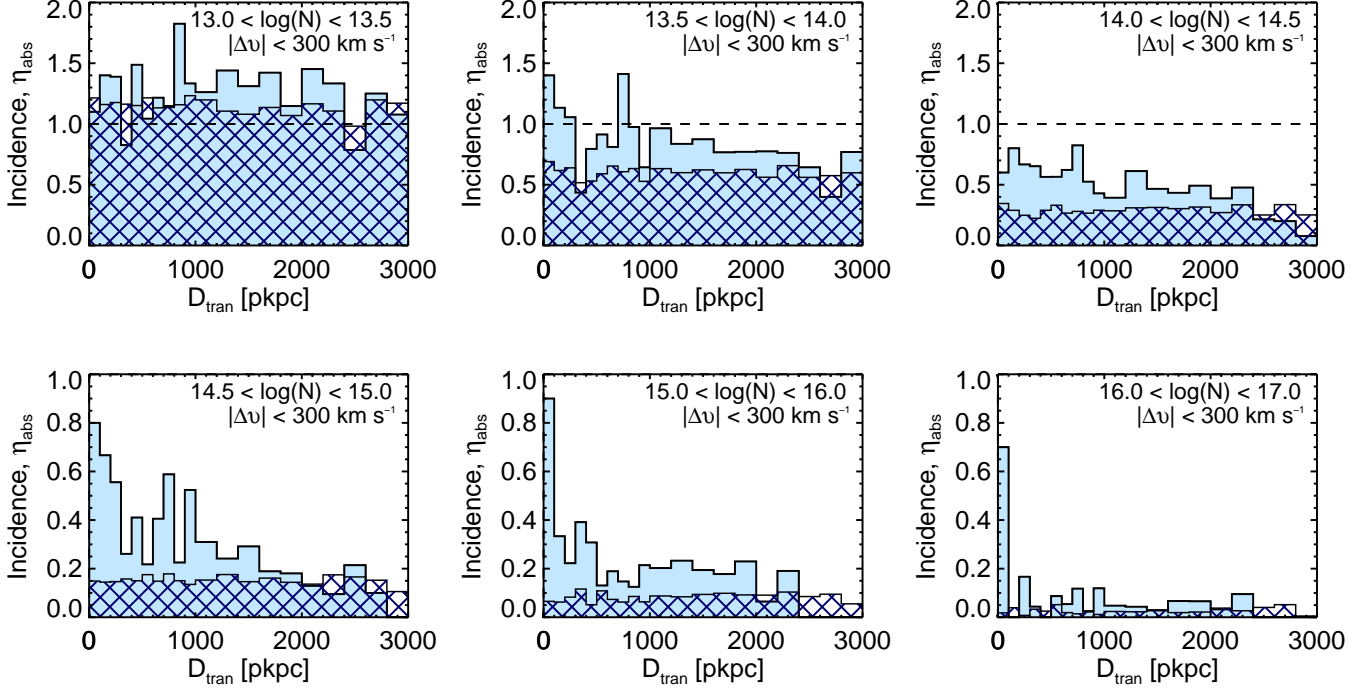


**Figure 16.** The incidence of H I absorbers,  $\eta_{\text{abs}}$ , as a function of impact parameter,  $D_{\text{tran}}$ . The solid histogram represents the mean number of absorbers per galaxy within  $\pm 300 \text{ km s}^{-1}$  at the given distance, whereas the hatched histogram represents the average incidence of absorbers near randomly-chosen redshifts. The different panels show various ranges of  $N_{\text{HI}}$ . The bin size is 100 pkpc for absorbers with  $D_{\text{tran}} < 1 \text{ pMpc}$  and 200 pkpc for those with  $D_{\text{tran}} > 1 \text{ pMpc}$ . The incidence of absorbers exceeds the random distribution for  $N_{\text{HI}} > 10^{13.5} \text{ cm}^{-2}$  to  $D_{\text{tran}} > 2 \text{ pMpc}$ . Note that only absorbers with  $\log(N_{\text{HI}}) > 14.5$  show strong association with the positions of galaxies. Table 2 gives the data values for  $f_c$  and  $P_E$  determined from these distributions.

**Table 2**  
Absorber Incidence ( $\eta_{\text{abs}}$ ) and Excess Probability ( $P_E$ ) for  $|\Delta v| < 300 \text{ km s}^{-1}$ <sup>a</sup>

$\log(N_{\text{HI}})$ range <sup>b</sup> [ $\text{cm}^{-2}$ ]	$\eta_{\text{abs}}$ $D_{\text{tran}} < 0.1 \text{ pMpc}$	$P_E$	$\eta_{\text{abs}}$ $D_{\text{tran}} < 0.3 \text{ pMpc}$	$P_E$	$\eta_{\text{abs}}$ $D_{\text{tran}} < 2 \text{ pMpc}$	$P_E$
13.0—13.5	$1.1 \pm 0.3$	$-0.1 \pm 0.3$	$1.3 \pm 0.2$	$0.1 \pm 0.1$	$1.33 \pm 0.04$	$0.17 \pm 0.04$
13.5—14.0	$1.4 \pm 0.4$	$1.0 \pm 0.5$	$1.2 \pm 0.2$	$0.8 \pm 0.3$	$0.87 \pm 0.03$	$0.44 \pm 0.06$
14.0—14.5	$0.6 \pm 0.2$	$0.7 \pm 0.7$	$0.7 \pm 0.1$	$1.4 \pm 0.4$	$0.53 \pm 0.03$	$0.80 \pm 0.09$
14.5—15.0	$0.8 \pm 0.3$	$4.4 \pm 1.9$	$0.7 \pm 0.1$	$3.4 \pm 0.8$	$0.32 \pm 0.02$	$1.03 \pm 0.13$
15.0—16.0	$0.9 \pm 0.3$	$12.7 \pm 4.6$	$0.4 \pm 0.1$	$4.9 \pm 1.4$	$0.22 \pm 0.02$	$1.59 \pm 0.20$
16.0—17.0	$0.7 \pm 0.3$	$38.2 \pm 14.8$	$0.2 \pm 0.1$	$9.7 \pm 3.4$	$0.06 \pm 0.01$	$1.78 \pm 0.40$

<sup>a</sup> The values in this table refer to Figure 16

<sup>b</sup>  $\log(N_{\text{HI}})$  range: The range of  $N_{\text{HI}}$  considered; And the incidence,  $\eta_{\text{abs}}$ , and excess probability,  $P_E$  considered over three ranges of  $D_{\text{tran}}$ . The quoted uncertainties in  $\eta_{\text{abs}}$  and  $P_E$  are calculated assuming Poisson statistics.

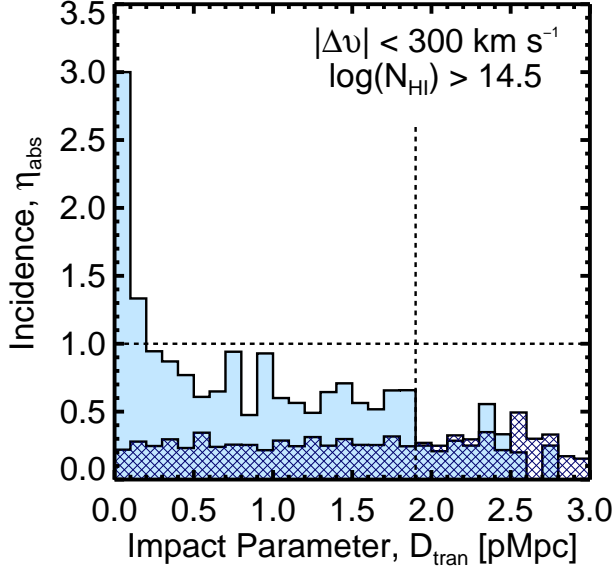
range of  $N_{\text{HI}}$  and  $D_{\text{tran}}$ , and with  $|\Delta v| < 300 \text{ km s}^{-1}$ . Because this quantity can be greater than unity, it has larger dynamic range and so allows for a more-complete picture of the *average multiplicity* of absorbers at locations close to galaxies. Also, because we consider  $\eta_{\text{abs}}$  in differential bins of  $N_{\text{HI}}$ , it can be used to measure the degree to which absorbers of a given  $N_{\text{HI}}$  associate with galaxies.<sup>26</sup>

Figure 15 illustrates the dependence of  $f_c$  on  $D_{\text{tran}}$  for various thresholds of  $N_{\text{HI}}$  (different panels). Within 100 pkpc,  $f_c > 0.5$  even for  $N_{\text{HI}} > 10^{16} \text{ cm}^{-2}$ . Also, *every galaxy* has an absorber with  $\log(N_{\text{HI}}) > 14.5$  within 100 pkpc and  $|\Delta v| < 300 \text{ km s}^{-1}$ . The distribution within 2.5 pMpc of lower- $N_{\text{HI}}$

<sup>26</sup> To illustrate the difference between  $f_c$  and  $\eta_{\text{abs}}$ , suppose that all absorbers have the same  $N_{\text{HI}}$ . Then for a sample of two galaxies, one with 3 absorbers and the other with none,  $f_c = 0.5$  and  $\eta_{\text{abs}} = 1.5$ .

absorbers is relatively uniform, with  $f_c > 0.5$ . However, at larger threshold  $N_{\text{HI}}$  (bottom three panels) we see that  $f_c$  is high ( $\gtrsim 0.5$ ) only within  $\sim 200 \text{ pkpc}$ . We will return to our measured values of  $f_c$  in §5.2 and §5.3 where we compare our measurements to those made at low- $z$  and also to results from numerical simulations.

Figure 16 shows the average incidence of absorbers,  $\eta_{\text{abs}}$ , as a function of distance,  $D_{\text{tran}}$ , and ranges of  $N_{\text{HI}}$  (different panels). Notably, in all panels (i.e., at all column densities) the average  $\eta_{\text{abs}}$  is higher than random for  $D_{\text{tran}} < 2 \text{ pMpc}$ . For absorbers with  $N_{\text{HI}} > 10^{14.5} \text{ cm}^{-2}$  (three bottom panels), there is a clear peak at small values of  $D_{\text{tran}}$ . No similar peak is present in the distributions of absorbers with  $N_{\text{HI}} < 10^{14.5} \text{ cm}^{-2}$  (top panels). Clearly absorbers with  $N_{\text{HI}} > 10^{14.5} \text{ cm}^{-2}$  are more tightly correlated with the positions of galaxies than absorbers of lower column densities.



**Figure 17.** The incidence of absorbers,  $\eta_{\text{abs}}$ , with  $N_{\text{HI}} > 10^{14.5} \text{ cm}^{-2}$  as a function of impact parameter. The solid histogram represents the distribution of these high- $N_{\text{HI}}$  absorbers for  $|\Delta v| < 300 \text{ km s}^{-1}$ . The hatched histogram represents the average incidence of the same absorbers near randomly-chosen redshifts. The vertical dotted line indicates the distance at which the incidence of the real distribution becomes comparable with that of the random distribution,  $D_{\text{tran}} \approx 2 \text{ pMpc}$ . The dotted horizontal line marks  $\eta_{\text{abs}} = 1$ .

These distributions can also be used to determine the excess probability (over that of a random place in the IGM) of intersecting an absorber of a given column density, within a range of  $D_{\text{tran}}$  and within some  $|\Delta v|$ . The excess probability,  $P_E$ , is defined through comparison to the random distribution:

$$P_E = \frac{\eta_{\text{abs}} - \eta_{\text{abs,random}}}{\eta_{\text{abs,random}}} \quad (11)$$

Table 2 summarizes the measured values of  $\eta_{\text{abs}}$  and  $P_E$  for absorbers binned in  $N_{\text{HI}}$  for the velocity window  $|\Delta v| < 300 \text{ km s}^{-1}$  and three distance cuts:  $D_{\text{tran}} < 100 \text{ pkpc}$ ,  $D_{\text{tran}} < 300 \text{ pkpc}$ , and  $D_{\text{tran}} < 2 \text{ pMpc}$ .

### 5.1. Absorbers with $N_{\text{HI}} > 10^{14.5} \text{ cm}^{-2}$

We have shown above that absorbers with  $N_{\text{HI}} > 10^{14.5} \text{ cm}^{-2}$  appear to trace the positions of galaxies in our sample with high fidelity. The incidence of absorbers with  $N_{\text{HI}} > 10^{14.5} \text{ cm}^{-2}$  and  $|\Delta v| < 300 \text{ km s}^{-1}$ , as shown in Figure 17, nicely encapsulates the “shape” of the CGM. Similar to Figure 9 for  $D_{\text{tran}} < 300 \text{ pkpc}$ , one sees rising values of  $\eta_{\text{abs}}$  as the galactocentric distance is reduced. From  $300 \text{ pkpc} < D_{\text{tran}} < 2 \text{ pMpc}$ ,  $\eta_{\text{abs}}$  reaches a plateau value with  $\eta_{\text{abs}} \gtrsim 0.5$  [ $2 \text{ pMpc} = 1.4 \text{ h}^{-1} \text{ pMpc} \approx 4.6 \text{ h}^{-1} \text{ cMpc}$  (at  $z = 2.3$ )]. For  $D_{\text{tran}} > 2 \text{ pMpc}$ ,  $\eta_{\text{abs}}$  drops to values consistent with the average IGM.

Recalling the quantity  $P(\Delta v, D_{\text{tran}})$ , defined in §4.1 as the probability, per galaxy, of intersecting an absorber at a given  $\Delta v$  and within the specified range of  $D_{\text{tran}}$ , here we consider the velocity distribution of absorbers with  $N_{\text{HI}} > 10^{14.5} \text{ cm}^{-2}$  in bins of  $D_{\text{tran}}$  as shown in Figure 18.

Fitting a Gaussian to the excess absorbers near galaxies compared to random gives a deviation ( $\sigma_{\langle \Delta v \rangle}$ ) of  $187 \text{ km s}^{-1}$  again suggesting that the velocity scale of the excess is  $\Delta v \approx \pm 300 \text{ km s}^{-1}$ .

Integrating the distribution in the first panel of Figure 18

**Table 3**  
Incidence ( $\eta_{\text{abs}}$ ) and Excess Probability for  $N_{\text{HI}} > 10^{14.5} \text{ cm}^{-2}$  <sup>a</sup>

$D_{\text{tran}}^b$ [pkpc]	$\langle \Delta v \rangle$ [km s <sup>-1</sup> ]	$\sigma_{\langle \Delta v \rangle}$ [km s <sup>-1</sup> ]	$\Delta v$ window [km s <sup>-1</sup> ]	$\eta_{\text{abs}}$	$P_E$
0–300	$4 \pm 33$	$164 \pm 28$	-350 to 350	$1.70 \pm 0.02$	4.1
300–600	$-74 \pm 50$	$253 \pm 49$	-550 to 450	$1.07 \pm 0.01$	1.19
600–900	$29 \pm 49$	$389 \pm 49$	-750 to 850	$1.31 \pm 0.01$	0.80
900–1200	$-43 \pm 78$	$407 \pm 87$	-850 to 750	$1.60 \pm 0.01$	1.14
1200–1500	$61 \pm 78$	$335 \pm 80$	-650 to 750	$1.20 \pm 0.01$	0.76
1500–1800	$42 \pm 96$	$344 \pm 109$	-650 to 750	$1.06 \pm 0.01$	0.63

<sup>a</sup> The values in this table refer to Figure 18.

<sup>b</sup>  $D_{\text{tran}}$ : The  $D_{\text{tran}}$  window considered;  $\langle \Delta v \rangle$ : the Gaussian velocity centroid and its associated error;  $\sigma_{\langle \Delta v \rangle}$ : the standard deviation of the Gaussian fit and its associated error;  $\Delta v$  window: the velocity window used to compute  $\eta_{\text{abs}}$  and  $P_E$  (comparable to  $\pm 2\sigma$ );  $\eta_{\text{abs}}$ : the incidence,  $P_E$ : the excess probability. The quoted uncertainties in  $\eta_{\text{abs}}$  are calculated assuming Poisson statistics. The error in  $P_E$  is dominated by the variation in individual realizations of the random sample: typically the variation in  $P_E$  is  $\sim 0.05$  except for the first bin ( $0 < D_{\text{tran}} < 300 \text{ pkpc}$ ) where the variation is  $\sim 0.2$ .

corresponding to  $D_{\text{tran}} < 300 \text{ kpc}$  results in an incidence averaged over  $\pm 350 \text{ km s}^{-1}$  ( $\sim 2\sigma$ ) and  $300 \text{ pkpc}$ ,  $\eta_{\text{abs}} = 1.6$ . Similarly, comparing the value of  $\eta_{\text{abs}}$  measured in the real and random distribution one infers that strong absorbers ( $N_{\text{HI}} > 10^{14.5}$ ) are  $> 4$  times ( $P_E = 4.1$ ) more likely to be found within  $300 \text{ kpc}$  and  $\pm 350 \text{ km s}^{-1}$  of a galaxy in our sample, than at a random place. The parameters of the Gaussian fits in Figure 18, as well as the inferred  $\eta_{\text{abs}}$  and  $P_E$ , are listed in Table 3.

In this section, we have shown that the covering fraction,  $f_c$ , of absorbers with  $\log(N_{\text{HI}}) < 14.5$  is roughly uniform and  $> 0.5$  out to  $D_{\text{tran}} \approx 2 \text{ pMpc}$ , but that those with higher  $N_{\text{HI}}$  only have  $f_c > 0.5$  within  $D_{\text{tran}} < 200 \text{ kpc}$  (Figure 15). Consideration of the incidence,  $\eta_{\text{abs}}$ , indicates that absorbers with  $\log(N_{\text{HI}}) > 14.5$  are more directly related to galaxies (Figure 16). Those absorbers nicely encapsulate the “shape” of the CGM (Figure 17) and are  $> 4$  times more likely to be found within  $|\Delta v| < 350 \text{ km s}^{-1}$  and  $D_{\text{tran}} < 300 \text{ pkpc}$  of a galaxy in our sample than at a random place in the IGM (Figure 18).

### 5.2. Covering Fractions: Comparison with Simulations

Motivated by the desire to predict the observational signatures of cold accretion streams, two recent theoretical papers have considered the covering fraction of absorbers of various  $N_{\text{HI}}$  surrounding galaxies. Faucher-Giguère & Kereš (2011) consider the covering fraction of Lyman Limit (LLS,  $17.2 < \log(N_{\text{HI}}) < 20.3$ ) and Damped Lyman Alpha (DLA,  $\log(N_{\text{HI}}) > 20.3$ ) absorbers originating within cold streams near two simulated star-forming galaxies at  $z = 2$  using cosmological zoom-in simulations that do not include galactic winds. Since these authors explicitly *did not* consider galactic winds, their covering fractions are approximately<sup>27</sup> a lower limit on the expected values. They considered a galaxy slightly less massive than those in our sample ( $M_{\text{DM}} = 10^{11.5} M_{\odot}$ ), as well as one comparable to those in this work ( $M_{\text{DM}} = 10^{12} M_{\odot}$ ).

For comparison, we consider the fraction of sightlines at a given  $D_{\text{tran}}$  for which  $\text{sum}(N_{\text{HI}}, 700 \text{ km s}^{-1})$  falls within the

<sup>27</sup> These values are only a lower-limit in the case that outflowing winds do not affect the gas distribution within the filamentary cold streams. van de Voort et al. (2011b) found that the wind prescription in simulations has little effect on the amount of gas that accretes onto halos but does affect the amount which is delivered into the ISM of the galaxy itself. Faucher-Giguère et al. (2011) argue that energetic winds can undergo hydrodynamical interactions with cold-streams removing some of the inflowing gas.



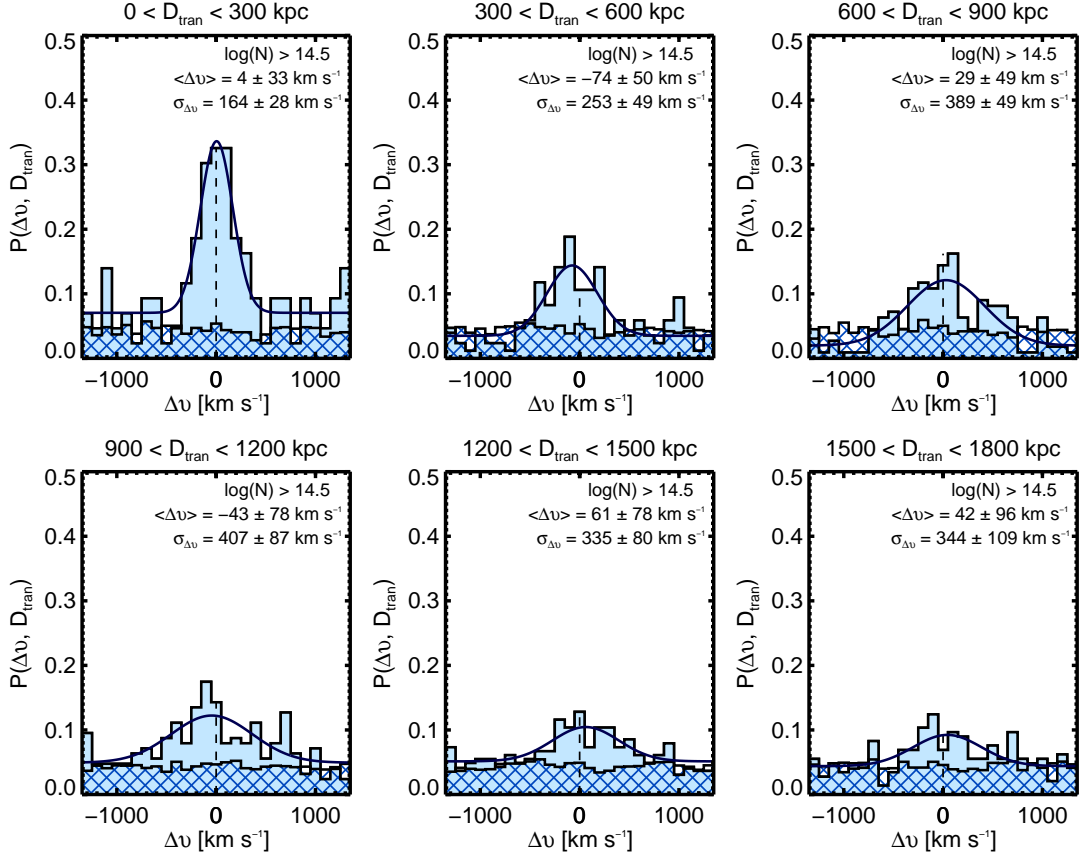


**Figure 18.** The velocity of absorbers with  $N_{\text{HI}} > 10^{14.5} \text{ cm}^{-2}$  in bins of  $D_{\text{tran}}$ , as indicated. Note that  $N_{\text{HI}} > 10^{14.5} \text{ cm}^{-2}$  absorbers are  $> 4$  times more likely to be found within  $\pm 300 \text{ km s}^{-1}$  and  $300 \text{ kpc}$  of a galaxy than at a random place in the IGM. See Table 3 for  $\eta_{\text{abs}}$  and the excess probability for all of the panels.

**Table 4**  
 $F_c$ : Comparison with Faucher-Giguère & Kereš (2011)

Sample	$\log(N_{\text{HI}}) [\text{cm}^{-2}]$	$F_c(<1 r_{\text{vir}})$	$F_c(<2 r_{\text{vir}})$
$M_{\text{DM}} = 10^{12} M_{\odot}$	17.2–20.3	11%	...
	$> 20.3$	4%	...
$M_{\text{DM}} = 10^{11.5} M_{\odot}$	17.2–20.3	12%	4%
	$> 20.3$	3%	1%
This work <sup>a</sup>	17.2–20.3	$30 \pm 14\%$	$24 \pm 9\%$
	$> 20.3$	$0_{-0}^{+10}\%$ <sup>b</sup>	$4 \pm 4\%$

<sup>a</sup> The  $F_c$  tabulated here from “this work” are the fraction of galaxies with a  $\text{sum}(N_{\text{HI}})$  statistic in the column density range. This is subtly different from the  $f_c$  presented earlier. Note that while we use a velocity cut of  $|\Delta v| < 700 \text{ km s}^{-1}$  here, the results would be the same if we used a  $\pm 300 \text{ km s}^{-1}$  window. Had we considered  $f_c$  as opposed to  $F_c$ , we would have calculated 20% for the LLS covering within both 1 and  $2 r_{\text{vir}}$ . The uncertainties quoted for “this work” are 1- $\sigma$  errors calculated assuming  $F_c$  follows a binomial distribution.

<sup>b</sup> We calculate the 1- $\sigma$  upper limit on this non-detection as  $1 - (1 - 0.68)^{1/(1+n)}$  where  $n = 10$  is the number of systems considered.

specified column density range. This is most akin to the results of Faucher-Giguère & Kereš (2011) as they measure the column density of absorbers after projecting their simulated cube onto a 2D plane. Note that here we use differential bins in  $N_{\text{HI}}$  ( $17.2 < \log(N_{\text{HI}}) < 20.3$ ), and since we are considering  $\text{sum}(N_{\text{HI}})$  rather than  $\text{max}(N_{\text{HI}})$ , we use  $F_c$  to denote the associated covering fraction (to differentiate it from the  $f_c$  measured earlier in this section).

Our measurements are compared with the Faucher-Giguère & Kereš (2011) simulation results in Table 4. Particularly in the case of LLS gas, we find  $\sim 3$  times higher  $F_c$  within  $r_{\text{vir}}$  and  $\sim 6$  times higher within  $2r_{\text{vir}}$  compared with the simulations. However, if the simulations results are treated as lower limits, then clearly they are consistent with the observations.

Fumagalli et al. (2011) also considered the covering fraction of H I surrounding 6 LBG-type galaxies at  $z = 2-3$  using cosmological zoom-in simulations with galactic winds included (though they are relatively weak with their particular implementation). They consider absorbers within  $r_{\text{vir}}$  and  $2r_{\text{vir}}$  for various thresholds in  $\log(N_{\text{HI}})$ :  $> 15.5$ ,  $> 17.2$ ,  $> 19.0$ , and  $> 20.3 \text{ cm}^{-2}$ . A comparison with the observations is given in Table 5. The models of Fumagalli et al. (2011) clearly under-predict the presence of  $15.5 < \log(N_{\text{HI}}) < 17.2$  gas surrounding galaxies. Similar to Faucher-Giguère & Kereš (2011), they also seem to under predict the radial extent of gas with  $N_{\text{HI}} \lesssim 10^{19} \text{ cm}^{-2}$ .

### 5.3. Evolution of the CGM from $z \sim 2.3$ to $z \lesssim 1$

There have been numerous studies of the low- $z$  galaxy-IGM connection. In the interest of brevity, below we compare our measured  $f_c$  with a small number of studies with comparable size and statistical power.

As discussed by Davé et al. (1999) and Schaye (2001), due to the expansion of the universe, the collapse of structure, and the evolution in the intensity of the metagalactic ionizing background, the  $N_{\text{HI}}$  associated with a fixed overdensity declines with redshift (e.g., an absorber at  $z = 0$  would have

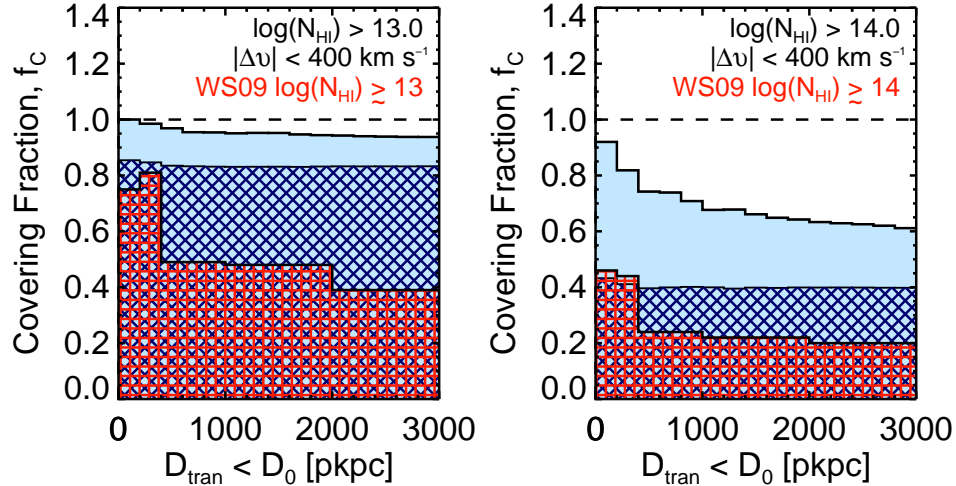


**Figure 19.** The covering fraction of high- and low-redshift absorbers in cumulative bins of  $D_{\text{tran}}$  (i.e., at each value of  $D_{\text{tran}}$ ,  $D_0$ , we consider all absorbers with smaller  $D_{\text{tran}}$ , as opposed to those absorbers with  $D_0 < D_{\text{tran}} < D_1$ .) In the (light-blue) solid histogram we plot our high- $z$  data for  $f_c$  close to galaxies. The (dark-blue) cross-hatched histogram shows the distribution at random places in the high- $z$  IGM. The (red) vertically-hatched histogram shows the distribution of  $f_c$  of low- $z$  absorbers taken from Wakker & Savage (2009). Here we consider the same cut in  $N_{\text{HI}}$  at both epochs ( $W_0 = 50\text{m}\text{\AA}$  is equivalent to  $N_{\text{HI}} = 10^{13}\text{ cm}^{-2}$  and similarly  $W_0 = 300\text{m}\text{\AA}$  is equivalent to  $N_{\text{HI}} = 10^{14}\text{ cm}^{-2}$ ).

**Table 5**  
Covering Fraction: Comparison with Fumagalli et al. (2011)

Sample	$\log(N_{\text{HI}})$ [ $\text{cm}^{-2}$ ]	$F_c (< 1 r_{\text{vir}})$	$F_c (< 2 r_{\text{vir}})$
Fumagalli et al.	$> 15.5$	38%	22%
	$> 17.2$	16%	7%
	$> 19.0$	6%	3%
	$> 20.3$	3%	1%
This work <sup>a</sup>	$> 15.5$	$90 \pm 9\%$	$68 \pm 9\%$
	$> 17.2$	$30 \pm 14\%$	$28 \pm 9\%$
	$> 19.0$	$10 \pm 9\%$	$8 \pm 5\%$
	$> 20.3$	$0^{+10}_{-0}\%$	$4 \pm 4\%$

<sup>a</sup> Values in “this work” are computed as described in Table 4. Were we to consider  $|\Delta v| < 300\text{ km s}^{-1}$  rather than  $|\Delta v| < 700\text{ km s}^{-1}$ , only the  $F_c$  for  $\log(N_{\text{HI}}) > 15.5$  within  $2 r_{\text{vir}}$  would change. The value for  $300\text{ km s}^{-1}$  would be  $60 \pm 10\%$ .

$N_{\text{HI}} \sim 20$  times lower than would be measured at the same overdensity at  $z \approx 2.3$ ). As a consequence, absorbers with the same  $N_{\text{HI}}$  at different redshifts trace different structures, and have very different incidence rates. For example, there are no regions of the Ly $\alpha$  forest at  $z \sim 2.3$  that have zero H I absorbers in a velocity window of  $\pm 700\text{ km s}^{-1}$  – every galaxy in our sample can be associated with (generally) a large number of absorbers. This is not the case at low- $z$ , where absorption-line spectra are sparsely populated and generally galaxies would be associated with very few (possibly no) H I absorbers. Similarly, the continued growth of structure and the rapid decline in the star-formation rate density toward  $z \sim 0$  means that a typical low- $z$  galaxy is expected to be in a very different place on its evolutionary sequence compared to a “typical” galaxy at  $z > 2$ . Large differences are also expected for gas fractions and baryonic accretion rates at low- $z$  compared to high. Thus, one might reasonably expect circumgalactic gas to differ as well.

With these caveats in mind, we compare the covering fraction,  $f_c$ , of the  $\langle z \rangle = 2.3$  sample with results at low- $z$ .

### 5.3.1. The CGM at $0.1 < z < 0.9$

Chen et al. (2001) considered 47 galaxies with  $\langle z \rangle = 0.36$  and  $D_{\text{tran}} < 330\text{ pkpc}$ <sup>28</sup>. Their galaxy sample covered a wide range of properties, with 68% having  $L_B > 0.25 L_B^*$ . The QSO spectra used were generally not of sufficient quality to allow for Voigt profile decompositions and thus the authors measured the equivalent width ( $W_0$ ) of Ly $\alpha$  absorption. Chen et al. (2001) considered absorbers to be associated with galaxies if  $|\Delta v| \lesssim 500\text{ km s}^{-1}$  (Morris & Jannuzi 2006).

For  $W_0 > 350\text{ m}\text{\AA}$  ( $N_{\text{HI}} \gtrsim 10^{14}\text{ cm}^{-2}$ ) and  $D_{\text{tran}} < 330\text{ pkpc}$ , 34/47 galaxies in their sample had detectable Ly $\alpha$  absorption, corresponding to  $f_c = 0.72$ . In the  $\langle z \rangle = 2.3$  sample there are 48 galaxies with  $D_{\text{tran}} < 330\text{ pkpc}$ . Using the same velocity window  $|\Delta v| < 500\text{ km s}^{-1}$ , we find 40/48 (83%) have Ly $\alpha$  absorption with  $N_{\text{HI}} \geq 10^{14}\text{ cm}^{-2}$ , consistent with the measurements from Chen et al. (2001). For clarity, the results from the low- $z$  studies as well as our measurements are reproduced in Table 6.

### 5.3.2. The CGM at $0.005 < z < 0.4$

Prochaska et al. (2011) studied the association of  $z < 0.2$  galaxies in 14 fields surrounding background QSOs. Similar to the Chen et al. (2001) study, they generally relied on conversions of published  $W_0$  measurements into  $N_{\text{HI}}$  using an assumed  $b_d$ . In total, their galaxy survey included 37 galaxies with  $D_{\text{tran}} < 300\text{ pkpc}$  and 1200 galaxies in all with  $\langle z \rangle = 0.18$ . They use a velocity window of  $|\Delta v| < 400\text{ km s}^{-1}$ . For the 26 galaxies with  $L > 0.1 L^*$  within 300 pkpc, 25 had accompanying Ly $\alpha$  absorption with  $N_{\text{HI}} > 10^{13}\text{ cm}^{-2}$ , or  $f_c = 96\%$ . In our sample, there are 43 galaxies with  $D_{\text{tran}} < 300\text{ pkpc}$ , all of which have a  $N_{\text{HI}} \geq 10^{13}\text{ cm}^{-2}$  absorber within  $|\Delta v| < 400\text{ km s}^{-1}$  ( $f_c = 100\%$ ).

These values appear consistent; however, the covering fraction of  $N_{\text{HI}} \geq 10^{13}\text{ cm}^{-2}$  gas is a very poor measure of the extent of the CGM at high redshift. For example, if we consider

<sup>28</sup> The  $D_{\text{tran}}$  ranges quoted here have been adjusted from the cosmology considered in Chen et al. (2001) to the cosmology used in this paper at the mean redshift of the sample,  $\langle z \rangle = 0.36$ .

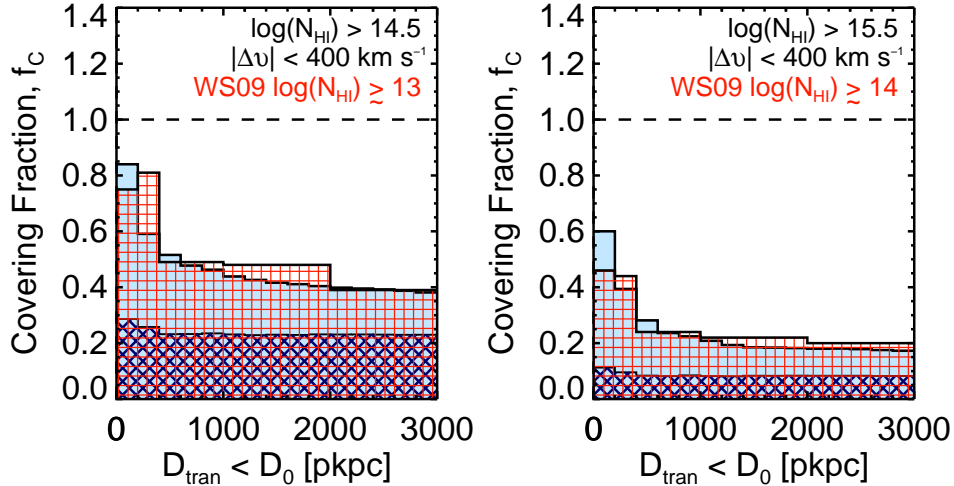


**Figure 20.** Same as Figure 19, but here we consider different  $N_{\text{HI}}$  cuts for the high- $z$  sample. We have found the  $N_{\text{HI}}$  lower limit for the high- $z$  sample which best reproduces the trend of the low- $z$   $f_c$  as a function of  $D_{\text{tran}}$ . We can see that the trends of high- $z$  absorbers of 1.5 dex higher  $N_{\text{HI}}$  are well matched to the distributions of low- $z$  absorbers.

the same velocity window ( $|\Delta v| < 400 \text{ km s}^{-1}$ ) and the same  $N_{\text{HI}}$  threshold ( $N_{\text{HI}} > 10^{13} \text{ cm}^{-2}$ ), we find  $f_c = 95\%$  within 1 pMpc and  $f_c = 94\%$  within 2 pMpc; i.e., there is no appreciable change in the  $f_c$  of gas of this  $N_{\text{HI}}$  with increasing distance. Prochaska et al. (2011) find  $f_c = 70\%$  for  $D_{\text{tran}} < 1$  pMpc in their sample.

Measurements with a higher  $N_{\text{HI}}$  threshold have larger dynamic range; for  $N_{\text{HI}} > 10^{14} \text{ cm}^{-2}$ , Prochaska et al. (2011) measure  $f_c = 70\%$  for  $D_{\text{tran}} < 300$  pkpc, and  $f_c = 38\%$  for 1 pMpc. For our  $\langle z \rangle \sim 2.3$  sample, we measure  $f_c = 81\%$  for  $D_{\text{tran}} < 300$  pkpc and  $f_c = 70\%$  for  $D_{\text{tran}} < 1$  pMpc.

### 5.3.3. The CGM in the Local Universe: $cz < 6000 \text{ km s}^{-1}$

Wakker & Savage (2009) (hereafter, WS09) studied the gaseous distribution around local galaxies ( $cz < 6000 \text{ km s}^{-1}$ ) along 76 lines of sight. The galaxy catalog considered included  $\sim 20,000$  local galaxies. The absorber catalog included 115 intergalactic Ly $\alpha$  absorbers (i.e., not from the Galaxy) over the same redshift range. They calculate  $f_c$  in cumulative distance bins (e.g.  $D_{\text{tran}} < 200$  pkpc).

For comparison to the WS09 sample, we use a velocity window  $|\Delta v| < 400 \text{ km s}^{-1}$  with respect to galaxy redshifts in our high redshift sample. From WS09 (Table 10) we use the values of  $f_c$  measured for the galaxy sample with  $L > 0.25 L^*$ .<sup>29</sup> They consider two classes of absorbers, those with  $W_0 > 50 \text{ m}\text{\AA}$  ( $N_{\text{HI}} > 10^{13} \text{ cm}^{-2}$ ) and  $W_0 > 300 \text{ m}\text{\AA}$  ( $N_{\text{HI}} \gtrsim 10^{14} \text{ cm}^{-2}$ ). We make a direct comparison to our sample with the same  $N_{\text{HI}}$  threshold in Figure 19 and Table 6. Our measurements are shown in the solid histogram, the random high- $z$  sample is plotted in the (dark-blue) cross-hatched histogram, and the WS09 sample is represented by the (red) vertically-hatched histogram. One can clearly see that at all  $D_{\text{tran}}$  and for both thresholds in  $N_{\text{HI}}$ , the  $z \sim 0$  sample shows significantly less covering than the high- $z$  sample.

As mentioned above, absorbers of fixed  $N_{\text{HI}}$  are theoretically expected to trace higher-overdensity gas at low redshift than at high redshift. By considering various  $N_{\text{HI}}$  thresh-

olds in our own data, we found that  $f_c$  of the low- $z$   $W_0 > 50 \text{ m}\text{\AA}$  ( $N_{\text{HI}} > 10^{13} \text{ cm}^{-2}$ ) sample was most comparable to high- $z$  absorbers with  $N_{\text{HI}} > 10^{14.5} \text{ cm}^{-2}$ ; similarly, the WS09  $W_0 > 300 \text{ m}\text{\AA}$  ( $N_{\text{HI}} \gtrsim 10^{14} \text{ cm}^{-2}$ ) can be matched to our high- $z$  absorbers with  $N_{\text{HI}} > 10^{15.5} \text{ cm}^{-2}$ . Note that we chose the  $N_{\text{HI}}$  threshold which best reproduced  $f_c$  measured on  $\sim \text{Mpc}$  scales.

These two comparisons, shown in Figure 20, exhibit remarkably similar patterns in the covering fraction of  $N_{\text{HI}}$  as a function of  $D_{\text{tran}}$ . It therefore appears that low- $z$  absorbers with  $\log(N_{\text{HI}}) = N_0$  on average trace the same physical regions around galaxies as gas with  $\log(N_{\text{HI}}) = N_0 + 1.5$  at  $\langle z \rangle = 2.3$ . While we do not directly measure universal overdensity, these results lend observational support to the predictions by Davé et al. (1999) and Schaye (2001) that gas at the same universal overdensity at low- and high- $z$  would have lower  $N_{\text{HI}}$  at low- $z$ . These measurements also suggest that the physical size of the CGM around a typical galaxy is 300 pkpc at both  $z \sim 0$  and  $\langle z \rangle = 2.3$ .

## 6. MAPPING THE CIRCUMGALACTIC MEDIUM

Another way to visualize the distribution of neutral hydrogen surrounding star-forming galaxies is to “map” the distribution along the transverse direction and the line of sight at the same time. As in §4.3, we use  $|\Delta v|$  to compute a line-of-sight distance assuming it is entirely due to the Hubble flow. In Figures 21 - 24, the vertical axes represent the  $D_{\text{Hubble}}$  velocity scale line-of-sight distribution of gas. The horizontal axes correspond to the physical impact parameter between the galaxy and the QSO line of sight,  $D_{\text{tran}}$ . Colors encode the incidence,  $\eta_{\text{abs}}$ , of the gas in a given pixel in the map and the black and white shading represents the signal-to-noise ratio (S/N) with which  $\eta_{\text{abs}}$  is detected.

The S/N is determined using Poisson statistics. For a given bin in  $D_{\text{tran}}$  and  $D_{\text{Hubble}}$ , we count the total number of absorption lines found in the random distribution,  $n_{\text{abs,ran}}$ , and the number of random locations considered at that impact parameter,  $n_{\text{gal,ran}}$ . We also count the number of real galaxies at that impact parameter,  $n_{\text{gal}}$ . The “noise” level of the map is then

<sup>29</sup> Our spectroscopic sample includes galaxies to  $\mathcal{R} = 25.5$ . This is equivalent to  $L > 0.25 L^*$  at  $z \approx 2.3$ .

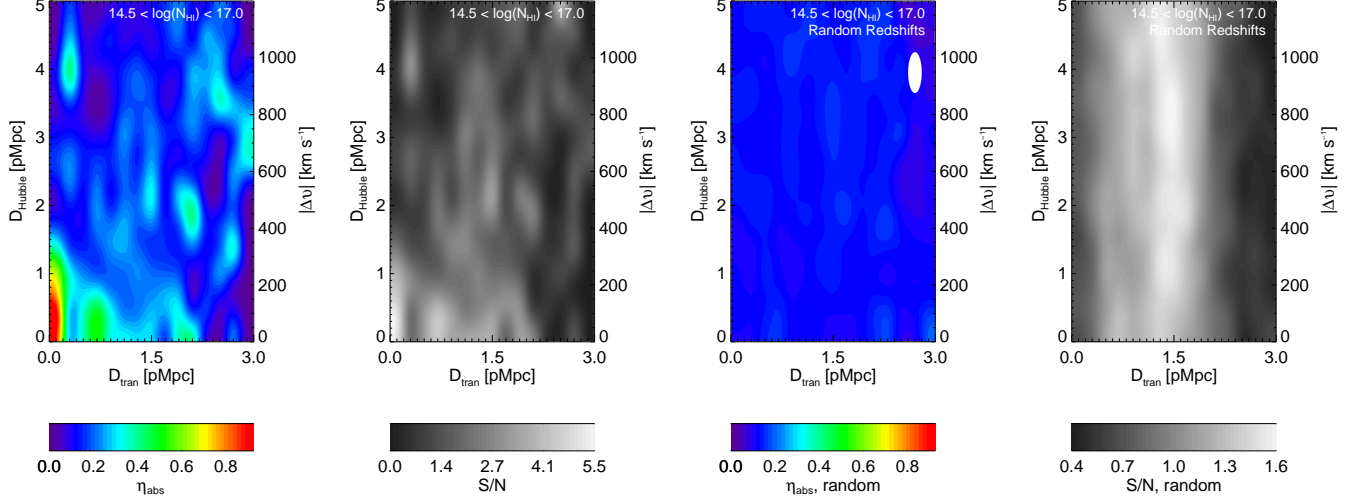


**Figure 21.** The incidence of  $14.5 < \log(N_{\text{HI}}) < 17$  absorbers. *Far Left:* Map of the  $\eta_{\text{abs}}$  with respect to the positions of galaxies (at the origin). *Second from Right:* The distribution at random locations in the IGM. The greyscale panels show the S/N ratios of the maps calculated as discussed in §6. The “bin” size for this map is  $200 \times 200$  pkpc and the smoothing scale is  $200$  kpc in  $D_{\text{tran}}$  and  $140 \text{ km s}^{-1}$  ( $600$  pkpc) along the line of sight. The FWHM of the gaussian smoothing beam is represented by the ellipse in the top right-hand corner of the 3rd panel from the left. Note that there is a strong peak in the incidence of high column density absorbers at close galacto-centric distances. The color bars in the  $\eta_{\text{abs}}$  maps have been re-normalized by  $\chi_v = 6.3$  in order to match the values of  $\eta_{\text{abs}}$  summed over  $|\Delta v| < 300 \text{ km s}^{-1}$ . The vertical structure in the S/N maps is caused by the variation in the number of galaxies in each bin of  $D_{\text{tran}}$ .

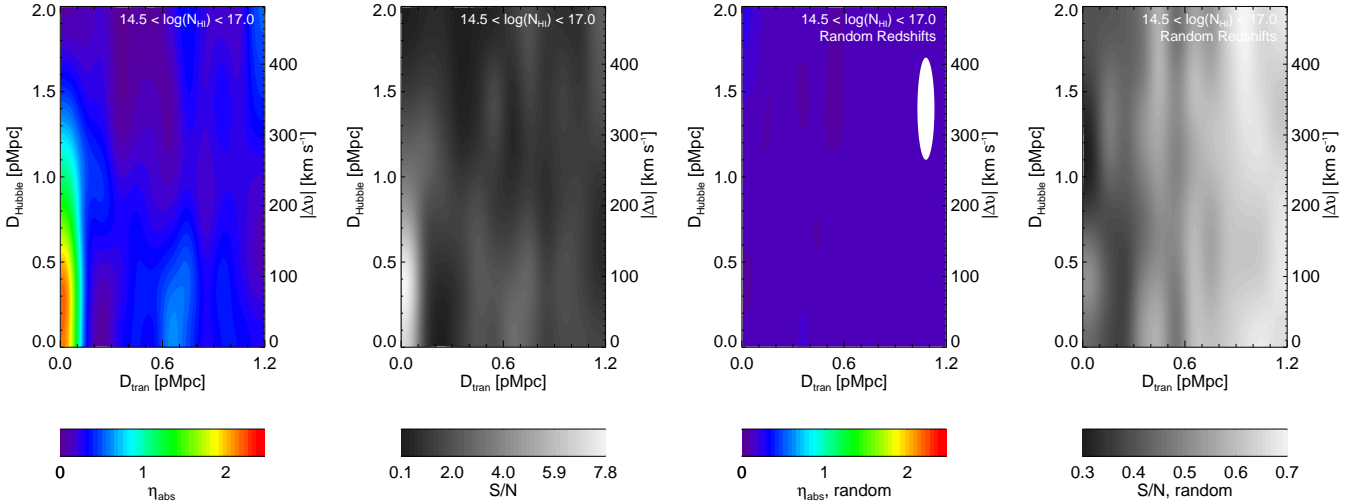


**Figure 22.** Same as Figure 21 but zoomed in to show the small scale distribution. The “bin” size for this map is  $100 \times 100$  pkpc. The smoothing scale is  $100$  kpc in impact parameter and  $140 \text{ km s}^{-1}$  ( $600$  pkpc) along the line of sight. The color bars for the incidence maps have been re-normalized  $\chi_v = 12.6$  in order to match the  $\eta_{\text{abs}}$  summed over  $|\Delta v| < 300 \text{ km s}^{-1}$ .

taken to be:

$$\sigma_{\text{sig}} = \frac{\sqrt{n_{\text{gal}} (n_{\text{abs,ran}}/n_{\text{gal,ran}})}}{n_{\text{gal}}}, \quad (12)$$

where the quantity inside the square root is the number of absorption systems expected (based on the incidence for the random sample) given the number of galaxies in the real sample at a given  $D_{\text{tran}}$ . The square root of this quantity represents the Poisson uncertainty in the number of absorbers that would be detected; the division by  $n_{\text{gal}}$  results in an expression for the error in  $\eta_{\text{abs}}$  per galaxy. This value is akin to the shaded error bars surrounding the median value of the random sample in

Figure 9. The signal-to-noise ratio is then taken to be:

$$\text{S/N} = \frac{\eta_{\text{abs}}}{\sigma_{\text{sig}}} \quad (13)$$

The maps are generated using three different bin sizes. We consider the intermediate bin size ( $200 \times 200$  pkpc) for two cuts in  $N_{\text{HI}}$  (Figures 21 and 23) which cover impact parameters out to  $3$  pMpc. For high- $N_{\text{HI}}$  absorbers which exhibit a peak at small scales, we also consider maps with  $100 \times 100$  pkpc bins (Figure 22). For low- $N_{\text{HI}}$  absorbers, we provide a map with  $400 \times 400$  pkpc bins to emphasize the large scale distribution (Figure 24). After the number of absorbers per bin is measured, the values are placed onto a  $10$  times finer grid and smoothed by a gaussian kernel with a full width half

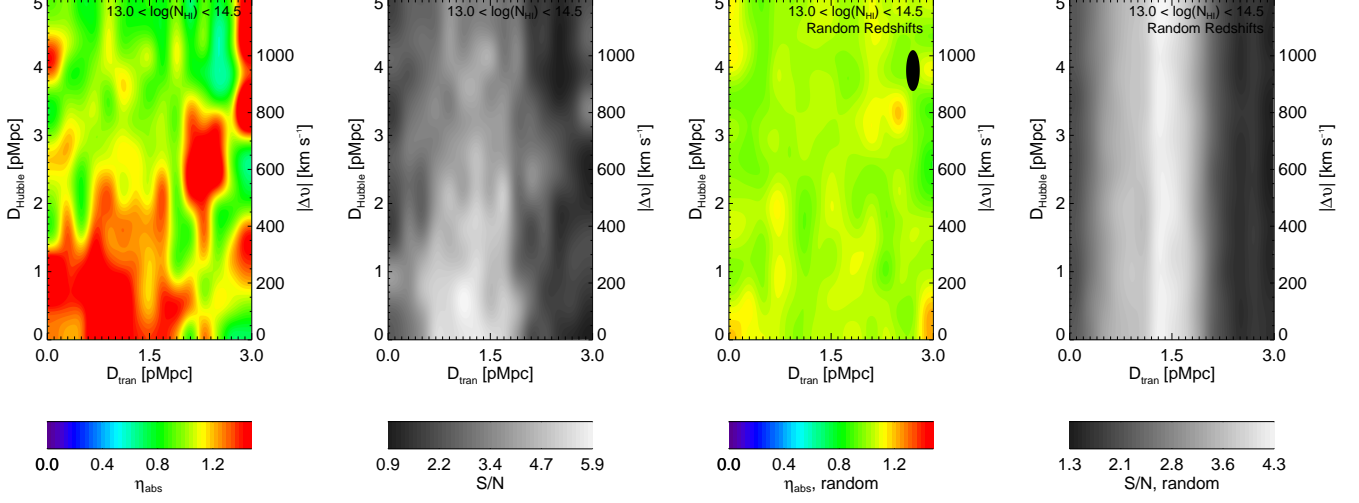


**Figure 23.** Same as Figure 21 but for low column density absorbers with  $13 < \log(N_{\text{HI}}) < 14.5$ . Note, that the incidence of these absorption systems is higher in the large-scale regions surrounding galaxies, similar to that of high column density systems. However, unlike the high column density absorbers, there is no strong peak in the incidence rate of low- $N_{\text{HI}}$  systems at small galacto-centric distances. The color bars for the incidence maps have been re-normalized  $\chi_v = 6.3$  in order to match the  $\eta_{\text{abs}}$  summed over  $|\Delta v| < 300 \text{ km s}^{-1}$ .

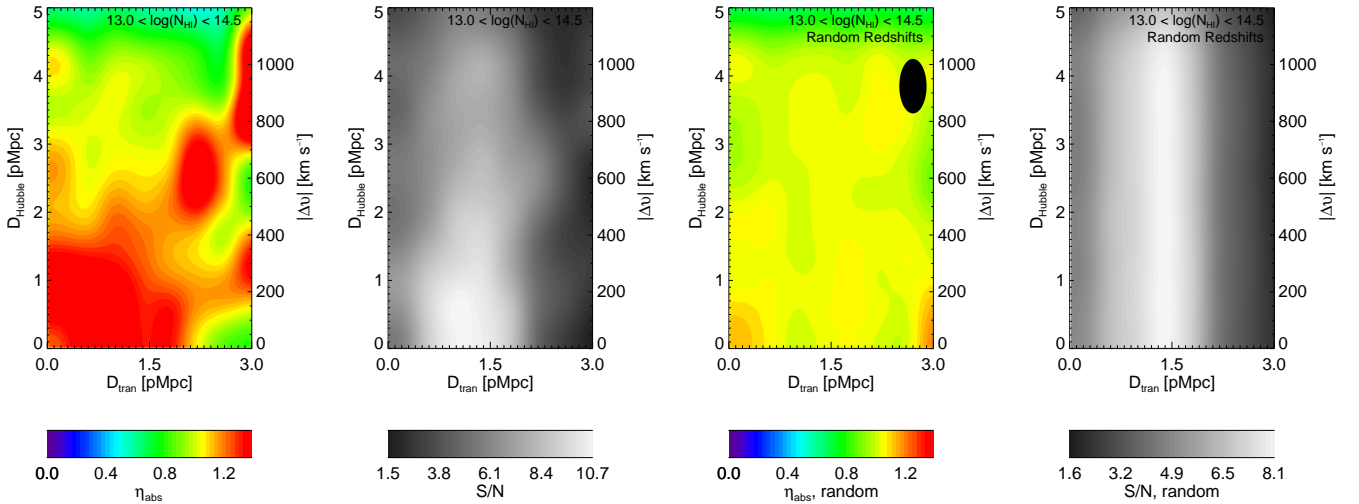


**Figure 24.** Same as Figure 23 but with  $400 \times 400 \text{ pkpc}$  binning. Note that the line-of-sight distribution is compressed compared to the transverse distribution. The color bars for the incidence maps have been re-normalized  $\chi_v = 3.15$  in order to match the  $\eta_{\text{abs}}$  summed over  $|\Delta v| < 300 \text{ km s}^{-1}$ .

maximum equal to the bin size in impact parameter ( $x$ -axis) and a velocity scale of  $140 \text{ km s}^{-1}$  or  $600 \text{ pkpc}$  in Hubble distance ( $y$ -axis). Binning and smoothing is required to make maps of this type as the values of impact parameter and velocity are discrete. The scale of the smoothing, however, is motivated by the data. The smoothing in  $D_{\text{tran}}$  is selected to obtain a large enough sampling of the inner and outer bins such that the noise in the random distribution is reduced. The velocity scale smoothing corresponds roughly to the amplitude of the redshift uncertainties (see §2.2).

In Figures 21 – 24, the normalization of the color bar is rescaled from the raw  $\eta_{\text{abs}}$  per  $100 \times 100$ ,  $200 \times 200$ , or  $400 \times 400 \text{ pkpc}$  bin by the multiplicative factor  $\chi_v$ , where:

$$\chi_v = \frac{D_{\text{Hubble}}(300 \text{ km s}^{-1})}{D_{\text{Hubble}}(\text{bin})} \approx \frac{1.26 \text{ pMpc}}{D_{\text{Hubble}}(\text{bin})} \quad (14)$$

where  $D_{\text{Hubble}}(\text{bin})$  is either 100, 200, or 400 pkpc. For the 100 pkpc bins,  $\chi_v = 12.6$ . This renormalization brings the scale of  $\eta_{\text{abs}}$  into agreement with that shown in Figures 16 and 17.

Recently, Rakic et al. (2011b) constructed similar maps to those presented here using pixel optical depth analysis (instead of Voigt profile fits) for a subset of the data presented here. Many of the conclusions discussed in the following section are corroborated by the independent analysis of Rakic et al. (2011b, §4).

#### 6.1. Absorbers with $N_{\text{HI}} > 10^{14.5} \text{ cm}^{-2}$

Shown in Figure 21 is a map of  $\eta_{\text{abs}}$  for  $10^{14.5} < N_{\text{HI}} < 10^{17} \text{ cm}^{-2}$ . Here we compare a map of the absorber distribution around galaxies (left-most panel) to a map which represents the general IGM as measured using the random distribution (third panel from left). Clearly, the incidence of  $N_{\text{HI}} > 10^{14.5} \text{ cm}^{-2}$  absorbers is higher near galaxies than in the general

**Table 6**  
H I Covering Fraction: Comparison with Low- $z$  Studies<sup>a</sup>

Sample	$W_0(Ly\alpha)$ mÅ	$\log(N_{\text{HI}})$ [cm <sup>-2</sup> ]	$D_{\text{tran}}$ pkpc	$ \Delta v $ km s <sup>-1</sup>	$f_c$
Chen et al. $0.1 < z < 0.9$	350	$\gtrsim 14$	<330	500	72%
This work $z \sim 2.3$	...	>14	<330	500	$83 \pm 5\%$
Prochaska et al. $0.005 < z < 0.4$	50	$\gtrsim 13$	<300	400	96%
	300	$\gtrsim 14$	<300	400	70%
	50	$\gtrsim 13$	<1000	400	70%
	300	$\gtrsim 14$	<1000	400	38%
This work $z \sim 2.3$	...	>13	<300	400	$100^{+0}_{-3}\%$ <sup>b</sup>
	...	>14	<300	400	$81 \pm 6\%$
	...	>13	<1000	400	$95 \pm 1\%$
	...	>14	<1000	400	$70 \pm 3\%$
Wakker & Savage $z < 0.017$	50	$\gtrsim 13$	<200	400	75%
	50	$\gtrsim 13$	<400	400	81%
	50	$\gtrsim 13$	<1000	400	49%
	50	$\gtrsim 13$	<2000	400	48%
	50	$\gtrsim 13$	<3000	400	39%
	300	$\gtrsim 14$	<200	400	46%
	300	$\gtrsim 14$	<400	400	44%
	300	$\gtrsim 14$	<1000	400	24%
	300	$\gtrsim 14$	<2000	400	22%
	300	$\gtrsim 14$	<3000	400	20%
This work $z \sim 2.3$	...	> 13	< 200	400	$100^{+0}_{-4}\%$ <sup>c</sup>
	...	> 13	< 400	400	$98 \pm 2\%$
	...	> 13	< 1000	400	$95 \pm 1\%$
	...	> 13	< 2000	400	$94 \pm 1\%$
	...	> 13	< 3000	400	$94 \pm 1\%$
	...	> 14	< 200	400	$92 \pm 5\%$
	...	> 14	< 400	400	$82 \pm 5\%$
	...	> 14	< 1000	400	$71 \pm 3\%$
	...	> 14	< 2000	400	$64 \pm 2\%$
	...	> 14	< 3000	400	$61 \pm 2\%$

<sup>a</sup> The distance binning is cumulative, so  $f_c$  is the covering fraction of gas with  $D_{\text{tran}} <$  the distance listed in the table and  $|\Delta v| <$  the velocity listed in the table. The low- $z$  samples generally do not include Voigt profile fits, but rather measure equivalent widths,  $W_0$ . The approximate value of  $N_{\text{HI}}$  associated with each  $W_0$  limit is listed. The uncertainties quoted for "this work" are 1- $\sigma$  errors calculated assuming  $f_c$  follows a binomial distribution.

<sup>b</sup> We calculate the 1- $\sigma$  lower limit on this 100% detection as  $(1-0.68)^{1/(1+n)}$  where  $n=43$  is the number of systems considered.

<sup>c</sup> We calculate the 1- $\sigma$  lower limit on this 100% detection as  $(1-0.68)^{1/(1+n)}$  where  $n=25$  is the number of systems considered.

IGM.  $\eta_{\text{abs}}$  remains significantly and consistently higher than that seen in the random map within 300 km s<sup>-1</sup> along the line of sight and out to 2 pMpc in impact parameter.

The maps presented in Figure 22 which show the inner distance and velocity ranges at higher resolution, allow one to compare the scales of the absorption excess in Hubble distance and in  $D_{\text{tran}}$  in order to detect redshift anisotropies indicative of particular kinematic patterns. Galaxy redshift errors and peculiar velocities of gas with respect to galaxies

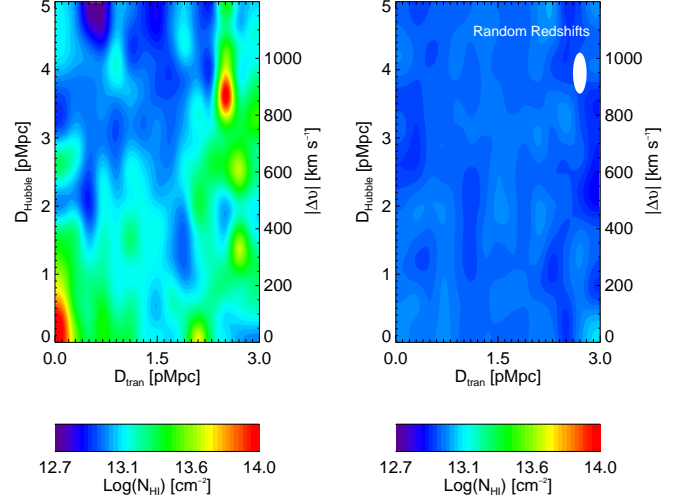


**Figure 25.** Maps of the median  $N_{\text{HI}}$  with respect to the positions of galaxies. The “bin” size for this map is 200 x 200 kpc. The smoothing scale is 200 kpc in impact parameter and 140 km s<sup>-1</sup> (600 pkpc) along the line of sight. *Left:* The map of the true distribution of column densities. *Right:* The map of the column density distribution in the random sample. The significance with which we detect structures appearing in this map is quantified with the S/N maps presented in the preceding figures.

will generally expand the line-of-sight velocity distribution.<sup>30</sup> Therefore, if the signal along the line of sight is elongated more than expected given the redshift errors and the scale of the transverse distribution, the remaining velocity structure may be attributed to peculiar velocities of the gas with respect to galaxies.

Based on Figure 22, adopting the green contours as representative of the most extreme portion of the overdensity of gas (conservatively) corresponds to a velocity scale of  $\sim 300$  km s<sup>-1</sup> and a physical impact parameter  $\sim 125$  pkpc<sup>31</sup>. Subtracting in quadrature the 140 km s<sup>-1</sup> smoothing (which corresponds roughly to our redshift errors) leaves a residual velocity scale of  $|\Delta v| \simeq 265$  km s<sup>-1</sup>. This velocity, were it due to pure Hubble flow, would indicate a distance of  $\sim 1.1$  pMpc. In order to consider the portion of the line-of-sight elongation likely due to peculiar velocities, we can subtract in quadrature the extent of the transverse distribution – in effect subtracting a possible Hubble flow broadening. Subtracting the  $D_{\text{Hubble}} = 125$  pkpc or  $\sim 35$  km s<sup>-1</sup> leaves  $\simeq 260$  km s<sup>-1</sup>; in other words, peculiar velocities of  $\pm 260$  km s<sup>-1</sup> are indicated by the data.<sup>32</sup>

## 6.2. Absorbers with $N_{\text{HI}} < 10^{14.5}$ cm<sup>-2</sup>

Figure 23 displays a map of the incidence of lower-column density absorbers ( $10^{13.0} < N_{\text{HI}} < 10^{14.5}$  cm<sup>-2</sup>). Again comparing the left-most panel (galaxy positions) to the third panel from the left (random IGM), one sees that the incidence of these absorbers is higher in the regions near galaxies than

<sup>30</sup> One exception to this “rule” is the case of inflowing gas on large scales where the inflow velocities counter the relative Hubble flow causing a reduction in the line-of-sight velocity distribution.

<sup>31</sup> Maps produced using a symmetric smoothing kernel of 200 pkpc in both the line-of-sight and transverse distance (not shown) also yield excess absorption to 300 km s<sup>-1</sup> along the line of sight. The extent of the line-of-sight distribution is robust to reductions in the line-of-sight smoothing kernel; however, the S/N associated with the excess is improved by the adopted smoothing kernel.

<sup>32</sup> Or, we have seriously underestimated the magnitude of our galaxy redshift errors.

in the general IGM; however, the low- $N_{\text{HI}}$  map exhibits no strong peak at small galactocentric distances.

Since there is little structure on small scales in Figure 23, the map has been more heavily smoothed to emphasize larger scales. Drawing attention to the edge of the red contours in Figure 24, it appears that the scale of the excess absorption is marginally *smaller* along the  $D_{\text{Hubble}}$  (line-of-sight) axis (1.5 pMpc) than along the transverse distance (2 pMpc). This suggests there may be coherent infall motion on  $\gtrsim$  Mpc scales compressing the distribution along the line of sight, the Kaiser (1987) effect. Rakic et al. (2011b) analyze the pixel statistics in the KBSS survey and discuss the kinematics of the circumgalactic gas in detail. They find a significant detection of compression of the signal along the line of sight which they interpret as large-scale infall.

### 6.3. Median Column Density Maps

An alternative visualization of the distribution of H I surrounding galaxies, avoiding the division of absorbers into low and high column density, is a map of the median  $N_{\text{HI}}$  in a given bin. Figure 25 shows maps where the color bar represents the median  $N_{\text{HI}}$  in a given bin of  $D_{\text{tran}}$  and  $D_{\text{Hubble}}$ . On small scales, the behavior is similar to the high- $N_{\text{HI}}$  absorbers, with significant elongation in the line of sight direction, due to a combination of peculiar motions of the gas and error in  $z_{\text{gal}}$ .

In this section we have shown that the kinematics of absorbers with  $\log(N_{\text{HI}}) > 14.5$  are consistent with a peculiar velocity component of  $\sim \pm 260 \text{ km s}^{-1}$  within  $\sim 100 \text{ pkpc}$  of galaxies, and separately that absorbers with  $\log(N_{\text{HI}}) < 14.5$  may exhibit the kinematic signature of retarded Hubble flow on scales  $\gtrsim 1 \text{ pMpc}$ .

### 6.4. Explaining the Gas-Phase Kinematics

The kinematics of the gas surrounding galaxies may provide important clues about the physical processes occurring near galaxies. The two most plausible scenarios for the origin of the observed gas is that it traces the large scale structure (in which case it is likely falling onto the halo) or that it is the result of galactic winds, known to operate in these galaxies. Most likely, it is some combination of the two phenomena. Unfortunately, the sign of the velocity offset (red-shifted or blue-shifted) cannot tell us what the relative motion of the gas is with respect to the galaxy since its position along the line of sight is not known. For example, gas which is redshifted with respect to the galaxy might be behind the galaxy, and thus be either outflowing or moving with the Hubble flow at larger distance. Conversely, redshifted absorbers could be foreground gas that is redshifted because it is falling onto the galaxy. There is no way to know *a priori* which scenario holds in which cases.

We recall that in §4.1 it was shown that the full extent in  $\Delta v$  spanned by absorbers comprising the net excess over random is  $|\Delta v| \lesssim 700 \text{ km s}^{-1}$ , with the most significant portion of the excess within  $|\Delta v| \lesssim 300 \text{ km s}^{-1}$ . Our map of high- $N_{\text{HI}}$  systems confirms the  $300 \text{ km s}^{-1}$  excess and allows us to measure the extent of the peculiar velocities. After accounting for our estimated galaxy redshift errors (§ 6.1), the range of significant excess becomes  $|\Delta v| \lesssim 260 \text{ km s}^{-1}$ .

In-falling cool gas is likely to be moving at relative velocities smaller than the galaxy circular velocity

(Faucher-Giguère & Kereš 2011):

$$v_{\text{circ}} = \sqrt{\frac{GM_{\text{DM}}}{r_{\text{vir}}}} = 220 \text{ km s}^{-1}, \quad (15)$$

where we assume  $M_{\text{DM}} = 10^{12} M_{\odot}$  and  $r_{\text{vir}} = 91 \text{ pkpc}$  (see §2.1 and §8.3). Since we measure only the line-of-sight component of this velocity,  $|v_{\text{los}}| \sim 200 \text{ km s}^{-1}$  might serve as an approximate upper limit on the line-of-sight velocity component due to gravitationally induced peculiar velocities. Unless we have significantly underestimated the measurement uncertainties in  $z_{\text{gal}}$ , accreting gas would be expected to have a “quieter” velocity field than observed.

On the other hand, outflows observed in the galaxy spectra regularly show blue-shifted velocities as high as  $800 \text{ km s}^{-1}$ , and large velocity widths appear to be required to explain the strength of strongly saturated absorption at modest impact parameters ( $D_{\text{tran}} \lesssim 100 \text{ pkpc}$ ), based on the galaxy-galaxy pairs analysis of Steidel et al. (2010). In the context of their simple model, the envelope of  $|\Delta v|$  is simply the component of the outflow speed  $v_{\text{out}}$  projected along an observers line of sight; this maximum velocity also dictates how strong the resulting absorption features will be, with  $W_0$  increasing proportionally to  $v_{\text{out}}$ . To model the behavior of  $W_0$  with impact parameter,  $v_{\text{out}}$  was the principle normalization factor and the inferred values were  $650 \lesssim v_{\text{out}} \lesssim 820 \text{ km s}^{-1}$  depending on the ion. In the present work, the first bin in  $D_{\text{tran}}$  extends from 50-100 pkpc, with a median  $D_{\text{tran}} = 80 \text{ pkpc}$ , with median  $\log(N_{\text{HI}}) \simeq 16.5$ . Assuming the Steidel et al. (2010) geometric/kinematic model (with  $R_{\text{eff}} = 90 \text{ pkpc}$ ) would predict that a line of sight with  $D_{\text{tran}} = 80 \text{ kpc}$  would have  $|\Delta v| \lesssim 0.46 v_{\text{out}}$  (equivalent to an observable velocity range between  $\pm 325$  and  $\pm 400 \text{ km s}^{-1}$ ) and a threshold  $N_{\text{HI}} \sim 10^{17} \text{ cm}^{-2}$  [analogous to our  $\max(N_{\text{HI}})$  statistic], both compatible with the observations from the QSO sightlines discussed above.

## 7. THE DOPPLER WIDTH

In addition to  $N_{\text{HI}}$  and  $z_{\text{abs}}$ , the third component of a Voigt profile fit is the Doppler width,  $b_d$ . In the case of an unsaturated line, the Voigt profile is well approximated by a Gaussian in optical depth, with a Doppler parameter:

$$b_d = \sqrt{2}\sigma = \frac{\text{FWHM}}{2\sqrt{\ln 2}}. \quad (16)$$

In the case of purely thermal broadening, the gas temperature  $T$  can be inferred directly from the Doppler parameter:

$$b_d(T) = \sqrt{\frac{2kT}{m}} \quad (17)$$

where  $m$  is the mass of the ion and  $k$  is the Boltzmann constant. For H I,

$$T = \frac{m_{\text{H}}}{2k} b_d^2 = 4 \times 10^4 \text{ K} \left( \frac{b_d}{26 \text{ km s}^{-1}} \right)^2; \quad (18)$$

noting that  $26 \text{ km s}^{-1}$  is the median value of  $b_d$  in the full absorber catalog.

The physical state of the IGM is predicted to be governed by the balance of two principle processes: the adiabatic cooling caused by the expansion of the Universe and photoionization heating, generally from the UV background. In the regime where this holds and in the case that the baryonic overdensity roughly traces the dark matter overdensity,

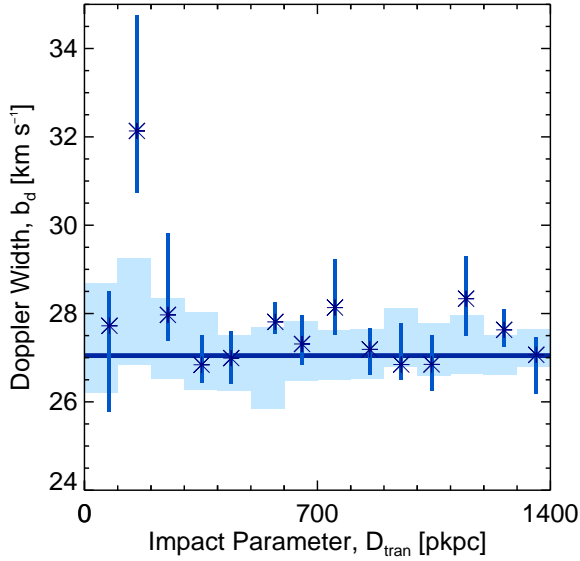


**Figure 26.** The Doppler width,  $b_d$ , of absorbers with  $\log(N_{\text{HI}}) > 13$  and  $|\Delta v| < 700 \text{ km s}^{-1}$  as a function of transverse distance from a galaxy. The symbols have the same meaning as those in Figure 9 except they refer to  $b_d$  instead of  $N_{\text{HI}}$ . Note the peak in the second bin corresponding to absorbers with  $100 < D_{\text{tran}} < 200 \text{ pkpc}$ .

a natural consequence is a relationship between the temperature of the gas,  $T$ , and its density,  $\rho$ . Higher-density regions, having more gravitational resistance to the Hubble flow, cool less and thus have higher temperatures on average (see e.g., Hui & Gnedin 1997; Schaye et al. 1999). And indeed, observed distributions of thermally broadened absorption lines exhibit higher  $b_d$  for absorbers with higher  $N_{\text{HI}}$  (Pettini et al. 1990; Schaye et al. 2000; Bryan & Machacek 2000; Ricotti et al. 2000; McDonald et al. 2001).

Other processes can also broaden individual absorption components. For the most diffuse and physically extended absorbers, generally with lower  $N_{\text{HI}}$ , the Hubble flow itself can contribute significantly to the line width. Turbulence (here meaning bulk motions of the gas) can also broaden absorption features such that:

$$b_d^2 = b_{\text{turb}}^2 + \frac{2kT}{m} \quad (19)$$

where  $b_{\text{turb}}$  is the turbulent component of the line width.

In this section we discuss the distribution of Doppler widths ( $b_d$ ) observed in absorption systems as a function of their galactocentric distance. The observed trends are much more subtle than those in  $N_{\text{HI}}$ , but their utility in discerning the physical state of the gas motivates a careful analysis.

### 7.1. The Dependence of $b_d$ on Proximity to Galaxies, $D_{\text{tran}}$

Figure 26 shows the Doppler width ( $b_d$ ) of absorbers with  $N_{\text{HI}} > 10^{13} \text{ cm}^{-2}$  versus  $D_{\text{tran}}$ . While considerably more noisy than the column density trends in the previous section, it appears that within the second bin (corresponding to  $100 < D_{\text{tran}} < 200 \text{ pkpc}$ ) the median value of  $b_d$  is considerably higher than that of the random sample.

We consider the trend in  $b_d$  versus  $N_{\text{HI}}$  for both the sample of absorbers close to galaxies and that of the full absorber catalog. In this way, we can examine the  $b_d$  of absorbers at fixed  $N_{\text{HI}}$ , as shown in Figure 27, in order to evaluate the effect of the  $T - \rho$  relationship on this result. Here, each of the four

closest bins in  $D_{\text{tran}}$  (Figure 26) is broken into individual panels. The asterisks represent the absorbers close to galaxies. The black horizontal lines and shading refer to the *full absorber catalog*.<sup>33</sup> Considering first the top right-hand panel with  $100 < D_{\text{tran}} < 200 \text{ pkpc}$  (the bin with the majority of the signal in Figure 26) for  $N_{\text{HI}} > 10^{14} \text{ cm}^{-2}$ , the median  $b_d$  of absorbers close to galaxies is larger than the median of the full absorber sample at fixed  $N_{\text{HI}}$ . This suggests that the larger  $b_d$  cannot be attributed solely to a dependence on  $N_{\text{HI}}$  as in the  $T - \rho$  relation.

Figure 27 shows that the median  $b_d$  for the sample of absorbers within  $D_{\text{tran}} \sim 100 - 300 \text{ pkpc}$  of galaxies is systematically larger than that of absorbers from the full absorber catalogue across most bins in  $N_{\text{HI}}$ . However, the absorbers closest to galaxies ( $D_{\text{tran}} < 100 \text{ pkpc}$ ; top left panel of Figure 27) do not appear to exhibit the same systematic “excess” in median  $b_d$  (cf. Figure 26). There are too few galaxies in this inner bin to determine whether the result is statistically significant.

In order to quantify the statistical significance of the apparent excess  $b_d$  in the range  $D_{\text{tran}} < 300 \text{ pkpc}$ , we performed a Monte Carlo simulation. This was done by drawing random samples of absorbers from the full absorber catalogue with the same distribution in  $N_{\text{HI}}$  and of the same size as the absorber sample close to galaxies. The figure of merit was taken to be the average difference computed as follows: in each bin of  $N_{\text{HI}}$  the difference between the median  $b_{d,\text{MC}}$  from the Monte Carlo sample and the median  $b_d$  in the full absorber catalog was computed (asterisks minus black bars in Figure 27). The differences from the  $N_{\text{HI}}$  bins were then averaged. The fraction of Monte Carlo samples whose average  $b_d$  excess is greater than that of the  $D_{\text{tran}} < 300 \text{ pkpc}$  sightline sample is 0.005, meaning the excess is significant at approximately the  $3\sigma$  level.

### 7.2. Doppler Widths vs. 3D Distance

In Figure 28 we consider the distribution of  $b_d$  as a function of  $D_{3\text{D}}$ , which allows one to consider trends as a function of distance without pre-selecting a velocity window. Here again,  $b_d$  is elevated for bins close to galaxies ( $D_{3\text{D}} \lesssim 400 \text{ pkpc}$ ). In the first bin, the median  $b_d \approx 35 \text{ km s}^{-1}$  compared to  $b_d = 27 \text{ km s}^{-1}$  for the random sample.

We again perform a comparison at fixed  $N_{\text{HI}}$  and since the median  $b_d$  monotonically decrease with increasing  $D_{3\text{D}}$ , we consider cumulative distance bins. For absorbers with  $D_{3\text{D}} < 600 \text{ pkpc}$ , the median  $b_d$  for absorbers with  $N_{\text{HI}} < 10^{16} \text{ cm}^{-2}$  is larger than the median measured in the full absorber catalog. Notably, for  $15 < \log(N_{\text{HI}}) < 16$ , absorbers close to galaxies ( $D_{3\text{D}} < 400 \text{ pkpc}$ ) have a median  $b_d > 40 \text{ km s}^{-1}$ . If interpreted as the result of an increase in gas temperature, the change in  $b_d$  is equivalent to more than doubling  $T$ . We also note that these intermediate  $N_{\text{HI}}$  systems that are characteristic of the CGM tend also to be associated with the strongest high ionization metals (O VI, C IV), often exhibiting evidence that the ionization has been produced by shocks in addition to photoionization (Simcoe et al. 2002).

As previously stated, the 3D distance is strongly influenced by the magnitude of  $|\Delta v|$ . Notably, the first three bins in  $D_{3\text{D}}$  (those with the most significant deviation in  $b_d$ ) correspond to absorbers with  $|\Delta v| < 150 \text{ km s}^{-1}$ .

<sup>33</sup> Note that within the full catalog for absorbers whose growth is expected to remain approximately linear ( $N_{\text{HI}} < 10^{15} \text{ cm}^{-2}$ ,  $\rho/\bar{\rho} \lesssim 10$ ), the median values (black horizontal lines) exhibit increasing  $b_d$  with increasing  $N_{\text{HI}}$ , as one would expect for the  $T - \rho$  relation.



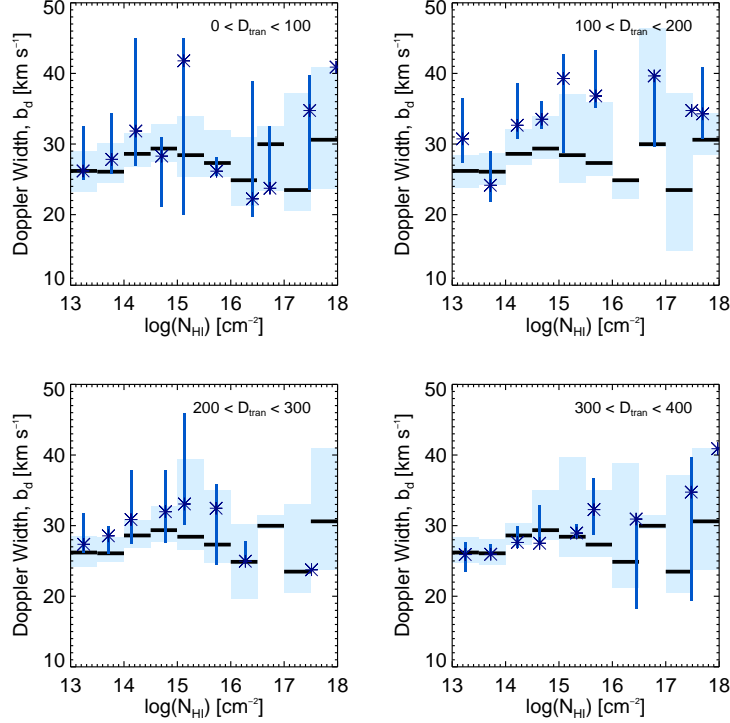


**Figure 27.** Comparison at fixed  $N_{\text{HI}}$  of absorbers close to galaxies with absorbers in the full HI catalog. The different panels show four bins of  $D_{\text{tran}}$ . Asterisks represent the median value of  $b_d$  in a bin of  $N_{\text{HI}}$  for absorbers close to galaxies. The horizontal black lines show the median  $b_d$  of absorbers from the full HI catalog, and the light shaded boxes represent their dispersion calculated through bootstrap samples of the same size as those in the real sample. The velocity window is  $|\Delta v| < 700 \text{ km s}^{-1}$ . In the bins without asterisks, there were no absorbers which satisfied both the  $D_{\text{tran}}$  and  $N_{\text{HI}}$  criterion; similarly, asterisks without error bars represent bins containing only a single absorber satisfying both the  $D_{\text{tran}}$  and  $N_{\text{HI}}$  criterion. Recall from Figure 26 that the strongest signal occurred at  $100 < D_{\text{tran}} < 200 \text{ pkpc}$  (shown in this Figure in the top right panel). Note that the median  $b_d$  of all absorbers close to galaxies with  $N_{\text{HI}} > 10^{14} \text{ cm}^{-2}$  are larger than those in the full absorber catalog.

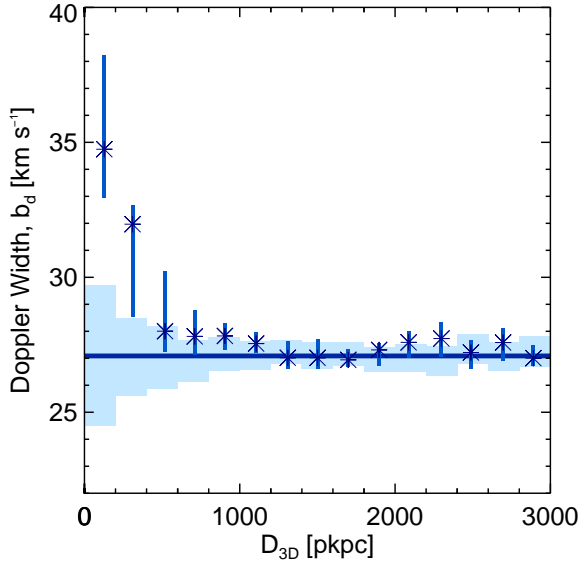


**Figure 28.** Same as Figure 26 but versus the 3D distance.

In summary, considering the trends illustrated in Figures 26 – 29, it appears that absorbers of all  $N_{\text{HI}}$  with  $100 < D_{\text{tran}} < 300 \text{ pkpc}$  and  $|\Delta v| < 150 \text{ km s}^{-1}$  have significantly larger Doppler widths than absorbers of the same  $N_{\text{HI}}$  in the full absorber sample.

### 7.3. Doppler Parameter: Possible Physical Explanations

The trends in Doppler widths,  $b_d$ , could have a variety of physical origins. As previously discussed, elevated  $b_d$  could be related to the observed trend in  $N_{\text{HI}}$  through the  $T - \rho$  relation in the IGM. However, we showed that at *fixed*  $N_{\text{HI}}$ , the median  $b_d$  of absorbers close to galaxies is still significantly larger than in the full absorber catalog (Figures 27 and 29). This suggests that the  $T - \rho$  relationship alone cannot account for the broader absorption lines close to galaxies.

Another possible contributor to increasing  $b_d$  near galaxies is a change in the *ionization* at a given  $N_{\text{HI}}$ . If the galaxy itself produces a significant fraction of the local ionizing radiation field (i.e., in excess of that of the metagalactic UV background), then  $N_{\text{HI}}/N_{\text{H}}$  would be smaller near galaxies. The fraction of the ionizing photons which escape the ISM of the galaxy is small (Nestor et al. 2011, Steidel et al. in prep), but their number, compared to the UV background is likely significant within  $\sim 100 \text{ pkpc}$ . In this case, the  $T - \rho$  relation could hold, but the mapping of  $N_{\text{HI}}$  to  $\rho$  would be altered. If this were the case, we would expect the locations of the asterisks in Figures 27 and 29 to be consistent with a leftward shift of the black bars. However, this scenario is at odds with the observation that the median  $b_d$  of absorbers with  $10^{14} < N_{\text{HI}} < 10^{16} \text{ cm}^{-2}$  and  $100 < D_{\text{tran}} < 200 \text{ pkpc}$  is higher than the median  $b_d$  for any bin in  $N_{\text{HI}}$  observed in the full absorber catalog (Figure 27). The same is true of absorbers with  $D_{3\text{D}} < 400 \text{ pkpc}$  and  $10^{14} < N_{\text{HI}} < 10^{16} \text{ cm}^{-2}$  (Figure 29).

Assuming that overdensity is not the main cause of the increased  $b_d$ , we consider other plausible processes which could

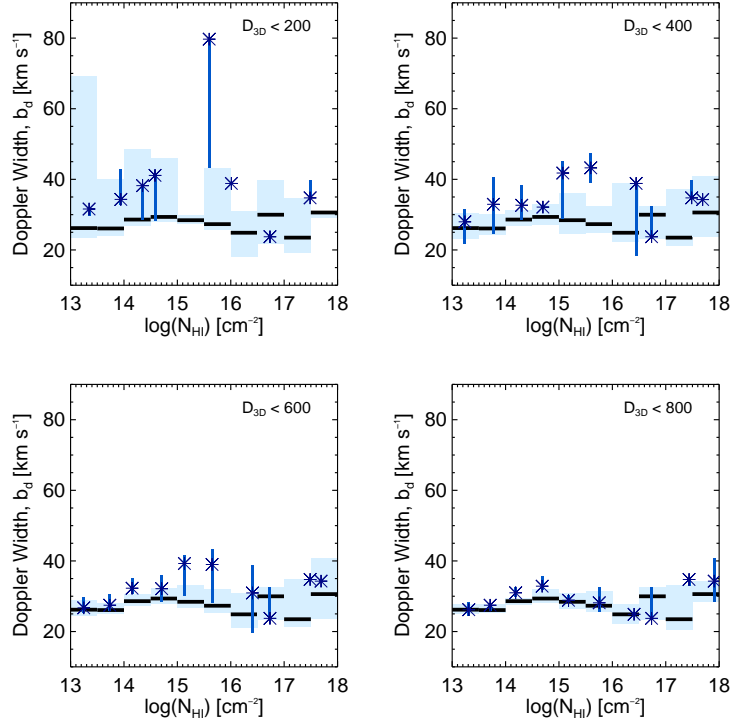


**Figure 29.** Same as Figure 27 but now divided into bins of 3D distance,  $D_{3D}$ , and with cumulative bins in  $D_{3D}$ . From Figure 28 one notes that the majority of the signal results from  $D_{3D} < 400$  pkpc (shown in this Figure in the upper two panels). Notably, absorbers near galaxies have higher  $b_d$  at nearly all values of  $N_{\text{HI}}$  at these impact parameters. Because the signal from all bins is combined, higher  $b_d$  at fixed  $N_{\text{HI}}$  is evident for absorbers with  $D_{3D} < 600$  pkpc.

lead to an increase in the temperature or turbulence of the gas. In principle it is possible to disentangle the source of the broadening (turbulent vs. thermal) by comparing the widths of absorption lines arising from ions with different atomic weights. The thermal broadening component,  $b_d(T)$ , depends on atomic mass, while the turbulent broadening component will remain constant so long as the ions reside in the same gas. While the HIRES QSO spectra in our sample include metal absorption lines which could be used for this purpose, the analysis of the metal lines is beyond the scope of this paper and will be presented elsewhere. At present, we consider the implications of both possible effects (temperature and turbulence).

Referring to Figure 28, there is an increase in the median  $b_d$  from  $27 \text{ km s}^{-1}$  to  $35 \text{ km s}^{-1}$ . Assuming purely thermal broadening, these values would indicate  $T = 4.4 \times 10^4 \text{ K}$  and  $7.4 \times 10^4 \text{ K}$ , respectively, or an increase in temperature of 68%. If we consider the absorbers with  $b_d \gtrsim 40 \text{ km s}^{-1}$  as in Figure 29, these suggest a temperature of  $\sim 10^5 \text{ K}$ . If instead the increase in line width is due to turbulence, an excess turbulent velocity of  $20\text{-}30 \text{ km s}^{-1}$  would account for the departure from the  $b_d = 27 \text{ km s}^{-1}$  global median. In either case, it is curious that the elevated Doppler widths occur in gas with  $100 < D_{\text{tran}} < 300$  pkpc but are not detected in the bin from  $0 - 100$  pkpc. While the non-detection at the smallest impact parameters is likely not significant, clearly, whichever mechanism is responsible for this increase in width is acting significantly outside of the typical galaxy virial radius ( $\sim 90$  pkpc).

Unless AGN are involved (galaxies with detected AGN signatures were not used in our analysis), excess photo-heating for material closer to galaxies seems unlikely, since the UV radiation field from local stellar sources is likely to be (if

anything) softer than the metagalactic background believed to dominate at an average IGM location.

There are at least two plausible processes which could increase  $b_d$  in the CGM of galaxies: galactic winds (outflows) and baryonic accretion. Accreting gas can be heated by shocks forming as the gas falls into galaxy halos. The galaxies in our sample have halo masses comparable to the theoretically expected transition mass between “cold mode” and “hot mode” accretion (van de Voort et al. 2011b; Faucher-Giguère et al. 2011; Kereš et al. 2009; Ocvirk et al. 2008); most of these authors predict that both hot and cold accretion occur in such halos at  $z > 2$ . The virial temperature for galaxies with halos of mass  $\sim 10^{12} M_{\odot}$  is expected to be  $T_{\text{vir}} \simeq 10^6 \text{ K}$  (van de Voort et al. 2011b), and Kereš et al. (2009) suggest that this hot gas may fill the volume surrounding galaxies to a few  $r_{\text{vir}}$ . The HI absorbers in our sample are unlikely to trace gas this hot, however gas cooling from this temperature would be detectable.

The interaction of cool dense gas with either a hot halo or a rarified wind fluid is also expected to produce turbulent boundary layers via both Rayleigh-Taylor<sup>34</sup> and Kelvin Helmholtz<sup>35</sup> instabilities (Kereš & Hernquist 2009; Faucher-Giguère & Kereš 2011). These boundary layers are also where metallic ions such as O VI are expected to be most abundant.

Galactic super winds can naturally explain either thermal

<sup>34</sup> Rayleigh-Taylor instabilities would form in the case of a lighter, less-dense fluid lying deeper in the gravitational potential of the galaxy than a denser cold-stream.

<sup>35</sup> Kelvin Helmholtz instabilities would form in the condition where the dense stream was moving with respect to the hot medium. This is especially plausible in the case of a fast moving galactic wind or a filament moving at the free-fall velocity.

or turbulent broadening, potentially to large distances away from galaxies. The favored mechanism for large scale winds is shocks from supernovae which could easily increase the gas temperature of the ambient medium. Although the distance to which galactic winds propagate is not well constrained, there is evidence that they expand to at least  $r_{\text{vir}}$  (Steidel et al. 2010). Shen et al. (2011) recently considered high-resolution “zoom-in” simulations of a single Lyman Break Galaxy<sup>36</sup> at  $z = 3$ . In their model, the LBG itself (as opposed to its satellite galaxies) enriches the IGM with metals from supernovae-driven winds to  $3r_{\text{vir}}$  (see their Figure 9). Kollmeier et al. (2006) considered the effect of winds on the CGM of star-forming galaxies at  $z = 3$  and found that winds could have a profound effect on the temperature of nearby gas: varying the energy released by supernovae in their simulations by a factor of 5 changed the temperature of gas close to galaxies by  $\sim 250\%$  (see their Figure 10). More recently, van de Voort & Schaye (2011) considered the physical properties of gas surrounding galaxies with halo masses  $M_{\text{DM}} = 10^{12} M_{\odot}$  at  $z = 2$  as a function of the kinematics of the gas (i.e. inflowing vs. outflowing). They found a radial temperature profile of outflowing gas qualitatively consistent with the observed increase in  $b_d$ . Outflows are also predicted to drive gas turbulence outside of virial halos through the conversion of kinetic energy from supernova driven bubbles into random motions through gas instabilities (see e.g., Evoli & Ferrara 2011).

While the exact cause of the enlarged line widths is not apparent, it is clear that the physical state of the gas within  $\sim 300$  pkpc is markedly different from that in “random” locations in the IGM - suggesting that galaxies and their potential wells deeply affect their surrounding CGM. This fact may introduce significant complications to studies of the general IGM which will be discussed further in §8.5.

## 8. GENERAL DISCUSSION

In §4 – 7 we presented measurements and plausible interpretations of the properties of neutral hydrogen gas surrounding star-forming galaxies at high  $z$ . Here, we speculate on the possible implications of the observed trends.

### 8.1. Gaseous “Zones” around Galaxies

The distribution of strong absorbers (Figure 9) and of the incidence of absorbers (Figures 16 and 17) suggest three distinct “zones” in the gaseous envelopes surrounding galaxies.

1. The first zone corresponds to the volume within  $D_{\text{tran}} < 300$  pkpc. For scale, the virial radius of a typical galaxy in our sample is  $\sim 90$  pkpc. Inside 300 pkpc, the values of the  $\max(N_{\text{HI}})$  statistic are significantly elevated and rise toward the position of the galaxy (Figure 9). Figure 16 shows rising  $\eta_{\text{abs}}$  with decreasing  $D_{\text{tran}}$  for the three bins within 300 pkpc. Similarly, at 300 pkpc,  $\eta_{\text{abs}}$  for absorbers with  $N_{\text{HI}} > 10^{14.5}$  drops sharply. In Figure 17, again at 300 pkpc one sees a rapid drop in the incidence of all absorbers with  $N_{\text{HI}} > 10^{14.5} \text{ cm}^{-2}$ .
2. The second zone lies between  $300 \text{ pkpc} < D_{\text{tran}} \lesssim 2 \text{ pMpc}$ . In Figure 9, we observed that  $\max(N_{\text{HI}})$ , while high compared to the random distribution, plateaus at a roughly constant value within this zone.  $\eta_{\text{abs}}$  also plateaus over the same range as shown in Figures 16 and 17.

<sup>36</sup> Lyman Break Galaxies at  $z = 3$  have very similar properties to the galaxies studied in this paper.

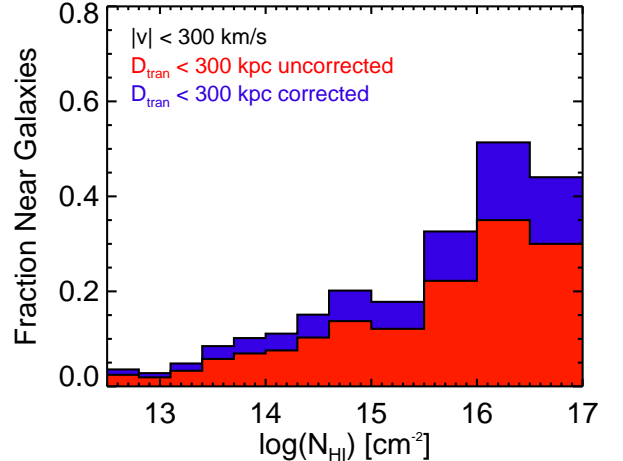


**Figure 30.** The fraction of all H I systems in our QSO sightlines that arise within  $|\Delta v| < 300 \text{ km s}^{-1}$  and  $D_{\text{tran}} < 300 \text{ pkpc}$  of the position of a galaxy in our spectroscopic galaxy sample (lighter red histogram), as a function of  $N_{\text{HI}}$ . The darker (blue) histogram indicates the fraction after correcting for the fact that not all galaxies in the photometric sample have been observed spectroscopically. These corrected points thus reflect the fraction of absorbers arising within the CGM of galaxies that meet our *photometric* selection criteria.

3. The third zone corresponds to  $D_{\text{tran}} \gtrsim 2 \text{ pMpc}$ . The transition between the second and third zone is not a sharp feature; rather between  $\sim 2 - 3 \text{ pMpc}$ , the distribution of absorbers as seen in the  $\max(N_{\text{HI}})$  and  $\eta_{\text{abs}}$  statistics drops to become consistent with (or below that of) the IGM median.

Three distinct zones are also evident in the velocity distribution of absorbers.

1. The first zone, corresponding to the strongest peak in the velocity distribution, is within  $|\Delta v| < 300 \text{ km s}^{-1}$  (Figures 6 and 7).
2. The second velocity zone includes gas to  $|\Delta v| \approx 700 \text{ km s}^{-1}$ , which encompasses the full extent of the excess  $N_{\text{HI}}$  (Figures 5 and 6).
3. The third zone is  $|\Delta v| > 700 \text{ km s}^{-1}$ , where the distribution with respect to galaxies is consistent with that of random locations (Figures 5 and 6).

Note that in Figure 7, the median  $N_{\text{HI}}$  of absorbers with  $D_{\text{tran}} < 300 \text{ pkpc}$  exhibits a sharp drop-off at  $|\Delta v| \geq 300 \text{ km s}^{-1}$  suggesting that absorbers at  $D_{\text{tran}} > 300 \text{ pkpc}$  are likely responsible for the excess absorption at  $300 < |\Delta v| < 700 \text{ km s}^{-1}$ .

### 8.2. Defining the CGM

We adopt a working definition of the “circumgalactic medium” (CGM) as the region within  $|\Delta v| < 300 \text{ km s}^{-1}$  and  $D_{\text{tran}} < 300 \text{ pkpc}$  of a galaxy. Figure 30 shows (in red) the fraction of absorbers from the full absorber catalog which fall within the CGM of a galaxy *in our spectroscopic sample* as a function of  $N_{\text{HI}}$ .

Our spectroscopic galaxy sample is 70% complete with respect to the photometric parent sample within 300 pkpc of the

line-of-sight to the QSOs.<sup>37</sup> The blue histogram in Figure 30 has been corrected for this incompleteness assuming that unobserved galaxies have the same overall redshift distribution and similar CGM to those that have been observed. Figure 30 shows that  $\gtrsim 20\%$  of all absorbers with  $\log(N_{\text{HI}}) > 14.5$  and  $\gtrsim 40\%$  of those with  $\log(N_{\text{HI}}) > 15.5$  arise in the CGM of galaxies that meet our selection criteria. Noting that the co-moving number density of identically selected galaxies (with the same limiting magnitude of  $\mathcal{R} = 25.5$ ) is  $\Phi = 3.7 \times 10^{-3} \text{ cMpc}^{-3}$  (Reddy et al. 2008), the CGM of LBGs at  $\langle z \rangle = 2.3$  contains only  $\simeq 1.5\%$  of the Universe’s volume but accounts for nearly half of the total gas cross-section for  $N_{\text{HI}} > 10^{15.5} \text{ cm}^{-2}$ . This is perhaps surprising given that our sample includes only galaxies with  $L_{\text{UV}} \geq 0.25L_{\text{UV}}^*$  and the faint-end slope of the UV luminosity function is very steep at  $z \sim 2.3$ ; however, it is consistent with previous results based on strong metal-line absorption around similar galaxies at comparable redshifts (Adelberger et al. 2003, 2005a; Steidel et al. 2010).

The situation changes substantially for  $N_{\text{HI}} \lesssim 10^{14.5} \text{ cm}^{-2}$ ; we have seen that these lower  $N_{\text{HI}}$  absorbers are more loosely associated with galaxies in our sample, though their incidence is enhanced by  $\sim 10\text{--}20\%$  relative to average locations in the IGM (e.g. see the top panels of Figure 16).

Stated another way, we have found that low and high-column density absorbers cluster differently with high- $z$ , UV-bright galaxies. We showed (Figure 16) that absorbers with  $\log(N_{\text{HI}}) > 14.5$  exhibit a much stronger peak in incidence towards the positions of galaxies than do the absorbers with lower column densities. Similarly, in maps of the incidence (Figures 21 – 24) low-column density absorbers show only large scale correlation with the positions of galaxies while high-column density absorbers again showed a strong peak near galaxies both along the line of sight and in  $D_{\text{tran}}$ .

Collectively, these lines of evidence point to a circumgalactic zone defined by the boundaries of  $|\Delta v| < 300 \text{ km s}^{-1}$  and  $D_{\text{tran}} < 300 \text{ pkpc}$  and dominated by absorbers with  $\log(N_{\text{HI}}) > 14.5$ . They also suggest that only systems with  $\log(N_{\text{HI}}) \lesssim 14 \text{ cm}^{-2}$  are confidently “IGM” – as  $N_{\text{HI}}$  increases beyond this limit, the likelihood that the gas lies within the CGM of a relatively bright galaxy increases very rapidly.

### 8.3. Small Scale Distribution of $N_{\text{HI}}$

In an effort to understand the physics responsible for the distribution of  $N_{\text{HI}}$  as a function of transverse distance from galaxies, we compare the data to two theoretical models. First we consider the possibility that the H I column density traces the dark matter halo density profile.

The typical dark matter halo hosting a galaxy in our sample is theoretically expected to follow a NFW (Navarro et al. 1997) density profile:

$$\rho(r) = \frac{\rho_c(z) \delta_{\text{NFW}}}{c \frac{r}{r_{\text{vir}}} \left(1 + c \frac{r}{r_{\text{vir}}}\right)^2} \quad (20)$$

where  $\delta_{\text{NFW}}$  is a normalization defined as

$$\delta_{\text{NFW}} = \frac{200}{3} \frac{c^3}{\ln(1+c) - \frac{c}{1+c}} \quad (21)$$

and  $\rho_c$  is the critical density,  $c$  is the concentration parameter of the dark matter halo which we take to be  $c = 4$  following

<sup>37</sup> Our absorption line catalogue is essentially 100% complete for absorbers with  $\log(N_{\text{HI}}) \gtrsim 13$ .

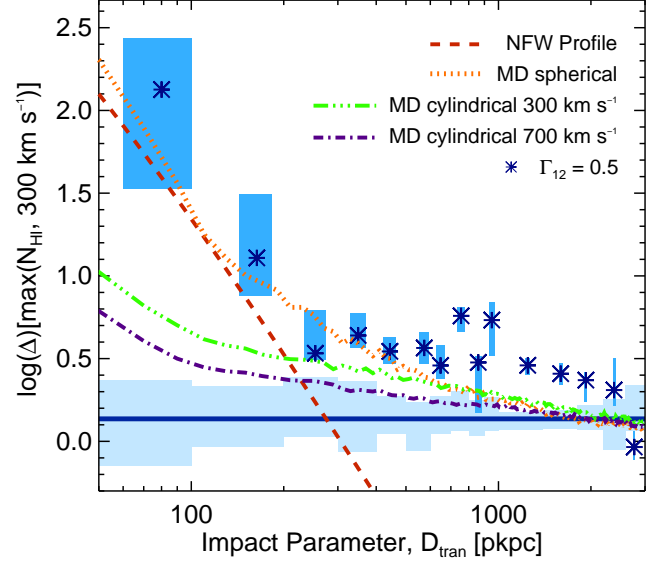


**Figure 31.** The  $\max(N_{\text{HI}}, 300 \text{ km s}^{-1})$  statistic, converted into a universal overdensity using Schaye (2001) plotted against transverse distance to a galaxy on a logarithmic scale. The same data shown in Figure 10 with two models over-plotted for comparison. Here we use 100 pkpc bins within 1 pMpc and 400 pkpc bins at larger  $D_{\text{tran}}$  to simplify the plot. Shown in the (red) dashed line is the NFW radial density profile plotted as a universal overdensity. See text for more details. Shown in the light (orange) dotted, light (green) dash-dotted, and dark (purple) dash-dotted lines are the average dark matter profiles from the MultiDark simulation for halos with  $M_{\text{DM}} > 10^{11.8} M_{\odot}$ . The light (orange) dotted curve is the median value (across the halos considered) of the average density in concentric spherical shells of radius  $D_{\text{tran}}$ . The light (green) dash-dotted curve is the median (across the halos considered) of the average dark matter density in concentric cylindrical shells of radius  $D_{\text{tran}}$  and length  $\pm 300 \text{ km s}^{-1} = \pm 1200 \text{ pkpc}$ . The dark (purple) dash-dotted curve is analogous to the green one, but the velocity window is  $\pm 700 \text{ km s}^{-1}$ .

Duffy et al. (2008), and  $r_{\text{vir}}$  is the virial radius for halos of average mass  $10^{12} M_{\odot}$  (91 pkpc; Trainor & Steidel, in prep; Conroy et al. 2008; Adelberger et al. 2005b).

We define  $\Delta$ , the matter overdensity, as:

$$\Delta = \frac{\rho}{\bar{\rho}} = \frac{\rho}{\Omega_{\text{M}}(1+z)^3 \rho_c(z=0)} \quad (22)$$

Noting the definition for the critical density:

$$\rho_c(z) = \frac{3H^2(z)}{8\pi G} \quad (23)$$

we can then express the NFW profile as a function of overdensity, rather than density:

$$\Delta_{\text{NFW}}(r) = \frac{1}{\Omega_{\text{M}}(1+z)^3} \frac{\delta_{\text{NFW}}}{c \frac{r}{r_{\text{vir}}} \left(1 + c \frac{r}{r_{\text{vir}}}\right)^2} \frac{H^2(z)}{H_0^2} \quad (24)$$

Using Jeans scale arguments, Schaye (2001) defined a scaling function which relates the gas overdensity ( $\rho_b/\bar{\rho}_b$ ) to an expected value of  $N_{\text{HI}}$ . While on the smallest scales where the growth is highly non-linear it is certainly not the case that  $\rho_b/\bar{\rho}_b$  is equal to  $\Delta$ , the matter overdensity (which is dominated by dark matter), the expectation is that they should mirror each other well at low overdensity ( $\Delta \approx 1\text{--}10$ ) where the growth is yet to become significantly non-linear. We therefore assume  $\rho_b/\bar{\rho}_b \approx \Delta$ , in order to compare our measured  $\max(N_{\text{HI}})$  to theoretical density profiles. For the cosmology

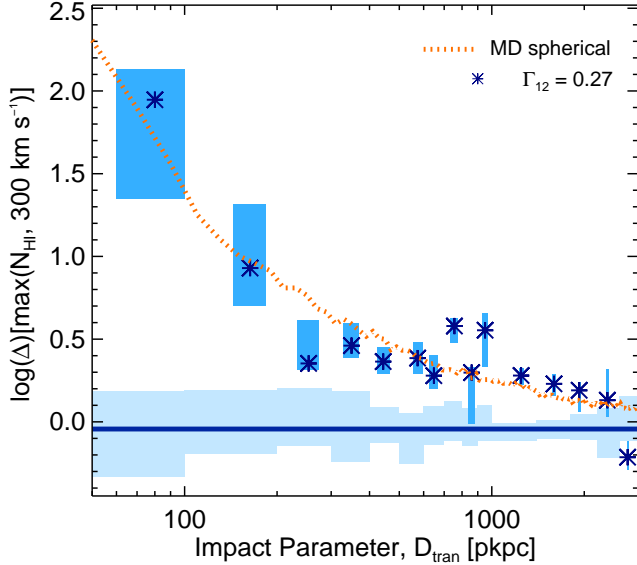


**Figure 32.** Same as Figure 31 but using a different normalization of the photoionization rate. In Figure 31 the data values were converted into  $\Delta$  assuming  $\Gamma_{12} = 0.5$  as suggested by Faucher-Giguère et al. (2008). Here, the data values are converted into  $\Delta$  assuming  $\Gamma_{12} = 0.27$  which bring them into the closest agreement with the MultiDark spherical density profile measurements.

used in this paper, at the redshifts of our sample, the scaling function from Schaye (2001) is:

$$\Delta \approx \left( \frac{N_{\text{HI}}}{10^{13.4}} \right)^{2/3} T_4^{0.17} \left( \frac{\Gamma_{12}}{0.5} \right)^{2/3} \left( \frac{1+z}{3.3} \right)^{-3}, \quad (25)$$

where  $T_4$  is the gas temperature in units of  $10^4$  K and  $\Gamma_{12}$  is the hydrogen photoionization rate in units of  $10^{-12} \text{ s}^{-1}$  where the normalization is taken from Faucher-Giguère et al. (2008). Using this relation, we can convert our  $\max(N_{\text{HI}})$  statistic into  $\Delta$  which can then be compared to the rescaled NFW profile.

The values after converting  $\max(N_{\text{HI}})$  to  $\Delta$  are shown in Figure 31. The (red) dashed curve is the NFW density profile (Equation 24). The NFW halo has a radial distribution similar to that of the  $\Delta$  inferred from our  $\max(N_{\text{HI}})$  statistic for small  $D_{\text{tran}}$ , but falls well below the Jeans-scale-inferred overdensity for  $D_{\text{tran}} \gtrsim 300$  pkpc. This is expected since the NFW profile is measured in simulations for dark matter (DM) within the virial radius. In the following section, we compare to the DM density on larger scales using DM profiles drawn directly from simulations.

#### 8.4. Large Scale Distribution of $N_{\text{HI}}$

Considering the distribution of gas around galaxies on Mpc scales, it is interesting to note the similarity between the scale over which circumgalactic gas has higher density than an average location in the IGM ( $D_{\text{tran}} \lesssim 2$  pMpc) and the galaxy-galaxy autocorrelation scale length recently measured from the same galaxies,  $r_0 = (6.5 \pm 0.5)h^{-1} \text{ cMpc}$  ( $\simeq 2.8$  pMpc at  $\langle z \rangle = 2.3$ ; Trainor & Steidel, in prep). It would not be surprising if they were closely related.

Most of the recent work on the dark matter density profiles at several  $r_{\text{vir}}$  and beyond have focused on the local universe. Since we are interested in comparing the gas-inferred density profiles with an average dark matter profile at  $z \sim 2-3$ , we created median DM density profiles using the MultiDark sim-

ulation (Klypin et al. 2011). The radial density profile within 3 pMpc was computed from 100 halos with  $M_{\text{DM}} > 10^{11.8} M_{\odot}$ <sup>38</sup>. Here we consider the dark matter density profile measured in two ways presented in terms of universal overdensity as shown in Figure 31. (1) First, we consider the average density in concentric spherical shells of radius  $D_{\text{tran}}$  centered on the position of each halo. We take the median of this profile across the 100 halos considered (light orange dotted curve) and compare it to the  $\max(N_{\text{HI}}, 300 \text{ km s}^{-1})$  statistic converted into overdensity using equation 25. (2) We also consider the average dark matter density profile computed within concentric cylindrical shells of radius  $D_{\text{tran}}$  and length  $\Delta v = \pm 300 \text{ km s}^{-1}$  ( $\pm 1200$  pkpc) as shown in the light (green) dash-dotted curve. We consider the effect of the velocity window used as well - the dark (purple) dash-dotted curve is analogous to the green curve, but with a cylinder length of  $\pm 700 \text{ km s}^{-1}$ .

The spherically-averaged radial density profile is well-matched by the NFW profile on small scales as expected (Figure 31). After 200–300 pkpc (the same scale as the first “zone” of the CGM, §8.1), the spherically averaged radial density profile flattens compared with NFW. From  $\sim 200$ –300 pkpc onwards, the inferred density declines smoothly, falling to the mean density of the universe [ $\log(\Delta) = 0$ ] at  $D_{\text{tran}} > 3$  pMpc.

The cylindrically averaged density profile significantly dilutes the signal in the inner bins of  $D_{\text{tran}}$  suggesting that the  $\max(N_{\text{HI}})$  statistic traces more of a radial distribution than a “line-of-sight” distribution on small scales. On larger scales, the cylindrical and spherically averaged density profiles look quite similar. Between  $D_{\text{tran}} \approx 1.5 - 2$  pMpc, the two cylindrically averaged curves become consistent with each other. This suggests that on scales of  $\sim 2$  pMpc the density along a sightline between  $\pm 300 \text{ km s}^{-1}$  and  $\pm 300$  to  $\pm 700 \text{ km s}^{-1}$  is similar – as one would expect far from galaxies as the density approaches the universal mean.

The density inferred from the H I measurements is markedly higher on  $\sim$  pMpc scales than is predicted by either MultiDark DM density profile. There are three possible causes for this discrepancy: (1) It may be the case that the  $\max(N_{\text{HI}})$  statistic traces high-density substructure while the radial density profiles drawn from the simulations are (by construction) smoothed - averaging over these structures. The assumption of Jeans smoothing intrinsic to the arguments of Schaye (2001) should minimize the discrepancy; however, it is likely still that substructure may affect our max statistics. (2) One or more of the assumptions used in the Schaye (2001) conversion between  $N_{\text{HI}}$  and  $\Delta$  could be invalid. For example one of the more uncertain quantities required in the conversion is the H I photoionization rate,  $\Gamma$ <sup>39</sup>. In Figure 32 we consider the change in the value of  $\Gamma$  needed to bring the measured  $\Delta[\max(N_{\text{HI}}, 300 \text{ km s}^{-1})]$  into agreement with the spherically averaged dark matter density profile. This plot suggests a normalization  $\sim 40\%$  lower than the estimates from Faucher-Giguère et al. (2008).<sup>40</sup> (3) Another possibility

<sup>38</sup> The halo mass was inferred from the number of particles found to “belong” to a halo using the Friends-of-Friends algorithm. The halo-mass cut of  $10^{11.8} M_{\odot}$  is the same mass threshold which reproduces the clustering of galaxies in our spectroscopic sample, as described in Trainor & Steidel (in prep). The mean and median halo masses of galaxies with this halo-mass threshold are  $10^{12.2} M_{\odot}$  and  $10^{12} M_{\odot}$ , respectively.

<sup>39</sup>  $\Gamma_{12}$  refers to the photoionization rate in units of  $10^{-12} \text{ s}^{-1}$ .

<sup>40</sup> The temperature of the gas is another quantity that could be adjusted. The temperature assumed currently is  $10^4$  K. To match our observations we

is that Jeans scale arguments do not hold in detail on these scales.<sup>41</sup>

### 8.5. The Implications of the Distinct Physics of the CGM

The final point is a note of caution regarding the effect the CGM of luminous galaxies may have on measurements which rely on “average” locations in the IGM. In addition to the rising  $N_{\text{HI}}$  and  $\eta_{\text{abs}}$  observed in the CGM of galaxies, we have shown that the physical state of the absorbing gas in this region is also distinct from the general IGM. The Doppler widths,  $b_d$ , of individual absorbers are significantly larger in the CGM zone, even when compared at *fixed*  $N_{\text{HI}}$ . Further, absorbers with  $N_{\text{HI}} > 10^{14.5}$  cluster tightly with galaxies (Figures 16, 17, and 22), and these absorbers are found in the CGM zone with very high frequency (Figure 30).

Taken together, these observations suggest that the physics of the “IGM” which has long been leveraged for measurements varying from the metagalactic background to the matter power spectrum, may be significantly affected by the baryonic physics of galaxy formation; particularly, low-resolution IGM studies dominated by H I absorbers  $\sim$ saturated in Ly $\alpha$  ( $N_{\text{HI}} > 10^{14.5} \text{ cm}^{-2}$ ) are likely to be affected by the presence of a nearby galaxy. Further observational and theoretical examination of this subject is crucial to a full understanding of the measurement power of the IGM.

In addition, studies of the distribution of metal absorption lines in the “IGM” often consider metallic species associated with HI absorbers of  $\log(N_{\text{HI}}) \gtrsim 14.5$  (Cowie et al. 1995; Songaila & Cowie 1996; Ellison et al. 2000; Carswell et al. 2002; Simcoe 2011). To a large degree, this is a practical choice as the associated metal absorbers occurring in sub-solar metallicity gas must be found and measured in spectra of finite S/N. However, the properties of the CGM discussed above suggest that, as many authors have speculated, these measurements more directly probe the metallicity of the CGM than that of the IGM. Observations at  $z \gtrsim 5$  generally cannot measure the  $N_{\text{HI}}$  associated with metal systems due to the line density of the forest, but they are likely to suffer from the same effect, adding credence to the idea that the recent discovery of the high- $z$  downturn of C IV (Ryan-Weber et al. 2006, 2009; Becker et al. 2009, 2011b; Simcoe et al. 2011) likely also traces CGM gas.

The observations of circumgalactic and intergalactic gas and its association with forming galaxies have now progressed to the point that more stringent comparison to theoretical expectations is possible. Even using the comparatively “blunt” tool of gas covering fraction, we have shown (§5.2) that the distribution of HI gas around galaxies exceeds the expectations of the models to which they have been compared, with the discrepancy increasing as  $N_{\text{HI}}$  decreases below  $10^{17} \text{ cm}^{-2}$ . It is clear that a combination of high-resolution (to capture the small-scale baryon physics) and cosmological (to provide sufficient statistical leverage) simulations will be required to make use of the more detailed physical measurements emerging from the observations: e.g., gas-phase kinematics, multi-phase velocity/density structure, redshift-space

would need to significantly lower the temperature assumed to  $T < 10^3 \text{ K}$  which is unlikely to be the case. If anything,  $10^4 \text{ K}$  is likely a *lower* limit on the temperature of the IGM at  $z \sim 2$  (see e.g., Becker et al. 2011a).

<sup>41</sup> We tested the agreement between the aforementioned models and our data converted using the Fluctuating Gunn-Peterson Approximation (FGPA; Rauch et al. 1997), finding that the disagreement is larger. Rakic et al. (2011b) also compare several methods for converting between H I optical depth (akin to  $N_{\text{HI}}$ ) and overdensity (see their §4.5).

distortions, gas temperatures, turbulence, the distribution and mixing of metals, all as a function of galaxy properties. In order to match the real universe, simulations will need to realistically model the physics of feedback from star formation, supernovae, and AGN activity and its effect on gas-phase accretion from the CGM.

It will be important for future simulations to have sufficient dynamic range to make predictions about the distribution of neutral hydrogen with  $13 < \log(N_{\text{HI}}) < 20$ . The physical picture advocated by most modern theoretical treatments of the “IGM” is that the Ly $\alpha$  forest traces gas of modest overdensity within the filaments of the “cosmic web”. The high covering fractions found in this study (e.g., the relatively large  $f_c$  of saturated HI extending  $\gtrsim 2 \text{ pMpc}$  from  $\sim 10^{12} M_\odot$  dark matter halos; §5) suggest that if this picture holds, the size of these filaments may remain quite large even as they approach the positions of high-bias halos. These initial comparisons suggest that the topology of the neutral hydrogen gas may be less “filamentary” (at all column densities) than current simulations of the “cosmic web” and “cold accretion” predict. If such disagreement between simulations and observations are common and persist they may become key to a deeper understanding of the baryon physics that ultimately controls the process of galaxy formation.

## 9. SUMMARY

In this paper we have presented a detailed study of neutral hydrogen in the IGM surrounding 886 high- $z$  star-forming galaxies using spectra of background QSOs from the Keck Baryonic Structure Survey. We draw conclusions from the analysis of 15 sightlines to hyper-luminous high- $z$  QSOs using high-resolution ( $7 \text{ km s}^{-1}$ ), high-signal-to-noise ratio (50-200) spectra. This study constitutes the largest absorption line catalog ever created at these redshifts through a complete Voigt profile decomposition of the Ly $\alpha$  forest for all 15 sightlines. The high S/N and excellent UV/blue-wavelength coverage of the HIRES QSO spectra allow precise determination of the column densities of saturated H I absorption systems whose positions we have found to correlate strongly with those of the galaxies in our sample. This sample is also considered by Rakic et al. (2011b) who analyze the pixel statistics of the H I optical depth.

In this work, we study the absorption patterns of H I gas in the velocity and spatial locations surrounding each galaxy redshift. We have examined the correlations among column density ( $N_{\text{HI}}$ ), covering fraction ( $f_c$ ), incidence ( $\eta_{\text{abs}}$ ), absorption line width ( $b_d$ ), galactocentric transverse distance ( $D_{\text{tran}}$ ), velocity offset ( $\Delta v$ ), and 3D distance ( $D_{3D}$ ). Our principal results are as follows:

1. The redshifts of H I absorption systems in the QSO spectra correlate strongly with the redshifts of galaxies (§4.1). The distribution of relative velocities ( $\Delta v$ ) is peaked at the systemic redshift of galaxies in our sample (Figure 5). The full excess absorption near galaxies falls within  $\pm 700 \text{ km s}^{-1}$  with the majority of the excess  $N_{\text{HI}}$  (i.e. the higher column density absorbers) falling within  $\pm 300 \text{ km s}^{-1}$  (Figures 6 and 7).
2. The column density ( $N_{\text{HI}}$ ) of absorbers is strongly correlated with the impact parameter to a galaxy ( $D_{\text{tran}}$ , §4.2). We consider the highest- $N_{\text{HI}}$  absorber within  $\pm 300 \text{ km s}^{-1}$  [ $\max(N_{\text{HI}})$ ] of each of the 10 galaxies within 100 physical kpc and find that the median value

is 3 orders of magnitude higher than at random places in the IGM (Figure 10). A trend of rising column densities as a function of decreasing  $D_{\text{tran}}$  is observed within the inner 300 physical kpc (1 cMpc) surrounding galaxies (Figures 9, 10, and 11).

3. The column densities ( $N_{\text{HI}}$ ) of absorbers as measured through the  $\max(N_{\text{HI}})$  statistic plateau in the range  $300 \text{ pkpc} < D_{\text{tran}} \lesssim 2 \text{ pMpc}$  (Figures 9 and 10, §4.2.1). Interestingly, the plateau is elevated in  $N_{\text{HI}}$  with respect to random places in the IGM by 0.3–0.6 dex. For  $D_{\text{tran}} \gtrsim 2 \text{ pMpc}$ , the values of  $\max(N_{\text{HI}})$  decline and become consistent with random places in the IGM.
4. The median  $N_{\text{HI}}$  as a function of 3D distance<sup>42</sup> smoothly declines with increasing  $D_{3\text{D}}$  and becomes consistent with random places in the IGM at  $D_{3\text{D}} \approx 3 \text{ pMpc}$  (Figure 14, §4.3).
5. The incidence<sup>43</sup> ( $\eta_{\text{abs}}$ ) of absorbers of all  $N_{\text{HI}}$  is higher within  $D_{\text{tran}} \lesssim 2$  physical Mpc of the position of a galaxy than at random places in the IGM (Figure 16, §5). For  $D_{\text{tran}} \gtrsim 2 \text{ pMpc}$ ,  $\eta_{\text{abs}}$  is consistent with that of the random IGM.
6. For absorbers with  $\log(N_{\text{HI}}) > 14.5 \text{ cm}^{-2}$ , there is a strong peak in the incidence,  $\eta_{\text{abs}}$ , close to galaxies at  $D_{\text{tran}} < 300 \text{ pkpc}$  (Figure 16, §5). No such peak is seen in the distribution of lower-column density absorbers. This suggests that absorbers with  $\log(N_{\text{HI}}) > 14.5 \text{ cm}^{-2}$  are more directly related to galaxies than absorbers of lower  $N_{\text{HI}}$ .
7. The incidence,  $\eta_{\text{abs}}$ , of absorbers with  $N_{\text{HI}} > 10^{14.5} \text{ cm}^{-2}$  and  $|\Delta v| < 300 \text{ km s}^{-1}$  shows rising values within  $D_{\text{tran}} < 300 \text{ pkpc}$ . From  $300 \text{ pkpc} < D_{\text{tran}} \lesssim 2 \text{ pMpc}$ , the  $\eta_{\text{abs}}$  roughly plateaus with  $\eta_{\text{abs}} \gtrsim 0.5$ . After  $\sim 2 \text{ pMpc}$ , the distribution becomes consistent with random places in the IGM (Figure 17, §5.1).
8. Within 300 pkpc and  $\pm 350 \text{ km s}^{-1}$  of a galaxy, the probability of intersecting an absorber with  $\log(N_{\text{HI}}) > 14.5$  is  $> 4$  times higher than at a random place in the IGM. (Figure 18 and Table 3, §5.1).
9. Maps of the incidence,  $\eta_{\text{abs}}$ , of low and high- $N_{\text{HI}}$  absorbers as a function of  $D_{\text{tran}}$  and  $D_{\text{Hubble}}$  allow for the measurement of redshift anisotropies (§6). In low- $N_{\text{HI}}$  gas [ $\log(N_{\text{HI}}) < 14.5$ ], on large scales (pMpc) the distribution along the line of sight is compressed compared to the distribution in the transverse direction. This is likely the signature of gas infall e.g. the Kaiser (1987) effect (Figure 24). In the high- $N_{\text{HI}}$  gas [ $\log(N_{\text{HI}}) > 14.5$ ], we find the “finger of God” effect, the elongation of the distribution along the line of sight compared to the transverse distribution (Figure 22). Taking into account the effect of our redshift errors, the data are consistent with peculiar velocities of  $\sim 250 \text{ km s}^{-1}$ . These conclusions are in agreement with those presented in

Rakic et al. (2011b) who used pixel optical depth analysis to demonstrate that the compression along the line of sight on large scales is highly significant ( $> 3\sigma$ ).

10. The Doppler widths ( $b_d$ ) of individual absorption lines in the HIRES spectra rise as the galactocentric distance is decreased (§7). The majority of the increased width is found within  $|\Delta v| < 150 \text{ km s}^{-1}$  and  $100 < D_{\text{tran}} < 300 \text{ pkpc}$  (Figures 26 and 28). The larger line widths could be caused by an increase in the gas temperature, the turbulence of the gas, or both. The median  $b_d$  close to galaxies are consistent with a gas temperature  $\sim 10^5 \text{ K}$ , or a turbulent contribution of  $\sim 20\text{--}30 \text{ km s}^{-1}$ .
11. Based on these measurements, we suggest a working definition of the circumgalactic medium (CGM) to be all locations within 300 pkpc and  $\pm 300 \text{ km s}^{-1}$  of a galaxy. We find that the CGM of our completeness corrected galaxy sample can account for nearly half of all absorbers with  $\log(N_{\text{HI}}) > 15.5$  (Figure 30, §8.2). Notably, the CGM of these galaxies comprises only 1.5% of the universe’s volume at these redshifts.

These findings not only define relevant scales of the CGM of luminous galaxies at redshift  $z \sim 2\text{--}3$ , but also demonstrate that much of the moderately high- $N_{\text{HI}}$  portion of the IGM likely originates in the regions surrounding luminous galaxies where the baryonic physics of galaxy formation appear to affect the physical state of the gas. This point may have important consequences for past and future studies of the “IGM” and should be considered in greater detail.

Our understanding of the physical properties of gas surrounding star-forming galaxies will greatly benefit from analysis of metallic absorption features in the HIRES spectra. These absorption lines probe the ionization state and metallicity of the gas and will provide direct constraints on the total mass in hydrogen and in metals that surround star-forming systems. This work is underway and will be published in the second paper in this series.

With this further analysis, we will have for the first time a quantitative snapshot of the baryonic interplay between the intergalactic medium and forming galaxies which is evidently central to the processes of galaxy formation and evolution.

The authors would like to thank Ryan Cooke who contributed the fits to the Damped Profiles in our QSO spectra. We are grateful to Bob Carswell for his assistance with the code VPFIT. Many thanks to Joop Schaye for his careful reading of the draft and insightful comments. We would also like to thank George Becker, Brian Siana, and Jean-René Gauthier for many helpful and interesting discussion. Thanks to Michele Fumagalli for providing the values listed in Table 5. We wish to acknowledge the staff of the the W.M. Keck Observatory whose efforts insure the telescopes and instruments perform reliably. Further, we extend our gratitude to those of Hawaiian ancestry on whose sacred mountain we are privileged to be guests.

This work has been supported by the US National Science Foundation through grants AST-0606912 and AST- 0908805. CCS acknowledges additional support from the John D. and Catherine T. MacArthur Foundation and the Peter and Patricia Gruber Foundation. Support for N.A.R. was provided by NASA through Hubble Fellowship grant HST-HF-01223.01 awarded by the Space Telescope Science Institute, which is

<sup>42</sup> The 3D distance,  $D_{3\text{D}}$ , is computed using the quadratic sum of the physical impact parameter between the galaxy and the line of sight to the QSO ( $D_{\text{tran}}$ ) and the line-of-sight distance one would calculate assuming the  $\Delta v$  of each absorber was due only to the Hubble flow,  $D_{\text{Hubble}}$ .

<sup>43</sup> The number of absorbers *per galaxy* with  $|\Delta v| < 300 \text{ km s}^{-1}$  and in a given bin of  $D_{\text{tran}}$ .

operated by the Association of Universities for Research in Astronomy, Inc., for NASA, under contract NAS 5-26555. This research has made use of the Keck Observatory Archive (KOA), which is operated by the W. M. Keck Observatory and the NASA Exoplanet Science Institute (NExSci), under contract with the National Aeronautics and Space Administration.

*Facilities:* Keck:I (LRIS), Keck:I (HIRES), Keck:II (NIR-SPEC)

## REFERENCES

- Adelberger, K. L., Shapley, A. E., Steidel, C. C., Pettini, M., Erb, D. K., & Reddy, N. A. 2005a, *ApJ*, 629, 636
- Adelberger, K. L., Steidel, C. C., Pettini, M., Shapley, A. E., Reddy, N. A., & Erb, D. K. 2005b, *ApJ*, 619, 697
- Adelberger, K. L., Steidel, C. C., Shapley, A. E., Hunt, M. P., Erb, D. K., Reddy, N. A., & Pettini, M. 2004, *ApJ*, 607, 226
- Adelberger, K. L., Steidel, C. C., Shapley, A. E., & Pettini, M. 2003, *ApJ*, 584, 45
- Barnes, L. A., Haehnelt, M. G., Tescari, E., & Viel, M. 2011, *ArXiv e-prints*
- Becker, G. D., Bolton, J. S., Haehnelt, M. G., & Sargent, W. L. W. 2011a, *MNRAS*, 410, 1096
- Becker, G. D., Rauch, M., & Sargent, W. L. W. 2009, *ApJ*, 698, 1010
- Becker, G. D., Sargent, W. L. W., Rauch, M., & Calverley, A. P. 2011b, *ApJ*, 735, 93
- Birnboim, Y. & Dekel, A. 2003, *MNRAS*, 345, 349
- Booth, C. M., Schaye, J., Delgado, J. D., & Dalla Vecchia, C. 2010, *ArXiv e-prints*
- Brooks, A. M., Governato, F., Quinn, T., Brook, C. B., & Wadsley, J. 2009, *ApJ*, 694, 396
- Bryan, G. L. & Machacek, M. E. 2000, *ApJ*, 534, 57
- Carswell, B., Schaye, J., & Kim, T. 2002, *ApJ*, 578, 43
- Cen, R., Miralda-Escudé, J., Ostriker, J. P., & Rauch, M. 1994, *ApJ*, 437, L9
- Chen, H.-W., Lanzetta, K. M., Webb, J. K., & Barcons, X. 2001, *ApJ*, 559, 654
- Conroy, C., Shapley, A. E., Tinker, J. L., Santos, M. R., & Lemson, G. 2008, *ApJ*, 679, 1192
- Cowie, L. L., Songaila, A., Kim, T.-S., & Hu, E. M. 1995, *AJ*, 109, 1522
- Crighton, N. H. M., Bielby, R., Shanks, T., Infante, L., Bornancini, C. G., Bouché, N., Lambas, D. G., Lowenthal, J. D., Minniti, D., Morris, S. L., Padilla, N., Péroux, C., Petitjean, P., Theuns, T., Tummuangpak, P., Weilbacher, P. M., Wisotzki, L., & Worseck, G. 2011, *MNRAS*, 414, 28
- Davé, R., Hernquist, L., Katz, N., & Weinberg, D. H. 1999, *ApJ*, 511, 521
- Dekker, H., D'Odorico, S., Kaufer, A., Delabre, B., & Kotzlowski, H. 2000, in *Society of Photo-Optical Instrumentation Engineers (SPIE) Conference Series*, Vol. 4008, Society of Photo-Optical Instrumentation Engineers (SPIE) Conference Series, ed. M. Iye & A. F. Moorwood, 534–545
- Duffy, A. R., Schaye, J., Kay, S. T., & Dalla Vecchia, C. 2008, *MNRAS*, 390, L64
- Ellison, S. L., Songaila, A., Schaye, J., & Pettini, M. 2000, *AJ*, 120, 1175
- Erb, D. K. 2008, *ApJ*, 674, 151
- Erb, D. K., Shapley, A. E., Pettini, M., Steidel, C. C., Reddy, N. A., & Adelberger, K. L. 2006a, *ApJ*, 644, 813
- Erb, D. K., Steidel, C. C., Shapley, A. E., Pettini, M., Reddy, N. A., & Adelberger, K. L. 2006b, *ApJ*, 647, 128
- , 2006c, *ApJ*, 646, 107
- Evoli, C. & Ferrara, A. 2011, *MNRAS*, 413, 2721
- Faucher-Giguère, C.-A. & Kereš, D. 2011, *MNRAS*, 412, L118
- Faucher-Giguère, C.-A., Kereš, D., & Ma, C.-P. 2011, *MNRAS*, 1399
- Faucher-Giguère, C.-A., Lidz, A., Hernquist, L., & Zaldarriaga, M. 2008, *ApJ*, 688, 85
- Finlator, K. & Davé, R. 2008, *MNRAS*, 385, 2181
- Förster Schreiber, N. M., Genzel, R., Bouché, N., Cresci, G., Davies, R., Buschkamp, P., Shapiro, K., Tacconi, L. J., Hicks, E. K. S., Genel, S., Shapley, A. E., Erb, D. K., Steidel, C. C., Lutz, D., Eisenhauer, F., Gillessen, S., Sternberg, A., Renzini, A., Cimatti, A., Daddi, E., Kurk, J., Lilly, S., Kong, X., Lehnert, M. D., Nesvadba, N., Verma, A., McCracken, H., Arimoto, N., Mignoli, M., & Onodera, M. 2009, *ApJ*, 706, 1364
- Fumagalli, M., Prochaska, J. X., Kasen, D., Dekel, A., Ceverino, D., & Primack, J. R. 2011, *MNRAS*, 1589
- Hernquist, L., Katz, N., Weinberg, D. H., & Miralda-Escudé, J. 1996, *ApJ*, 457, L51+
- Hui, L. & Gnedin, N. Y. 1997, *MNRAS*, 292, 27
- Kaiser, N. 1987, *MNRAS*, 227, 1
- Kereš, D. & Hernquist, L. 2009, *ApJ*, 700, L1
- Kereš, D., Katz, N., Davé, R., Fardal, M., & Weinberg, D. H. 2009, *MNRAS*, 396, 2332
- Kereš, D., Katz, N., Weinberg, D. H., & Davé, R. 2005, *MNRAS*, 363, 2
- Klypin, A. A., Trujillo-Gomez, S., & Primack, J. 2011, *ApJ*, 740, 102
- Kollmeier, J. A., Miralda-Escudé, J., Cen, R., & Ostriker, J. P. 2006, *ApJ*, 638, 52
- Law, D. R., Steidel, C. C., Erb, D. K., Larkin, J. E., Pettini, M., Shapley, A. E., & Wright, S. A. 2009, *ApJ*, 697, 2057
- Law, D. R., Steidel, C. C., Shapley, A. E., Nagy, S. R., Reddy, N. A., & Erb, D. K. 2011, *ArXiv e-prints*
- McDonald, P., Miralda-Escudé, J., Rauch, M., Sargent, W. L. W., Barlow, T. A., & Cen, R. 2001, *ApJ*, 562, 52
- McLean, I. S., Becklin, E. E., Bendiksen, O., Brims, G., Canfield, J., Figer, D. F., Graham, J. R., Hare, J., Lacayanga, F., Larkin, J. E., Larson, S. B., Levenson, N., Magnone, N., Teplitz, H., & Wong, W. 1998, in *Society of Photo-Optical Instrumentation Engineers (SPIE) Conference Series*, Vol. 3354, Society of Photo-Optical Instrumentation Engineers (SPIE) Conference Series, ed. A. M. Fowler, 566–578
- Miralda-Escudé, J., Cen, R., Ostriker, J. P., & Rauch, M. 1996, *ApJ*, 471, 582
- Morris, S. L. & Jannuzi, B. T. 2006, *MNRAS*, 367, 1261
- Navarro, J. F., Frenk, C. S., & White, S. D. M. 1997, *ApJ*, 490, 493
- Nestor, D. B., Shapley, A. E., Steidel, C. C., & Siana, B. 2011, *ApJ*, 736, 18
- Ocvirk, P., Pichon, C., & Teyssier, R. 2008, *MNRAS*, 390, 1326
- Oke, J. B., Cohen, J. G., Carr, M., Cromer, J., Dingizian, A., Harris, F. H., Labrecque, S., Lucinio, R., Schaaf, W., Epps, H., & Miller, J. 1995, *PASP*, 107, 375
- Oppenheimer, B. D. & Davé, R. 2008, *MNRAS*, 387, 577
- Oppenheimer, B. D., Davé, R., Kereš, D., Fardal, M., Katz, N., Kollmeier, J. A., & Weinberg, D. H. 2010, *MNRAS*, 406, 2325
- Pettini, M., Hunstead, R. W., Smith, L. J., & Mar, D. P. 1990, *MNRAS*, 246, 545
- Pettini, M., Shapley, A. E., Steidel, C. C., Cuby, J., Dickinson, M., Moorwood, A. F. M., Adelberger, K. L., & Gialalisco, M. 2001, *ApJ*, 554, 981
- Pettini, M., Steidel, C. C., Adelberger, K. L., Dickinson, M., & Gialalisco, M. 2000, *ApJ*, 528, 96
- Prochaska, J. X., Weiner, B., Chen, H., Mulchaey, J. S., & Cooksey, K. L. 2011, *ArXiv e-prints*
- Rakic, O., Schaye, J., Steidel, C. C., & Rudie, G. C. 2011a, *MNRAS*, 414, 3265
- , 2011b, *ArXiv e-prints*
- Rauch, M., Miralda-Escudé, J., Sargent, W. L. W., Barlow, T. A., Weinberg, D. H., Hernquist, L., Katz, N., Cen, R., & Ostriker, J. P. 1997, *ApJ*, 489, 7
- Reddy, N., Dickinson, M., Elbaz, D., Morrison, G., Gialalisco, M., Ivison, R., Papovich, C., Scott, D., Buat, V., Burgarella, D., Charmandaris, V., Daddi, E., Magdis, G., Murphy, E., Altieri, B., Aussel, H., Dannerbauer, H., Dasyra, K., Hwang, H. S., Kartaltepe, J., Leiton, R., Magnelli, B., & Popesso, P. 2011, *ArXiv e-prints*
- Reddy, N. A. & Steidel, C. C. 2009, *ApJ*, 692, 778
- Reddy, N. A., Steidel, C. C., Pettini, M., Adelberger, K. L., Shapley, A. E., Erb, D. K., & Dickinson, M. 2008, *ApJS*, 175, 48
- Richards, G. T., Strauss, M. A., Fan, X., Hall, P. B., Jester, S., Schneider, D. P., Vanden Berk, D. E., Stoughton, C., Anderson, S. F., Brunner, R. J., Gray, J., Gunn, J. E., Ivezić, Ž., Kirkland, M. K., Knapp, G. R., Loveday, J., Meiksin, A., Pope, A., Szalay, A. S., Thakar, A. R., Yanny, B., York, D. G., Barentine, J. C., Brewington, H. J., Brinkmann, J., Fukugita, M., Harvanek, M., Kent, S. M., Kleinman, S. J., Krzesiński, J., Long, D. C., Lupton, R. H., Nash, T., Neilsen, Jr., E. H., Nitta, A., Schlegel, D. J., & Snedden, S. A. 2006, *AJ*, 131, 2766
- Ricotti, M., Gnedin, N. Y., & Shull, J. M. 2000, *ApJ*, 534, 41
- Ryan-Weber, E. V., Pettini, M., & Madau, P. 2006, *MNRAS*, 371, L78
- Ryan-Weber, E. V., Pettini, M., Madau, P., & Zych, B. J. 2009, *MNRAS*, 395, 1476
- Schaye, J. 2001, *ApJ*, 559, 507
- Schaye, J., Theuns, T., Leonard, A., & Efstathiou, G. 1999, *MNRAS*, 310, 57
- Schaye, J., Theuns, T., Rauch, M., Efstathiou, G., & Sargent, W. L. W. 2000, *MNRAS*, 318, 817
- Shapley, A. E., Steidel, C. C., Erb, D. K., Reddy, N. A., Adelberger, K. L., Pettini, M., Barmby, P., & Huang, J. 2005, *ApJ*, 626, 698
- Shapley, A. E., Steidel, C. C., Pettini, M., & Adelberger, K. L. 2003, *ApJ*, 588, 65



- Shen, S., Madau, P., Aguirre, A., Guedes, J., Mayer, L., & Wadsley, J. 2011, ArXiv e-prints
- Simcoe, R. A. 2011, ApJ, 738, 159
- Simcoe, R. A., Cooksey, K. L., Matejek, M. E., Burgasser, A. J., Bochanski, J., Lovegrove, E., Bernstein, R. A., Pipher, J. L., Forrest, W. J., McMurtry, C., Fan, X., & O'Meara, J. 2011, ArXiv e-prints
- Simcoe, R. A., Sargent, W. L. W., & Rauch, M. 2002, ApJ, 578, 737
- Songaila, A. & Cowie, L. L. 1996, AJ, 112, 335
- Steidel, C. C., Adelberger, K. L., Shapley, A. E., Pettini, M., Dickinson, M., & Giavalisco, M. 2003, ApJ, 592, 728
- Steidel, C. C., Bogosavljević, M., Shapley, A. E., Kollmeier, J. A., Reddy, N. A., Erb, D. K., & Pettini, M. 2011, ArXiv e-prints
- Steidel, C. C., Erb, D. K., Shapley, A. E., Pettini, M., Reddy, N., Bogosavljević, M., Rudie, G. C., & Rakic, O. 2010, ApJ, 717, 289
- Steidel, C. C., Shapley, A. E., Pettini, M., Adelberger, K. L., Erb, D. K., Reddy, N. A., & Hunt, M. P. 2004, ApJ, 604, 534
- Theuns, T., Leonard, A., Efstathiou, G., Pearce, F. R., & Thomas, P. A. 1998, MNRAS, 301, 478
- van de Voort, F. & Schaye, J. 2011, ArXiv e-prints
- van de Voort, F., Schaye, J., Booth, C. M., & Dalla Vecchia, C. 2011a, MNRAS, 415, 2782
- van de Voort, F., Schaye, J., Booth, C. M., Haas, M. R., & Dalla Vecchia, C. 2011b, MNRAS, 414, 2458
- Vogt, S. S., Allen, S. L., Bigelow, B. C., Bresee, L., Brown, B., Cantrall, T., Conrad, A., Couture, M., Delaney, C., Epps, H. W., Hilyard, D., Hilyard, D. F., Horn, E., Jern, N., Kanto, D., Keane, M. J., Kibrick, R. I., Lewis, J. W., Osborne, J., Pardeilhan, G. H., Pfister, T., Ricketts, T., Robinson, L. B., Stover, R. J., Tucker, D., Ward, J., & Wei, M. Z. 1994, in Society of Photo-Optical Instrumentation Engineers (SPIE) Conference Series, Vol. 2198, Society of Photo-Optical Instrumentation Engineers (SPIE) Conference Series, ed. D. L. Crawford & E. R. Craine, 362–+
- Wakker, B. P. & Savage, B. D. 2009, ApJS, 182, 378
- Wiersma, R. P. C., Schaye, J., Dalla Vecchia, C., Booth, C. M., Theuns, T., & Aguirre, A. 2010, MNRAS, 409, 132
- Zhang, Y., Anninos, P., & Norman, M. L. 1995, ApJ, 453, L57+